

Parameterization of subgrid-scale processes in finite element sea ice-ocean models

DOCTORAL DISSERTATION PRESENTED BY

ALICE PESTIAUX

FOR THE DEGREE OF DOCTOR IN SCIENCES

THESIS COMMITTEE:

Prof. Thierry Fichefet (Supervisor)
Prof. Eric Deleersnijder (Supervisor)
Université catholique de Louvain
Prof. Marie-Laurence De Keersmaecker (Chair)
Prof. Hugues Goosse
Université catholique de Louvain

Louvain-la-Neuve 26 June 2015

Voilà une page qui se tourne. Et une thèse, c'est long... Très long... On sait quand on commence, mais on ne sait pas quand ce sera fini. Mais au delà de toutes les épreuves, des analyses, des doutes, des présentations et des rédactions et aussi de tous les buggs, et là nombreux savent qu'il y en a eu pas mal, un chemin se trace et finalement, on arrive à cette fin. Bien évidemment, tout ce parcours n'aurait pas été possible sans l'aide de nombreuses personnes, qui m'ont guidée, encouragée et soutenue pendant ces cinq années, et je tiens à les remercier chaleureusement.

Je remercie tout d'abord mes promoteurs de thèse, Thierry Fichefet et Eric Deleersnijder. Merci Thierry pour ton soutien quotidien et ton pragmatisme face aux problèmes de code ou de résultats. Merci aussi pour tes judicieux conseils à propos de pistes d'analyses ou de changement d'orientation. Merci Eric pour les discussions que nous avons eues et pour tes suggestions toujours pertinentes. A tous les deux, un grand merci pour votre disponibilité et toutes les opportunités et responsabilités que vous m'avez permis d'endosser.

Je remercie également les autres membres de mon jury pour leur relectures attentives, leurs questions pertinentes et les discussions qui ont suivies. Martin, merci pour ton aide précieuse dans la compréhension de LIM3, à travers toutes ses lignes de code mais aussi de ses résultats. Vincent, merci pour ta curiosité et le regard pertinent que tu as porté sur mon travail. Hugues, merci pour ton enthousiasme et pour les pistes de réflexion que tu m'as suggérées. Sergey, thank you for your great support with FESOM and your continuous availability through these three years.

I would like to thank the AWI team for its welcome and its help. Thanks a lot to Dmitry Sidorenko and Qiang Wang for their support and advices relative to the numerous buggs I get in the coupling. I would also like to thank Claudia Wekerle, Xuezhu Wang, Madlen Kimmritz, Martin Losch and other people from the Climate Dynamics group for making it a pleasure coming to Bremerhaven.

Je voudrais maintenant remercier mes collègues, dont nombreux d'entre eux sont devenus des amis. Merci à tous ceux qui ont contribués aux bons moments à la cafétaria, aux activités ou petits repas. Un grand merci Oli, pour toutes les lectures et le grand debuggage du code, merci pour tes conseils mais surtout aussi pour tes encouragements lorsque rien ne marchait ou tout buggait. Merci à l'équipe de "glace", Antoine, Sylvain B., Sylvain M., Jonathan, François pour leur écoute et leurs conseils. Mathilde, merci pour les petites séances de jogging et les grandes séances de papotage. Merci Eli et Violette pour ces petites discussions essentielles à ma décompression face à cette longue thèse. Merci également à Monique et Dominique pour leur disponibilité, leur bonne humeur et leur travail discret mais très efficace. En MEMA, je tenais

aussi à remercier pour leur aide et leur convivialité, Jean-François, Jonathan, Christopher, Philippe et Valentin.

Je tiens à remercier le Fonds pour la formation à la Recherche dans l'Industrie et dans l'Agriculture (FRIA) pour m'avoir octroyé une bourse de recherche durant quatre années de doctorat. Je suis également reconnaissante envers le projet SLIM, financé par la Commaunté Française de Belgique, comme Actions de Recherche Concertées, sous le contrat ARC 10/15-028, et envers "The North-German Supercomputing Alliance (HLRN)" pour avoir mis à ma disposition les moyens logistiques nécessaires au bon déroulement de ma thèse.

Enfin, je termine avec le plus important, la famille. Je voudrais remercier mes parents pour m'avoir toujours soutenue d'une manière ou d'une autre, dans mes choix, mes études, tant au point de vue logistique qu'affectif. Merci Adrien pour ta présence, tes attentions et tes encouragements. Enfin, présent depuis le début, à travers les buggs, les départs pour les conférences, les rédactions, merci Benoît pour ton soutien quotidien, tes petits attentions et ta compréhension. Même si tu ne sauras lire ces lignes que dans quelques années, merci Jade de m'aider à relativiser toutes les doutes ou inquiétudes que j'ai pu avoir.

A Jade et Benoît.

Contents

\mathbf{C}	ontei	nts	iii
1	Inti	roduction	3
	1.1	Improved resolution with the finite element method	7
	1.2	Improvement of the Gent-McWilliams velocity	11
	1.3	Subgrid-scale processes in sea ice models	13
	1.4	Objectives of the thesis	16
2	Str	ongly anisotropic diffusion operator	21
	2.1	Introduction	22
	2.2	Diffusion equation	25
	2.3	DGFEM formulation	27
	2.4	Interior penalty factor	28
		2.4.1 Eigenvalue penalty factor	29
		2.4.2 Oriented penalty factor	31
		2.4.3 Eigenvalue penalty factor vs oriented penalty factor	34
	2.5	Comparison with the method of manufactured solutions	36
	2.6	Physical application	44
	2.7	Concluding remarks	48
3	Ger	nt-McWilliams velocity and isopycnal diffusion	51
	3.1	Introduction	52
	3.2	Equations of the tracer model	54
		3.2.1 Gent-McWilliams velocity	55
		3.2.2 The issue of boundary conditions	56
		3.2.3 Isopycnal diffusion	57
	3.3	Discontinuous finite element discretization	58
		3.3.1 DGFEM formulation of the advective part	60
		3.3.2 DGFEM formulation of the diffusive part	61
	3.4	Investigation of the vanishing isoneutral flux	63
	3.5	Results	66
		3.5.1 Illustration of the isopycnal diffusion	66

•	
1V	Contents

	3.6	3.5.3 Application to an idealized channel	67 70 74
4	The		77
	4.1	Introduction	77
	4.2	Description of the models	79
		4.2.1 FESOM	79
		Ocean model	30
		Sea ice	31
		4.2.2 LIM3	33
	4.3	Coupling strategy	36
		4.3.1 Storing sea ice state variables on the FESOM grid	37
		4.3.2 Calling sequence	38
		4.3.3 Inputs/Outputs	38
		4.3.4 Input heat fluxes to LIM3	90
	4.4	Experimental design	92
	4.5	Model tuning	94
	4.6	Concluding remarks	97
_			
5		i	99
	5.1		00
	5.2		00
		e e e e e e e e e e e e e e e e e e e)1
		v)1
		•)2
		*)5
)6
)7
		v)7
)9
			11
		v	12
			14
	5.3	v G	17
		- U	18
			22
			25
	٠.		29
	5.4	Concluding remarks	31
6	Cor	nclusions	33

Contents	v

Appendices 141			
\mathbf{A}	Supplementary material for Chapter 3	141	
В	Supplementary material for Chapter 4 B.1 EVP rheology in FESOM		
Re	eferences	149	

Contents 1

Preamble

In the current context of models improvement for better climate studies and predictions, simulating small scale physical processes remain a challenge. In this respect, and for reasons explained in this thesis, subgrid-scale parameterizations are adopted whenever such processes cannot be explicitly represented. However, parameterizations are by nature, approximations of reality and sometimes come along with concomitant shortcomings. Often, this kind of issues are raised when parameterizations are used in conditions that are close to validity limits of hypotheses they are based on. In order to prevent those parameterizations from shifting to unphysical behaviours, what is hereafter referred as "numerical artefacts" are used. In models based on the finite element method, these artefacts are distinctive due to the specificity of the formalism itself. In this thesis, we aim at identifying the best compromise between these numerical workarounds and the preservation of physics, through the study of subgrid-scale parameterizations in two different models based on the finite element method. These models are successively used in configurations of increasing complexity, in order to ultimately understand the impacts of parameterizations on the models physics accuracy and their skills with respect to observations.

Three different models are used throughout this thesis. In the first part treating of the parameterization of mesoscale eddies, the Second-generation Louvain-la-Neuve Ice-ocean Model¹ (SLIM; White et al., 2008a; Blaise et al., 2010; Kärnä et al., 2012) is considered. With its discretization based on the discontinuous Galerkin finite element method (dgFEM), chapter 2 tackles some technical issues relative to the penalty terms that are required to stabilize the numerical scheme. Chapter 3 presents some toy oceanic applications with SLIM to highlight the impacts of this parameterization, but these simulations remain idealized since the development of SLIM in order to reach a global version has been stopped. Indeed, the applications within this framework are now oriented towards the land-sea continuum. SLIM is then not ready to simulate more realistic global applications, in particular because of the limited available computational time. Indeed, the usual period in realistic applications in order to study the effects of the mesoscale eddies is over 1000 years after a stabilization period of 10.000 years. The first two chapters are then more theoretical. In the second part of this thesis, the parameterization of some sea-ice subgrid-scale processes are already included in the Louvain-la-Neuve sea-Ice Model (LIM3; Vancoppenolle et al., 2009b). Initially, it is embedded in the ocean modelling system NEMO (Madec and team, 2008) which is discretized on a structured grid. In chapter 4, some key components of LIM3 have been separated from NEMO and coupled to the Finite Element Sea-ice Ocean Model (FESOM; Danilov et al.,

 $^{^{1}}http//www.climate.be/slim/$

2 Contents

2004; Wang et al., 2008; Timmermann et al., 2009) using unstructured triangular surface meshes, in order to take advantages from each model (unstructured mesh, sophisticated representation of sea ice physics). From this perspective, chapter 5 shows some more complex results of FESOM-LIM3 simulations to present the main features of this new coupled model.

CHAPTER

Introduction

The spatial resolution of the numerical ocean models is established according to what they intend to represent: estuaries, coastal seas or large-scale flows. For any chosen resolution, there are always subgrid-scale processes that cannot be explicitly resolved. From there, the first direct solution to this issue is to increase the resolution of the mesh, but such an improvement on the whole studied domain often requires too large a computational cost. An intermediary step is to use an unstructured mesh instead of the usual structured grid since local refinement is easily possible in the areas of interests. Yet another problem is that, sometimes, independently from resolution, the physics of the process to be represented are not well known. A way to sidestep those problems is to make use of relatively simple, subgrid-scale parameterizations in order to approximate processes that are too complex or local to be explicitly resolved (Holland, 1989). The inclusion of these subgrid-scale processes in finite element ocean-sea ice models is investigated through this thesis.

In the global ocean, the most energetic motions occur at the mesoscale. Taking place on spatial scales ranging from 75 to 200km, the mesoscale eddies result from barotropic and baroclinic instabilities, which occur in most places of the World Ocean. They stir and mix salinity and temperature, as well as other tracers, and, by doing so, influence the density field and thus the general ocean circulation (Rhines, 2009). Parameterizing their effects on the tracer fields significantly provides simulations closer to reality than without them.

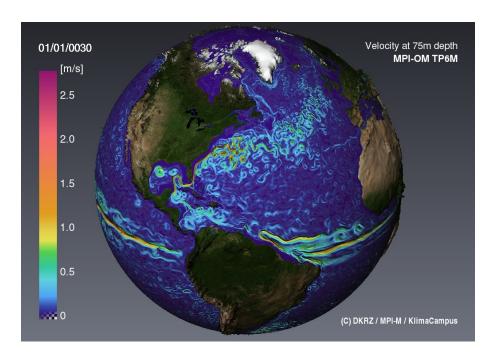


Figure 1.1: Visualization of the ocean velocity at 75m depth highlighting the structure of the most important currents in the North Atlantic simulated by the high-resolution eddy resolving ocean model MPIOM TP6M with a horizontal grid spacing of 10km (source: http://www.dkrz.de/Klimaforschung-en/konsortial-en/storm-en).

For instance, some improvements are noticed in the global temperature and salinity distributions, the heat fluxes and the location of deep water formation (Danabasoglu et al., 1994; Danabasoglu and McWilliams, 1995). Although they have been studied for half a century, ocean eddies are still difficult to understand and interpreting their associated impacts remains complex. Iselin (1939) and Montgomery (1940) suggested that tracers are mainly mixed by eddies along the isopycnals, i.e. the surfaces of constant density. These surfaces are not horizontal in most of oceanic regions. Isopycnal mixing is much stronger, whereas diapycnal mixing, which happens across these surfaces, is much slower (McDougall and Church, 1986). Historically, a scalar diffusion was traditionally used for simplicity but in addition with a vertical diffusivity which is smaller by several orders of magnitude than the horizontal one. In order to model the effects of this anisotropic turbulence and transport along and across isopycnals, Redi (1982) considered a new isopycnal mixing tensor where the main axis of diffusivity have been rotated from the standard cartesian coordinates towards

any direction where there is a density gradient. The first attempts of their representations were not convincing (Cox, 1987; Hirst and Cai, 1994) since it proved necessary to add a background horizontal diffusion to prevent numerical instability. Changing the traditional horizontal/vertical grid to isopycnal coordinates did not solve the problem (McDougall, 1987). Moreover, the main issue remained that the effects of unresolved mesoscale eddies were not adequately simulated. In order to incorporate the baroclinic effects of mesoscale eddies, and thus to reduce the available potential energy without resolving the eddies in the model, Gent and McWilliams (1990) suggested to add an extra velocity (GM) which conserves all tracer moments between the isopycnals. This GM parameterization which is very popular today, is implemented in the majority of the OGCMs and brings the following major improvement: the non-divergent GM velocity relaxes the density slopes and thus releases potential energy.

Sea ice, which refers to any form of frozen seawater, covers, on average, about 7% of the oceans. It modifies the heat, mas and momentum exchanges between atmosphere and ocean. Due to its low thermal conductivity (Pringle et al., 2007), sea ice insulates the ocean from the atmosphere. In order to describe the state of the sea ice cover, which is very sensitive to the climate changes, the sea ice extent, which is defined as the sum of cell areas with ice concentration above 15%, is used. Indeed, the maximum sea ice extent in the

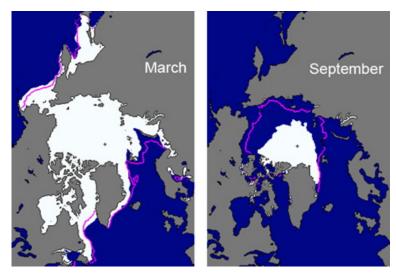


Figure 1.2: Illustrations of the respective monthly averages of sea ice extent in March 2013 (left) and September 2013 (right), where the pink line represents the monthly mean ice extent during the period 1981 – 2010. (source: nsidc.org/data/seaice_index)

Northern Hemisphere reaches about $15 \times 10^6 \text{ km}^2$ in March and its minimum drops to around 4.5×10^6 km² in September. In the Antarctic, the extent varies between $3 \times 10^6 \mathrm{km}^2$ in February and $18 \times 10^6 \mathrm{km}^2$ in September. Due to its high reflectance in the visible spectrum and its low thermal conductivity, the sea ice cover limits heat, momentum and water mass exchanges between the atmospheric boundary layer and the upper ocean. Furthermore, the salt rejected during sea ice formation significantly influences the high-latitude oceanic convection and hence the global ocean circulation (Aagaard and Carmack, 1989). The acceleration of the recent decline of the Arctic sea ice cover is partly linked to the ice-albedo feedback which is, in part, responsible for the high sea ice sensitivity to climate change (Stroeve et al., 2012). Indeed, a positive imbalance in the surface energy budget leads to a lower sea ice coverage, subsequently followed by a higher solar absorption in the upper ocean, which further intensifies the sea ice melting. Therefore, sea ice can act as positive feedback for the climate warming. To get a better understanding of the climate system as well as better projections, general circulation models (GCMs) and their sea ice component need to be improved (IPCC, 2013).

Sea ice undergoes also very small-scale processes that affect its large-scale properties. As illustrated in Figure 1.3, sea ice can be studied at many different scales because of its spatial heterogeneity. This heterogeneity is mainly due to

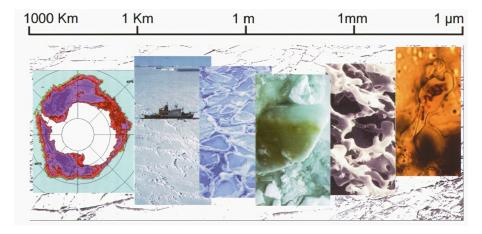


Figure 1.3: Illustration of sea ice spanning several characteristic scales (taken from Thomas and Dieckmann (2003)). From the left to the right: satellite image of the Antarctic sea ice extent in September, pack ice field, pancake ice, sea ice floe colored by diatoms, brine channels and a diatom chain in a brine pocket.

processes linked to ice deformation in response to wind forcing and oceanic

surface currents that set it in motion, to the presence of snow or the sea ice dynamic. Moreover, the interactions between processes occurring at different scales are very strong. The large-scale oceanic circulation undeniably affects the boundary conditions for small-scale sea ice processes, but these small-scale processes also modify this large-scale ocean circulation through numerous interactive processes. For example, brine released from sea ice affects the deep convection, and thus the thermohaline circulation (e.g., Vihma et al., 2014). Through these studies, it is incontestable that small-scale physical processes play an important role, especially at the interfaces and within the boundary layers.

As for the ocean, all the mechanisms associated with sea ice evolution cannot be exhaustively resolved in climate models. Small-scale processes occurring at scales smaller than the model grid sizes are represented thanks to parameterizations, as functions of the state variables that are resolved by the models (such as the sea ice concentration or thickness). This is, for instance, the case of the sea ice growth and melt, brine or the ridging/rafting mechanisms (Holland et al., 2006). Besides, many processes dependent on ice or snow thicknesses cannot be explicitly represented (Schramm et al., 1997), so that their parameterizations remain essential. However, these parameterizations are by definition based on approximations of the real processes and are used either because these processes are too complex or local to be represented explicitly in models or simply because they are not well understood. In addition, parameterizations require observational data to be calibrated properly. Even with these difficulties, subgrid-scale parameterizations remain important in large-scale sea ice models in order to improve their results. For instance, some sophisticated large-scale sea ice models use subgrid-scale parameterizations to improve their representation of the ice thickness, enthalpy and salt distributions.

Before including some subgrid-scale parameterizations in a model, a first improvement that concerns both the ocean and sea ice, can be made with respect to the mesh. Instead of the usual structured grid which is often quite coarse in order to save computational time, an unstructured mesh can be used. A better representation of the coastlines with some local refinements already allow to improve the realism of results or to study some processes in particular areas, such as the Canadian Arctic Archipelago.

1.1 Improved resolution with the finite element method

Traditionally, geophysical models have been based on structured grids and finite difference schemes because of the ease of implementation (Griffies et al., 2000). For instance, LIM3 used in this study, is based on this formalism. As

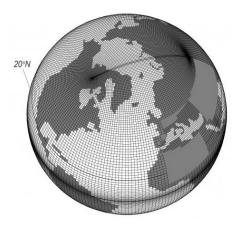


Figure 1.4: Illustration of the structured grid used by NEMO [source: http://www.nemo-ocean.eu].

illustrated in Figure 1.4, the grid is regular and the cells are oriented with respect to the latitude and longitude coordinates. Although the implemented algorithms are very fast with this kind of discretization, these meshes suffer from a lack of flexibility. A way to skirt this issue is to adopt the alternative unstructured mesh, as shown in Figure 1.5. SLIM in which the mesoscale ed-



Figure 1.5: Illustration of the unstructured mesh used by SLIM.

dies will be parameterized in this thesis, is based on this kind of mesh. Its flexibility is a real advantage since the mesh can follow the coastlines and the

resolution can be improved in a particular area in order to capture its specific geometry (Legrand et al., 2000).

For this reason, unstructured meshes become to be used in ocean modelling with the finite element method (FEM; e.g., Piggott et al., 2007; White et al., 2008b; Danilov et al., 2004) or with the finite volume method (FVM, e.g. FV-COM, SUNTANS, D-flow FM; Lai et al., 2010; Chen et al., 2003; Kernkamp et al., 2011), especially thanks to their ability to locally increase the resolution, as shown in Figure 1.6. This feature is particularly important for capturing the ocean bathymetry (Gorman et al., 2006) and boundaries, defined by the coasts or the islands. In the case of multiscale problems, the mesh can be refined

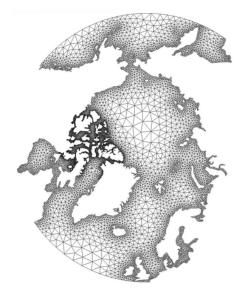


Figure 1.6: Example of unstructured mesh refined along the coastlines and in the Canadian Arctic Archipelago (SLIM's mesh).

wherever and whenever necessary, for example when eddies appear (Bernard et al., 2007). Unstructured meshes also allow to avoid the North Pole singularity.

Two other advantages of the FEM are sometimes a more convenient conservation of the energy and the straightforward treatment of the weak boundary conditions. However, this method remain more complex with technicalities than the finite difference method. Both the finite difference method and the FEM compute approximations of the solution at some particular points of the domain, called nodes. The main difference between those two methods lies in

the choice of the discretization. Indeed, the differential operators are directly discretized by the finite difference method, whereas with the FEM, they are applied on the discretized fields.

Sea ice modelling with the FEM is not new. Indeed, Mukherji (1973) took advantages of it in order to simulate the crack propagation within the ice pack. Then, Sodhi and Hibler (1980) used the method proposed by Becker (1976) to compute the ice drift in the complex area of Strait of Belle Isle. At the origin, the majority of modelling studies were idealized test cases, as the study of ice motion in the Beaufort Sea by Thomson (1988), the use of different sea ice rheologies (Schulkes et al., 1998) or the investigation of a Lagrangian sea ice description (Wang and Ikeda, 2004). Complexity and thus realism were progressively brought to these models in order to improve the sea ice representation, with regional sea ice modelling developed around Greenland (Kliem, 2001) or in the Arctic Ocean (Yakovley, 2003; van Scheltinga et al., 2010). In particular, Lietaer et al. (2008) investigated the effects of resolving the Canadian Arctic Archipelago (CAA) in a finite element sea ice model. Even if there is no ocean dynamics or oceanic feedbacks in this work, the sea ice results close to the straits are influenced by the fact that the CAA is closed or open, and the ice exchanges through this area are non-negligible (the sea ice volume in the CAA represents 10% of the total sea ice volume of the model). FESOM proves to have advantages in long-term simulations with respect to the mesh refinement in different studies (Sidorenko et al., 2011; Wang et al., 2012; Juricke et al., 2012; Wekerle et al., 2013). For instance, the latter study examines the characteristics of the individual CAA channels with a mesh resolution of 5km in this area. The variability of the freshwater transport through the CAA is shown to be mainly regulated by the variability of ocean volume transport, as suggested by observations (Peterson et al., 2012).

Even if unstructured meshes lead to some improvements in ocean and sea ice simulations (Lietaer et al., 2008; Wang et al., 2012; Wekerle et al., 2013), parameterizations of subgrid-scale processes remain necessary in most of the GCMs. Indeed, even an eddy-resolving ocean model with a horizontal mesh resolution of around $1/12^{\circ}$, which allows to resolve the largest baroclinic eddies but in only some parts of the ocean, requires such parameterizations and as a result, these processes increase the computational time (Masumoto et al., 2004).

1.2 Improvement of the Gent-McWilliams velocity

As shown in Figure 1.7, the impacts of the mesoscale eddies can be parameterized thanks to two distinct processes: the isopycnal diffusion and the GM velocity. Indeed, the main diffusion relative to these eddies mainly occurs along the surfaces of constant density. In the formulation of the diffusivity tensor, the smaller diffusion (diapycnal) which takes place across these surfaces, is also taken into account but has a much smaller magnitude since it is linked to molecular turbulence. Besides, the GM velocity, which is computed thanks to the density gradient, tends to relax density slopes.

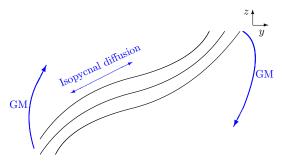


Figure 1.7: Schematic illustration of isopycnals (black lines) where the main effects of the parameterization of the mesoscale eddies are represented in blue: the isopycnal diffusion mainly diffuse the tracers along these same surfaces whereas the GM velocity principally tends to slump the isopycnals.

Most current numerical ocean models (e.g., NCAR Climate System Model, HOPE, ECHAM; Gent et al., 1998; Marsland et al., 2003; Jungclaus et al., 2006) use the parameterization of mesoscale eddies. From the density gradient, the eddy-induced transport streamfunction $\underline{\psi}$, which is on the basis of the GM scheme, is computed:

$$\underline{\psi} = A^I \frac{\nabla_h \rho}{\partial_z \rho} \times \hat{\underline{e}}_z, \tag{1.1}$$

where A^I is the eddy diffusivity, ρ the seawater density and $\underline{\hat{e}_z}$ the vertical unit vector. The associated velocity:

$$\underline{u}_{GM} = \nabla \times \psi \tag{1.2}$$

is computed and used to advect the tracers in addition to the Eulerian velocity. In practice, the streamfunction computation is difficult in realistic simulations, especially because of its decrease to zero at the top and bottom boundaries and because of the vertical stratification. Indeed, near the top and bottom boundaries, the neutral slope, that is used in the streamfunction computation, can become infinite. In order to handle this issue, the typical methods are

to progressively cancel the streamfunction at the boundaries or to impose an arbitrary limit on the neutral slope. However, these methods are not based on physical processes and the results are closely connected to numerical details. In addition, these tapering functions run counter to the evolution of mesoscale eddies towards larger vertical scales.

In order to overcome this issue, Ferrari et al. (2010) suggest to solve a one-dimensional boundary-value problem where the eddy-induced streamfunction \widetilde{Y} is the solution of:

$$\left(c^2 \frac{d^2}{dz^2} - N_b^2\right) \widetilde{Y} = \frac{g}{\rho_0} \nabla_h \rho$$

$$\widetilde{Y}(\eta) = \widetilde{Y}(-H) = [0, 0],$$
(1.3)

where $N_b=\sqrt{-\frac{g}{\rho_0}\frac{\partial\rho}{\partial z}}$ is the Brunt-Väisälä frequency, $c=\frac{N_bH}{\pi}$ is a depth independent speed relative to the Eady problem (Eady, 1949), H is the depth, ρ_0 is the constant reference density, g is the gravitational acceleration and η the ocean surface elevation. The approximation $[\tilde{Y}, 0]$ is then close to ψ except near the surface and the bottom since the transport vanishes there by definition. Applied on each water column, the new parameterized transport satisfies, without any additional tapering or matching conditions, two key properties: homogeneous Dirichlet boundary conditions at the ocean surface and bottom, and presence of slow baroclinic modes in this vertical structure that are consistent with the phenomenology of the geostrophic turbulence. Moreover, some important attributes of the scheme should be mentioned: the parameterized eddy transport is interpolated through regions of weak stratification without any ceiling on the neutral slope, and the parameterization provides a non-local sink of potential energy, whereas it was local for the scheme of Gent and Mc-Williams (1990). This one-dimensional boundary value formulation is already used in the popular Modular Ocean Model (MOM, Dunne et al., 2012), and its coupled versions, e.g., the Australian Community Climate and Earth System Simulator (ACCESS, Bi et al., 2013) or the ICTP-MOM ocean-sea-ice model (Farneti, 2012).

Such improvements in the representation of physical processes through the subgrid-scale parameterizations are also possible in sea ice models. For instance, the ice thickness distribution enables the representation of several ice categories within a single grid cell. Its parameterization in sea ice models influences the variability in both the ocean and sea ice. For example, in the ocean, the thermohaline circulation can be modified due to the inclusion of the ice thickness distribution (Bitz et al., 2001).

 $^{^{1}\}mathrm{The}$ tilde refers to a two-dimensional vector, whereas the underline refers to a three-dimensional vector.

1.3 Subgrid-scale processes in sea ice models

Present-day sea ice models provide realistic estimates in terms of mean state and variability. The first detailed thermodynamic model was presented by Maykut and Understeiner (1971), in which the exchange of mass and the storage of heat in the ice are treated. Nowadays, most sea ice models are coupled to ocean models or to climate models in order to investigate its interactions with ocean and atmosphere. Typically, sea ice thermodynamics is treated using the Semtner (1976) 0- or 3-layer formalism or the more sophisticated model of Bitz and Lipscomb (1999). Soon, the large-scale dynamical processes were taken into account in models (Coon et al., 1974; Hibler, 1979). In this purpose, the internal behaviour of the sea ice has been studied. In Hibler (1979), the sea ice is assumed to be a non-linear viscous-plastic (VP) medium whose resistance to deformation depends on its instantaneous states of motion and on several sea ice variables. For the sake of computational efficiency, the elastic-viscous-plastic (EVP) formulation of Hunke and Dukowicz (1997) is often chosen to describe the sea ice rheology within the dynamical component. Due to its horizontal heterogeneity, the sea ice extent varies quite a lot over an ice floe, with typical scale ranges from 1m to 100km. As illustrated in Figure 1.8, one way to account for this feature is to introduce a subgrid-scale distribution of ice thickness. For

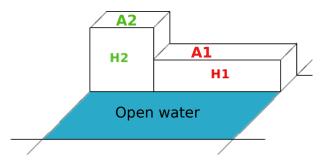


Figure 1.8: Illustration of the representation of the ice thickness distribution in a grid cell for two sea ice categories/concentrations and open water.

the sake of simplicity, only two different states of sea ice are considered with an open water area, in this example. Indeed, each category has a mean thickness (H1,H2) and an associated relative coverage of the grid cell (A_1,A_2) . Thanks to this ice thickness distribution (ITD) (Thorndike et al., 1975), the ice pack is described in terms of relative coverage of different thicknesses, which is very interesting since many sea ice properties are strongly dependent on the ice thickness (rate of growth, surface temperature, turbulent and radiative heat exchanges with atmosphere, salt content and potential energy). This model consists in describing the large-scale consequences of the small-scale processes

involved in the ice thickness evolution. The thickness distribution g(h) can be defined as follows:

$$\int_{h_1}^{h_2} g(h)dh = \frac{A(h_1, h_2)}{R},\tag{1.4}$$

where R is the ice pack area of the region considered and $A(h_1, h_2)$ is the area within R covered by ice of thickness h in the range $h_1 \leq h \leq h_2$. Integrated on a defined domain $[0, h_{max}]$, one has:

$$\int_0^{h_{max}} g(h)dh = 1, \tag{1.5}$$

and, outside these boundaries, g(h) vanishes. Two types of phenomena alter the ice thickness, and thus g(h): the thermodynamic and mechanical processes. In taking into account both their influences, the governing equation for the thickness distribution can be written as:

$$\frac{\partial g}{\partial t} = -\nabla \cdot (\underline{v} \ g) - \frac{\partial}{\partial h} (f \ g) + \Psi, \tag{1.6}$$

where f[m/s] is the growth rate function and \underline{v} g is the flux of thickness distribution and the effects of the mechanical ridging and opening processes are represented in the redistribution function Ψ . On the one hand, the transfer between the categories due to thermodynamics comes from the growth and melt, and the distribution will tend naturally towards an uniform thickness. In order to parameterize the thermodynamic thickening of ice, f is built and its magnitude is determined by the balance of the atmospheric and oceanic heat fluxes at the bottom and top of the ice, its thermal history, its thickness, the snow cover and the distribution of brine inclusions within the ice. But the ice thickness also influences the rate of heat input to the atmosphere and ocean. For instance, Badgley (1966) reports that "the turbulent heat input to the atmosphere over a refreezing lead is more than 2 orders of magnitude larger than that over typical 3-m ice. Thus if leads account for 1% or more of the ice pack, their effects can begin to dominate the large-scale turbulent heat exchange and alter boundary layer stability". On the other hand, the dynamic processes result from the nonuniform motions of the ice that create leads and pressure ridges. In state of divergence, new areas of open water appear, whereas the convergence tends to close open water areas, and sometimes, the thin ice is rearranged to build a ridge. Besides, the shear occurs through slip along some cracks and can cause leads and pressure ridges. Thick and thin ice covers do not vary in the same way in the same area. Indeed, thin ice offers little resistance to compression whereas thick ice, for example over 1m, is very strong. As the ice moves, q(h) must also vary in function of the advection of the areas of the different thicknesses into the region R. In the latter, the rearrangement of ice in R is expressed as sources and sinks of the ice area of



Figure 1.9: Illustrations of pressure ridges (left,[http://www.arctic.noaa.gov/ice-rubble-pressure.html]) and leads (right, [Courtesy S. L. Farrell]).

each category. Of course, it depends on h, on the strain rate and g. In state of pure divergence, area of open water can appear, this assumed area is exported from R. In case of pure convergence, there is a flux of ice into R so that Ψ must mimic the rearrangement of the ice already present in R to take up less place. The thin ice is then taken from a range of ice thicknesses, not especially the thinnest, and pressure ridges are created in increasing the area covered by thick ice and decreasing the area covered by thin ice. Once the thickness distribution has been applied, this new configuration on the grid cell is used to conservatively remap all the other global sea ice variables, such as the heat content or temperature, in the same way than the thickness.

The parameterization of the ITD is already included in the sea ice model LIM3 (Vancoppenolle et al., 2009b), where 5 categories are considered to describe the ice thickness. LIM3 also takes into account the halodynamics through empirical parameterizations for gravity drainage and percolation of brine (Vancoppenolle et al., 2005), so that each ice thickness category is divided into 5 layers for sea ice halo-thermodynamics. The evolution of the salinity profile is computed from basal ice formation, snow ice formation, gravity drainage and flushing and is given for thermodynamic computations. The sea ice dynamics is solved by using the EVP rheology of Hunke and Dukowicz (2001) in the C-grid formulation of Bouillon et al. (2009). This configuration already provides a sea ice model with a sophisticated representation of the sea ice physics but new parameterizations could still be added. Some other parameterizations relative to thermodynamic processes could be included, for instance, a surface albedo which evolves according to meltpond coverage or the penetration of shortwave radiation into snow (Notz, 2012). Besides, some additional parameterizations about subgrid-scale dynamic processes could also be included, for instance the bottom and surface roughness related to the ice-thickness distribution. The question is what it the best balance between the parameterizations and the

improvements of the results. The question remains whether these new parameterizations always bring better skills with respect to observations or not.

1.4 Objectives of the thesis

The use of parameterizations of subgrid-scale processes is widespread in GCMs, both in their oceanic and sea ice components. Their inclusion in finite element sea ice-ocean models is not straightforward and, hence, is investigated throughout this thesis. A pertinent choice must be made among all the physical processes that can potentially be parameterized and among the various available methods. A newly parameterized process within a model must not be too computationally expensive and provide concrete improvements of the model skills. As discussed previously, such parameterizations have been shown to bring significant improvements in the capabilities of ocean models (e.g. sharper main thermocline; Danabasoglu and McWilliams, 1995) but produce unwanted model behaviours in particular cases (e.g., dissipation, diffusion fluxes in the wrong directions or infinite values; Griffies, 2004). So as to prevent this, numerical artefacts are used, for instance the tapering functions or matching conditions (Gent et al., 1995; Redi, 1982).

How to reduce the use of numerical artefacts associated with those parameterizations to the benefit of their physics?

Chapters 2 and 3 present the parameterization of mesoscale eddies, which are usually treated as two distinct processes: the isopycnal diffusion and the GM velocity, that are computed as suggested by Redi (1982) and Gent and McWilliams (1990), respectively. Their inclusion influences the ocean results obtained by means of SLIM and these effects are highlighted through these chapters.

First, the mixing of tracers by mesoscale eddies mainly occurs along the isopycnals, but another diffusion, called diapycnal, occurs orthogonally to these surfaces with a weaker magnitude. This situation leads to a strong anisotropy in the diffusivity tensor. Since SLIM is discretized with a discontinuous Galerkin finite element method, the interior penalty terms are introduced to yield a compact scheme. In particular, the penalty factor which penalizes the jump of tracer over the edges of the elements, is required to stabilize the discontinuous Galerkin finite element method. However, its estimation is not an easy task because it influences the results. If the penalty factor is too small, the numerical scheme becomes unstable. But, if it is too large, too much numerical diffusion is introduced, which damages the approximate solution. In Chapter 2, the oriented penalty factor, defined by rotating the system to align it with the principal axes of the diffusivity tensor, is assessed through a comparison with

another penalty factor (the eigenvalue penalty factor, inspired by the work of Rivière (2008)). Next, our study highlights the difference of order in the value of each penalty factor. In a simple test case, the evolution of a tracer concentration, placed in a density field where the isopycnals are plane and equally spaced, is investigated. Even if the eigenvalue penalty factor yields a smoothed concentration field, the values of the oriented penalty factor are smaller with larger jumps between the elements in the numerical solution. This difference in the fields shows that too much numerical diffusion is induced with the eigenvalue penalty factor. In addition, our study over the numerical errors indicates that the oriented penalty factor, which stabilizes the numerical system sufficiently, induces less errors.

Larger values of the penalty factor can also affect the efficiency of the numerical scheme through an ill-conditioned system. With standard penalty factors, the model inability to solve the linear system with strong anisotropies emphasizes the need for a well-conditioned system. Using the condition number, the accuracy of the system can be measured: when the condition number is close to 1, the system allows to get an accurate solution. The oriented penalty factor gives the best condition number whatever the order. Besides, it allows to reduce the computational effort contrary to the eigenvalue penalty factor.

Another characteristic of the isopycnal diffusion could lead to numerical errors in the approximated solution: the main directions of the isopycnal and diapycnal diffusions are not aligned with the mesh axes. Despite the fact that the slope of the isopycnal surface does not exceed 0.01, a small angle of 1° leads to differences in the spatial convergence. With a coarse test mesh (10km), the oriented penalty factor yields the best spatial convergence. The oriented penalty factor was thus selected for further applications. In Chapter 3, the tracer concentration, initialized as a Gaussian, really tends to follow the isopycnals in a progressively inclining density field. The choice of the oriented penalty factor do not seem to affect the solution or produce some unwanted behaviours. Last but not least, numerical errors may appear in the wrong direction of diffusivity flux. When only the isopycnal diffusion is considered, i.e., no diapycnal diffusion is assumed, the tracer concentration should only be diffused in the isopycnal direction. In practice, a spurious flux appears in the diapycnal direction. As its variance grows linearly with time, it can be defined as a spurious diffusivity in the diapycnal direction (Karger, 1992), and this spurious diffusivity appears to be weaker than the real diapycnal diffusivity. These investigations allow to show that the physical processes behind the parameterization associated to the isopycnal diffusion are preserved.

As already mentioned, the one-dimensional boundary value problem suggested by Ferrari et al. (2010) allows to avoid the use of additional tapering

functions in order to naturally ensure impermeable boundaries in the computation of the GM velocity. In Chapter 3, an idealized channel simulation reveals the expected effects on the temperature field when the GM velocity is parameterized in SLIM. Without this parameterization, the isotherms are getting extremely steep under the action of wind because the transient motions are not sufficient to smooth the density slopes. When the GM parameterization is taken into account, this undesirable feature is not noticed anymore: the available potential energy is released in such a way that the isotherms are slumped. Moreover, the stratification close to the ocean surface is greatly influenced by this mesoscale parameterization. While minimizing the use of numerical artifices, the expected oceanic behaviours such as the slumped isopycnals, seem to be well estimated in SLIM applications.

Several sea ice models (e.g., Salas-Mélia et al., 2005; Hunke et al., 2013; Vancoppenolle et al., 2009b) based on the structured grids already use some parameterizations to describe subgrid-scale processes, such as the ice thickness distribution or the halodynamics, but these parameterizations were, until now, never included in a model discretized on unstructured meshes. This second objective of this thesis concerns the new sea ice-ocean coupled model FESOM-LIM3.

What are the interest and potential applications of having a state-of-the-art representation of the sea ice physics on an unstructured mesh?

In Chapter 4, key components of LIM3 are coupled to the global ice-ocean model FESOM in order to gather the advantages of each model. With the unstructured mesh used in FESOM, the coastlines are well represented and places of particular interest can be locally refined. While the sea ice thermodynamics in FESOM remains relatively simple, LIM3 offers the possibility of representing the ice thickness distribution and includes a state-of-the-art representation of the sea ice halo-thermodynamics. Some technical adaptations have been realized in order to perform realistic simulations of sea ice state over the 1979-2007 period.

In Chapter 5, the simulated general sea ice physical state variables are studied: the ice areal coverage, thickness and volume, as well as the ice velocity, in both Hemispheres. Thanks to this coupled model, some regions which were, until now, often unresolved or represented with a coarse resolution, can be studied in more details. In the previous works, LIM3 was used with at best, a structured grid of 1° of horizontal resolution so that only two channels were represented in the Canadian Arctic Archipelago. Thanks to the unstructured mesh, all its narrows straits are reproduced. The simulated mean ice

concentration is evaluated against the satellite observations in terms of spatial and seasonal variability. While FESOM overestimated the ice concentration throughout the year which leaded to almost no variation in ice concentration in the Canadian Arctic Archipelago, FESOM-LIM3 performs better or presents specific patterns, such polynyas in the Amundsen Gulf and Smith Sound, as well as the open area water in the Foxe Basin. Through the main gates of the Arctic basin, the simulated solid freshwater fluxes are in very good agreement with the various observations. Contrary to expectations, the net export in the Bering Strait is slightly negative which means that the solid freshwater tends to go out of the Arctic basin. This feature was already observed in other GCMs (MRI-A, MRI-F, FSU-HYCOM) but no explanation was so far provided. A possible solution could be to decrease the atmosphere-ice drag slightly. As the ice thickness distribution tends to give thinner ice in the marginal areas, the ice is easier exported through the gate. Finally, the seasonal solid freshwater flux in the Fram Strait is especially well represented by FESOM-LIM3 with a continuous ice export all over the year in the range of the observations. As for the Southern Hemisphere, the ice drafts in the Weddell sea are also underestimated in comparison to the ULS observations, which again could be due to the too small lead closing parameter for this area. Despite that, the freezing and melting timing phases in the simulated time series remain realistic.

The improvements brought by the multi-category formalism to sea ice models running on structured grids can therefore be expected on unstructured meshes, but it is not trivial. Including a more sophisticated representation of sea ice physics and having a finer mesh resolution at high-latitudes should lead to some improvements in the simulations, provided that parameters in this new coupled model are properly calibrated. In order to achieve such calibrations, further test experiments are required.

C H A P T E R

Strongly anisotropic diffusion operator

In the framework of SLIM, the isopycnal diffusion is discretized with the discontinuous Galerkin finite element method (dgFEM). Contrary to the continuous method, where the solution is continuous on all the discretized space, the

dgFEM gives a solution which is approximated on each element separately so that some discontinuities (called jumps) appear at the element boundaries, as shown on the right hand-side picture. With this discretization, the diffusion requires penalty terms in order to stabilize the numerical scheme. With the particularly strong anisotropy in the isopycnal diffusivity tensor, the penalty factor is not well-adapted since it has not been built in order to follow the



isopycnals. Initially dependent on a scalar diffusivity, it tends to induce diapycnal diffusion and thus deteriorates the solution. The major challenge is then to define this penalty factor in a different way to deal with the isopycnal diffusion correctly. The penalty factor choice is important since a larger value damages the solution accuracy and a smaller one leads to instabilities within the numerical scheme.

This Chapter is based on the following paper, published on 20 June 2014: A. Pestiaux, S.A. Melchior, J.F. Remacle, T. Kärnä, T. Fichefet and J. Lambrechts. Discontinuous Galerkin finite element discretization of a strongly anisotropic diffusion operator. *Inter. J. Num. Meth. Fluids*, 75:365-384,2014.

Abstract

The discretization of a diffusion equation with a strong anisotropy by a discontinuous Galerkin finite element method is investigated. This diffusion term is implemented in the tracer equation of an ocean model thanks to a symmetric tensor which is composed of diapycnal and isopycnal diffusions. The strong anisotropy comes from the difference of magnitude order between both diffusions. As the ocean model uses interior penalty terms to ensure numerical stability, a new penalty factor is required in order to correctly deal with the anisotropy of this diffusion. Inspired by the literature, two new penalty factors have been established from the coercivity property. One of them takes into account the diffusion in the direction normal to the interface between the elements. After comparison, the oriented penalty facotr appears to be the best since the spurious numerical diffusion is weaker than with the penalty factor proposed in the literature. It is computed with a transformed coordinate system in which the diffusivity tensor is diagonal, using its eigenvalue decomposition. Furthermore, the numerical scheme associated with the oriented penalty factor is validated with the Method of Manufactured Solutions. It is finally applied to simulate the evolution of temperature and salinity due to turbulent processes in an idealized Arctic Ocean.

2.1 Introduction

In ocean general circulation models, all physical processes cannot be resolved explicitly due to insufficient spatial resolution. Hence, appropriate parameterizations are required in order to account for those processes. Iselin (1939) and Montgomery (1940) suggested that the mixing of tracers by mesoscale eddies in the stratified ocean mainly occurs along the surfaces of constant density, i.e., the isopycnals. It appears that some smaller processes also mixed the tracers but orthogonally to the isopycnals, so that these surfaces are called diapycnals. Even with its small magnitude, the diapycnal diffusion should also be taken into account in the parameterization of the mesoscale eddies. This situation creates a strong anisotropy in the diffusion tensor. In order to model the effects of this anisotropic turbulence and transport along and accross isopycnals, Redi (1982) considered a new isopycnal mixing tensor where the main axes of diffusivity have been rotated from the standard cartesian coordinates towards any direction where there is a density gradient. The isopycnal diffusivity operator is then built as a non-linear function of the active tracer concentrations since the diffusion operator depends on the density which, in turn, is a function of salinity and temperature (Gent and McWilliams, 1990). This operator differs fundamentally from isotropic and homogeneous diffusion since the tensor is not diagonal or constant. But, as in most ocean general circulation models used in climate studies, the main directions of the diffusion are not aligned with the mesh and this can create numerical errors.

In the present work, only the tracer equation from a ocean model is considered. Even if many processes can influence the evolution of oceanic tracers, such as the advection or the vertical mixing, we focus only on the isopycnal diffusion, which is discretized with a Discontinuous Galerkin Finite Element Method (DGFEM) since it is developed in the framework of an unstructured grid oceanic model, the Second-generation Louvain-la-Neuve Ice-ocean Model (SLIM¹, Blaise et al., 2010; Kärnä et al., 2012; White et al., 2008a). Even if advection is not present in this study, this is an important ocean process that cannot be forgotten for a realistic oceanic simulation. When the advection term is present, DGFEM is better adapted than the continuous Galerkin (CG) method since the numerical dissipation is lower than in CG for an equivalent mesh and the dispersion is optimal (Ainsworth, 2004). For the last thirty years, DGFEM has been used to solve partial differential equations in engineering applications, but the anisotropy of these models was much less than in the ocean (Lesaint and Raviart, 1974; Reed and Hill, 1973). In a natural way, the numerical fluxes and the slope limiters were introduced (Cockburn et al., 2000). The DGFEM allows to approximate the solution on each element separately and some discontinuities, called jumps, can appear at the interface of the elements (Douglas, 1982). For these many reasons, SLIM has been developed with DGFEM and, as this oceanic model is employed and improved, the DGFEM is used instead of the CG. In the framework of SLIM, interior penalty terms are introduced to yield a compact scheme. Especially, the estimation of the penalty factor is required to stabilize the finite element method.

In the ocean, the anisotropy is quantified thanks to a factor ϵ , named anisotropy factor. Its high magnitude, which comes from the ratio between the maximum and minimum eigenvalue of the diffusivity tensor, λ_M and λ_m , respectively, is not usual in standard engineering analysis, such as in the composite materials or in petroleum geology (Hohn, 159, 1999). The derivation of the penalty factor is not an easy task since it influences the results. If it is too small, the numerical scheme becomes unstable. But, if it is too large, too much numerical diffusion is introduced and this reduces the quality of the approximate solution. Houston et al. (2002) analyzed the discretization of the advection-diffusion equation with a discontinuous Galerkin method when the diffusivity is heterogeneous and less anisotropic than in the ocean. As the local and small diffusivity in some parts of the domain can influence the internal layers if there is advection, Gastaldi and Quarteroni (1990), Croisille et al. (2005) and Pietro et al. (2008) investigated the regions where the diffusion vanishes and reappears further. The discontinuity-penalization parameter does not take

 $^{^{1}}http://www.climate.be/slim/$

into account the direction and is thus not appropriate when the diffusivity is anisotropic.

In her book, Rivière (2008) has proposed a DGFEM interior penalty method that is able to deal with moderate anisotropic diffusion. In practical case, the mesh is usually aligned with the direction of anisotropy. Consider the Laplace problem

$$\frac{\partial^2 C}{\partial x^2} + \frac{\partial^2 C}{\partial y^2} = 0 \tag{2.1}$$

on a uniform mesh made of squares where C is a tracer (see Figure 2.1). Consider a change in coordinate $y' \mapsto hy$ which leads to

$$\frac{\partial^2 C}{\partial x^2} + h^2 \frac{\partial^2 C}{\partial y'^2} = 0 \tag{2.2}$$

An anisotropy of h^2 can exactly be balanced using a mesh that is stretched by a factor h in the direction of anisotropy. One design goal of our approach would be that a numerical solution obtained for the equation (2.1) on a uniform mesh would be strictly the same as the numerical solution obtained for the equation (2.2) on a mesh that is stretched by a factor h in the y direction. Rivière's approach deals separately with the anisotropy of the diffusion tensor and with the anisotropy of the mesh. With the kind of anisotropy that is present in ocean modeling, penalty factors computed with Rivière's approach are very high. The corresponding linear systems are so ill-conditioned that they cannot be inverted. Actually, the Rivière penalty factor demonstrates its effectiveness when the anisotropy is small and local. In this paper, we want to have a method as accurate as the Rivière method but practicable for complex simulations. We therefore suggest an improvement to this penalty factor in

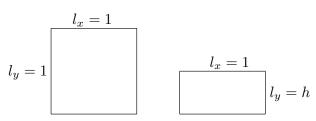


Figure 2.1: Illustration of two meshes with their respective side lengths l_x and l_y .

order to reduce it while preserving the numerical stability. It will be referred to as the eigenvalue penalty factor.

Ern et al. (2008) suggested another penalty factor. He applied a weighted average method to the diffusivity tensor in the direction normal to the interface

between the elements. The use of this factor without the average method is quite intuitive. There is, to the best of our knowledge, no formal demonstration of the use of the penalty factor suggested by Ern. In this paper, we will first prove that this penalty factor without the weighted average, which is called here the *oriented penalty factor*, is sufficient to ensure the coercivity even for strong anisotropic diffusions. The coercivity ensures that the solution is well-posed, i.e., the uniqueness and continuity properties are satisfied. The latter is defined by rotating the system to align it with the principal axes of the diffusivity tensor. Afterwards, the more appropriate penalty factor for a strong anisotropic diffusion will be determined between the eigenvalue penalty factor and the *oriented penalty factor*. That will allow to have, not only the numerical scheme stabilization, but also less numerical diffusion and thus a better approximation of the solution. If a simple example is taken where the anisotropic diffusion is defined as

$$\kappa = \begin{pmatrix} 1 & 0 \\ 0 & \alpha \end{pmatrix},$$

where α is assumed to be smaller than 1, a first approximation of each penalty term can be theoretically computed (Table 2.1). As expected, the Rivière

Table 2.1: Comparison of an approximation of the penalty term for the Rivière, the eigenvalue and the oriented methods.

penalty factor remains large whatever the direction. The eigenvalue penalty factor is a little better, whereas the oriented penalty factor which changes with the main axes diffusion seems the best.

The paper is organized as follows. The diffusion tensor is defined in Section 2. The DGFEM is applied to the diffusion equation in Section 3. Section 4 presents both penalty factors discussed here, and compares them. The Method of Manufactured Solutions is applied in Section 5. A physical application is suggested in Section 6. Finally, concluding remarks close the paper in Section 7.

2.2 Diffusion equation

In the framework of SLIM, the unstructured meshes are composed of several layers of triangular prisms. As the elements are triangular at the surface, the coastlines can be represented with high geometrical flexibility. Additionally,

the mesh is structured along the vertical direction, which preserves the natural stratification of the ocean. Each tracer concentration field $C(\underline{X},t)$, typically the temperature T or the salinity S, satisfies the following diffusion equation:

$$\frac{\partial C}{\partial t} = \nabla \cdot (\underline{\underline{\kappa}} \cdot \nabla C), \tag{2.3}$$

where $\underline{\kappa}$ is the diffusivity tensor. This symmetric tensor is computed from the density ρ , which is itself a function of T and S through the equation of state. The density is a three-dimensional function implying that the dimension d=3 and $\underline{X}=(x,y,z)$. Initial conditions $C(\underline{X},0)$ are supposed to be given and no normal flux of both temperature and salinity is allowed on the boundary $\partial\Omega$ of the domain $\Omega\subset R^d$. The normal \underline{n} is defined everywhere on the boundary of the elements. From the density ρ , the slope² \widetilde{s} is obtained as:

$$\widetilde{s} = [s_x, s_y] = -\frac{\nabla_h \rho}{\partial \rho / \partial z},$$
(2.4)

where $\nabla_h = (\partial_x, \partial_y)$. Let us now define $\underline{\nu} = -\nabla \rho$ and create the diapycnal unit vector:

$$\widehat{\underline{\nu}} = \frac{\underline{\nu}}{\|\underline{\nu}\|} = \frac{[s_x, s_y, -1]}{\sqrt{s_x^2 + s_y^2 + 1}},$$

where $\|\cdot\|$ is the Euclidean norm. The \widetilde{s} and $\underline{\nu}$ vectors are important since the anisotropic diffusion in the ocean is oriented along and across the density slope. The diffusivity tensor $\underline{\kappa}$, which is made up of isopycnal and diapycnal parts, can then be expressed as:

$$\underline{\kappa} = A^{I}(\underline{\delta} - \underline{\widehat{\nu}} \ \underline{\widehat{\nu}}) + A^{D} \ \underline{\widehat{\nu}} \ \underline{\widehat{\nu}},$$

where $\underline{\delta}$ is the Kronecker delta and A^I and A^D are the non negative isopycnal and diapycnal diffusivity coefficients, respectively Griffies et al. (1998). Using the local density slope \widetilde{s} , Redi (1982) showed that the tensor $\underline{\kappa}$ in the (x,y,z) reference frame can be written as³:

$$\underline{\underline{\kappa}} = \frac{A^{I}}{1 + \|\widetilde{s}\|^{2}} \begin{pmatrix} 1 + s_{y}^{2} + \epsilon s_{x}^{2} & (\epsilon - 1)s_{x}s_{y} & (1 - \epsilon)s_{x} \\ (\epsilon - 1)s_{x}s_{y} & 1 + s_{x}^{2} + \epsilon s_{y}^{2} & (1 - \epsilon)s_{y} \\ (1 - \epsilon)s_{x} & (1 - \epsilon)s_{y} & \epsilon + \|\widetilde{s}\|^{2} \end{pmatrix}, \tag{2.5}$$

 $^{^2{}m The}$ tilde refers to a two-dimensional vector, whereas the underline refers to a three-dimensional vector.

³The equality between $\underline{\underline{\kappa}}$ and its components should not be written because the former is a tensor, i.e., a mathematical object that does not depend on any basis, while the latter is the matrix obtained by expressing the former in a particular basis. The formal link between the tensor and its components κ_{ij} is simply $\underline{\underline{\kappa}} = \kappa_{ij} e_i e_j$ where Einstein convention is used and e_i is the basis vector in direction $i = \{1, 2, 3\}$. This kind of equality is however used in this chapter for the sake of easier reading.

where $\epsilon = \frac{A^D}{A^I}$ is the ratio of the diapy cnal diffusivity to the isopycnal diffusivity.

2.3 DGFEM formulation

In this study, the elements Ω_e are prisms with vertical faces (Wang et al., 2008) and P_1^{DG} shape functions, i.e. polynomials of degree p=1, are chosen in each element (implying that the number of nodes in the element is N=6). Note that the index e refers to a specific element, whereas the index e refers to an interface between two elements. The usual Galerkin finite element formulation of the tracer equation is:

$$\begin{split} & \int_{\varOmega} \left(\frac{\partial C}{\partial t} - \nabla \cdot \left(\underline{\underline{\kappa}} \cdot \nabla C \right) \right) \ \tau \ d\varOmega = 0 \\ \Leftrightarrow & \int_{\varOmega} \frac{\partial C}{\partial t} \tau \ d\varOmega = \int_{\varOmega} \nabla \tau \cdot \underline{\underline{\kappa}} \cdot \nabla C \ d\varOmega - \int_{\partial \varOmega} \underline{n} \cdot \underline{\underline{\kappa}} \cdot \nabla C \ \tau \ d\Gamma, \end{split}$$

where τ is the shape function. The integral over the whole domain Ω is decomposed into the sum of integrals over each element Ω_e and each interface $\gamma_k = \Omega_e \cap \Omega_{e'}$. The set of all element interfaces is noted $\Gamma = \bigcup_k \gamma_k$. The interface term is computed over each face:

$$\sum_{e} \int_{\Omega_{e}} \frac{\partial C}{\partial t} \tau \ d\Omega = \sum_{e} \int_{\Omega_{e}} \nabla \tau \cdot \underline{\underline{\kappa}} \cdot \nabla C \ d\Omega - \sum_{k} \int_{\gamma_{k}} \underline{n} \cdot \underline{\underline{\kappa}} \cdot \nabla C \ \tau \ d\Gamma. \quad (2.6)$$

Instead of incorporating boundary conditions in the space, Dirichlet boundary conditions are directly weakly imposed through the penalty factor (Arnold et al., 2000). In DGFEM, the weak formulation consists in finding C such as $a(C,\tau)=b(\tau)$, where a is a bilinear form and b is a linear form. The right-hand side term of equation (2.6) is indeed the bilinear form (Rivière, 2008), which is

defined as:

$$a(C,\tau) = \sum_{e} \int_{\Omega_{e}} \nabla \tau \cdot \underline{\kappa} \cdot \nabla C \, d\Omega$$

$$-\sum_{k} \int_{\gamma_{k}} \left([[\tau]] \cdot \{\underline{\kappa} \cdot \nabla C\} + [[C]] \cdot \{\underline{\kappa} \cdot \nabla \tau\} \right) \qquad (2.7)$$

$$+\sum_{k} \int_{\gamma_{k}} \mu[[C]] \cdot [[\tau]] \, d\Gamma$$

$$= \sum_{e} \int_{\Omega_{e}} \nabla \tau \cdot \underline{\kappa} \cdot \nabla C \, d\Omega - \sum_{k} \int_{\gamma_{k}} [[\tau]] \cdot \{\underline{\kappa} \cdot \nabla C\} \, d\Gamma$$

$$\underbrace{-\sum_{k} \int_{\gamma_{k}} [[C]] \cdot \{\underline{\kappa} \cdot \nabla \tau\} \, d\Gamma}_{\mathbf{Q}} + \underbrace{\sum_{k} \int_{\gamma_{k}} \mu[[C]] \cdot [[\tau]] \, d\Gamma}_{\mathbf{Q}}, \quad (2.8)$$

where μ is the penalty factor and [[.]] is the jump vector at the interface such that $[[C]] = n \frac{C^+ - C^-}{2}$, with C^+ and C^- being the tracer on the left- and right-hand sides, respectively (Cockburn et al., 2000). The term $\mathbb Q$ comes from the divergence theorem and the integration by parts. The interior penalty (IP) terms, i.e., the symmetric interior penalty term $\mathbb Q$ and the penalty term $\mathbb Q$, stabilize the diffusion in the DGFEM. The value of μ must be chosen carefully. On the one hand, if μ is not large enough, the bilinear form is not coercive and the approximate solution is not stable. In this case, numerical artifacts, such as spurious oscillations, that deteriorate the quality of the solution appear. On the other hand, if μ is too large, the solution exhibits too much numerical diffusion and modifies the effective value of the diffusivity tensor. Moreover, the numerical schemes will not be efficient. For instance, a large value of μ can have a detrimental effect on the conditioning of the matrix that represents the bilinear form (Shahbazi, 2004).

2.4 Interior penalty factor

The factor μ penalizes the jump of the concentration tracer C over the edge of an element. For scalar diffusivity, Shahbazi (2004) derives a penalty factor which is a function of the dimension d, the degree of the polynomial shape function D_p , the area of the interface A and the volume of the element V:

$$\mu = \frac{(D_p + 1)(D_p + d)}{d} \frac{n_0}{2} \frac{A}{V} \kappa, \tag{2.9}$$

where n_0 is the number of neighbors of the element, i.e., $n_0 = 5$ for prisms, and κ is a scalar diffusivity. As the diffusion is represented by an anisotropic

diffusivity tensor, this usual penalty factor cannot be used directly.

In the next sections, two different ways of computing the penalty factor that take into account the anisotropic diffusivity are discussed. Firstly, Rivière (2008) only uses the lower and upper bounds of the eigenvalues of the tensor. As this suggested penalty factor is too large, a new penalty factor inspired from Rivière (2008) has been developed and called eigenvalue penalty factor. In this new configuration, the previous maximum eigenvalue used in the penalty factor suggested by Rivière (2008) is replaced in order to reduce the numerical diffusion, which leads thus to a better performance. But the tries with the eigenvalue penalty factor were not convincing. Secondly, the proof of the oriented penalty factor, which is a function of $\underline{n} \cdot \underline{\kappa} \cdot \underline{n}$, is introduced. This factor is defined by rotating the system to align it with the principal axes of the diffusivity tensor and a value is suggested when strong anisotropy exists in the diffusivity tensor.

2.4.1 Eigenvalue penalty factor

In the case of a small anisotropic diffusivity, Rivière (2008) suggested to replace the penalty factor (2.9) by the penalty factor μ defined with the eigenvalues of the diffusivity tensor:

$$\mu = \frac{(D_p + 1)(D_p + d)}{d} \frac{n_0}{2} \frac{A}{V} \frac{\lambda_M^2}{\lambda_m},$$
(2.10)

where λ_m and λ_M are the minimum and maximum eigenvalues of the diffusivity tensor, respectively. Even though the anisotropy in the new diffusivity tensor is considered, this penalty factor returns excessive values whenever $\frac{\lambda_M^2}{\lambda_m}$ is large.

It is possible to find sharper bounds for μ when anisotropy is very large. The penalty factor must be chosen so that the bilinear form $a(C, \tau)$ is coercive, i.e., there exists a positive constant c_1 such that:

$$c_{1} \|C\|_{S}^{2} \leq a(C, C)$$

$$\leq \sum_{e} \int_{\Omega_{e}} \nabla C \cdot \underline{\kappa} \cdot \nabla C \ d\Omega - 2 \sum_{k} \int_{\gamma_{k}} \{\underline{n} \cdot \underline{\kappa} \cdot \nabla C\}[[C]] \ d\Gamma$$

$$+ \sum_{k} \int_{\gamma_{k}} \mu[[C]]^{2} \ d\Gamma, \qquad (2.11)$$

where τ has been replaced by C in equation (3.7) and the norm assocated to the Broken Sobolev space is $\|C\|_S^2 = \sum_e \int_{\Omega_e} \|\nabla C\|^2 \ d\Omega + \sum_k \int_{\gamma_k} [[C]]^2 \ d\Gamma$. As the aim is to ensure the coercivity, a(C,C) must be limited by something that is smaller. Using the arithmetic-geometric mean inequality $-2\alpha\beta \ge -\epsilon_V^{-1}\beta^2$

 $\alpha^2 \epsilon_Y$ with the strictly positive scalar ϵ_Y , the equation becomes:

$$a(C,C) \geq \sum_{e} \int_{\Omega_{e}} \nabla C \cdot \underline{\kappa} \cdot \nabla C \, d\Omega - \frac{1}{\epsilon_{Y}} \sum_{k} \int_{\gamma_{k}} \{\underline{n} \cdot \underline{\kappa} \cdot \nabla C\}^{2} \, d\Gamma + \sum_{k} \int_{\gamma_{k}} (\mu - \epsilon_{Y}) [[C]]^{2} d\Gamma, \qquad (2.12)$$

where α has been replaced by [[C]] and β by $\{\underline{n} \cdot \underline{\underline{\kappa}} \cdot \nabla C\}$. Using the geometric law $(m^+ + m^-)^2 \leq 2(m^+)^2 + 2(m^-)^2$, the second term can be bounded as follows:

$$\sum_{k} \int_{\gamma_{k}} \{ \underline{n} \cdot \underline{\underline{\kappa}} \cdot \nabla C \}^{2} \ d\Gamma \leq \frac{1}{2} \sum_{k} \int_{\gamma_{k}} \left(\left(\underline{n} \cdot \left(\underline{\underline{\kappa}} \cdot \nabla C \right)^{-} \right)^{2} + \left(\underline{n} \cdot \left(\underline{\underline{\kappa}} \cdot \nabla C \right)^{+} \right)^{2} \right) d\Gamma,$$

where the signs $(\cdot)^+$ and $(\cdot)^-$ refer respectively to the values of the variable on the left- and right-hand sides of the interface. In order to bound the diffusivity tensor, $\underline{\kappa}$ is considered constant on each element so that:

$$\sum_{k} \int_{\gamma_{k}} \{ \underline{n} \cdot \underline{\kappa} \cdot \nabla C \}^{2} d\Gamma \leq \frac{1}{2} \sum_{k} \left(||\underline{n} \cdot \underline{\kappa}^{-}||^{2} \int_{\gamma_{k}} ||\nabla C^{-}||^{2} d\Gamma \right) + ||\underline{n} \cdot \underline{\kappa}^{+}||^{2} \int_{\gamma_{k}} ||\nabla C^{+}||^{2} d\Gamma \right).$$
(2.13)

The trace inequality (Warburton and Hesthaven, 2003):

$$\forall \gamma_k \in \Omega_e \quad \int_{\gamma_k} P^2 d\Gamma \le \int_{\Omega_e} c_s \frac{A_k}{V_e} P^2 d\Omega, \tag{2.14}$$

where $c_s = \frac{(O_p+1)(O_p+d)}{d}$ and O_p is the number of degrees of freedom of the polynomial P, is now used. Since O_p is related to the gradient of the tracer concentration, it is equal to D_p-1 and thus $c_s = \frac{D_p(D_p-1+d)}{d}$. The inequality (2.13) can then be written as:

$$\sum_{k} \int_{\gamma_{k}} \{ \underline{n} \cdot \underline{\underline{\kappa}} \cdot \nabla C \}^{2} d\Gamma \leq \frac{c_{s}}{2} \sum_{e} \left(\sum_{k \in e} \frac{A_{k}}{V_{e}} ||\underline{n} \cdot \underline{\underline{\kappa}}||^{2} \right) \int_{\Omega_{e}} ||\nabla C||^{2} d\Omega. (2.15)$$

Moreover, the first part of the inequality (2.11) can be bounded as follows:

$$\int_{\Omega_e} \nabla C \cdot \underline{\underline{\kappa}} \cdot \nabla C \ d\Omega \ge \int_{\Omega_e} \lambda_m ||\nabla C||^2 \ d\Omega. \tag{2.16}$$

Using the inequalities (2.15) and (2.16), the bilinear form can be written as:

$$a(C,C) \geq \sum_{e} \left(\lambda_{m} - \frac{c_{s}}{2\epsilon_{Y}V_{e}} \sum_{k \in e} A_{k} ||\underline{n} \cdot \underline{\underline{\kappa}}||^{2} \right) \int_{\Omega_{e}} ||\nabla C||^{2} d\Omega$$

$$+ \sum_{k} (\mu - \epsilon_{Y}) \int_{\gamma_{k}} [[C]]^{2} d\Gamma. \tag{2.17}$$

In order to ensure the coercivity $a(C,C) > c_1||C||_S^2$, two conditions are required:

$$\begin{cases} \mu - \epsilon_Y = c_1 > 0, \\ \lambda_m - \frac{c_s}{2\epsilon_Y V_e} \sum_{k \in e} A_k ||\underline{n} \cdot \underline{\kappa}||^2 \ge 0. \end{cases}$$

These conditions are satisfied if μ is chosen such as:

$$\mu > \epsilon_Y \ge \frac{c_s}{2\lambda_m V_e} \sum_{k \in e} A_k ||\underline{n} \cdot \underline{\underline{\kappa}}||^2.$$

In order to correctly understand the meaning of this new penalty factor, an idealized case is considered. On the one hand, the mesh is supposed to be aligned with the axes and the horizontal faces are larger than the vertical ones. On the other hand, the vertical diffusivity is chosen smaller than the horizontal one so that $A_k||\underline{n}\cdot\underline{\kappa}||^2$ is constant. Ideally, the same penalty factor must be used on both kinds of face. For the horizontal faces, the minimum eigenvalue λ_m is introduced:

$$\mu_H = \frac{c_s}{2\lambda_m V_e} n_0 A_H \lambda_m^2$$

$$= \frac{c_s}{2V_e} n_0 A_H \lambda_m. \tag{2.18}$$

This expression reveals that this penalty factor will introduce less numerical diffusion since the ratio $\frac{\lambda_M^2}{\lambda_m}$ disappears. Thus, it will be well adapted to the anisotropic situations. Besides, for the vertical faces, the penalty factor is:

$$\mu_V = \frac{c_s}{2\lambda_m V_c} n_0 A_V \lambda_M^2,$$

which exactly corresponds to the penalty factor suggested by Rivière (see equation (2.10)). In this last case, the factor will still return excessive values, which will lead to too much numerical diffusion.

2.4.2 Oriented penalty factor

As the factor μ penalizes the jump of the concentration tracer C over the edge of an element, a natural approach to estimate the penalty factor for an

anisotropic diffusivity tensor is to consider its normal component on both sides of the interface of the elements Ern et al. (2008). In order to build such a penalizing term, the coordinate system is aligned with the principal axes of the diffusivity tensor and Ω is expressed in another reference frame Ω' . So that the coercivity criterion is satisfied, equation (2.12) is also used:

$$a(C,C) \geq \sum_{e} \int_{\Omega_{e}} \nabla C \cdot \underline{\underline{\kappa}} \cdot \nabla C \, d\Omega - \frac{1}{\epsilon_{Y}} \sum_{k} \int_{\gamma_{k}} \{\underline{n} \cdot \underline{\underline{\kappa}} \cdot \nabla C\}^{2} \, d\Gamma + \sum_{k} \int_{\gamma_{k}} (\mu - \epsilon_{Y}) [[C]]^{2} d\Gamma.$$

With the geometric law $2(m^+)^2 + 2(m^-)^2 \ge (m^+ + m^-)^2$, the integral in the second term of the right-hand side can be bounded as:

$$-\int_{\gamma_k} \{\underline{n} \cdot \underline{\underline{\kappa}} \cdot \nabla C\}^2 d\Gamma \geq -\int_{\gamma_k} \{(\underline{n} \cdot \underline{\underline{\kappa}} \cdot \nabla C)^2\} d\Gamma,$$

and the inequality becomes:

$$a(C,C) \geq \sum_{e} \int_{\Omega_{e}} \nabla C \cdot \underline{\kappa} \cdot \nabla C \, d\Omega - \frac{1}{\epsilon_{Y}} \sum_{k} \int_{\gamma_{k}} \left\{ \left(\underline{n} \cdot \underline{\kappa} \cdot \nabla C \right)^{2} \right\} \, d\Gamma + \sum_{k} \int_{\gamma_{k}} (\mu - \epsilon_{Y}) [[C]]^{2} d\Gamma.$$

$$(2.19)$$

Since the diffusivity tensor in the first term in the right-hand side is symmetric positive definite, it can be diagonalized:

$$\int_{\Omega_e} \nabla C \cdot \underline{\underline{\kappa}} \cdot \nabla C d\Omega = \int_{\Omega_e} \nabla C \cdot \underline{\underline{U}} \cdot \underline{\underline{\lambda}}^{1/2} \cdot \underline{\underline{\lambda}}^{1/2} \cdot \underline{\underline{U}} \cdot \nabla C \ d\Omega, \tag{2.20}$$

where the unit tensor $\underline{\underline{U}}$ describes the rotation that aligns the reference frame with the eigenvectors and $\underline{\underline{\lambda}}$ is the diagonal tensor scaled by the corresponding eigenvalues λ_i (i=1,2,3). The other terms of the equation can be transformed accordingly:

$$\begin{cases}
\nabla' C &= \nabla C \cdot \underline{U} \cdot \underline{\lambda}^{1/2}, \\
\underline{n}' &= \frac{\underline{\lambda}^{1/2} \cdot \underline{U} \cdot \underline{n}}{||\underline{\lambda}^{1/2} \cdot \underline{U} \cdot \underline{n}||}, \\
J' &= \sqrt{\lambda_1 \lambda_2 \lambda_3}.
\end{cases}$$

Note that the symbol ' indicates that the variable is expressed in the modified coordinate system. With this frame change, the equation (2.20) can thus be expressed as:

$$\int_{\Omega_e} \nabla C \cdot \underline{\underline{\kappa}} \cdot \nabla C \ d\Omega = J' \int_{\Omega'} \nabla' C \cdot \nabla' C \ d\Omega'.$$

Using the trace inequality (2.14) in the reference frame Ω' , this equation can be bounded as:

$$\sum_{e} \int_{\Omega_{e}} \nabla C \cdot \underline{\underline{\kappa}} \cdot \nabla C \ d\Omega \ge \sum_{k} \frac{J' \ V'_{e}}{c_{s} \ A'_{k}} \int_{\gamma'_{k}} (\nabla' C \cdot \underline{n}')^{2} \ d\Gamma', \tag{2.21}$$

where V'_e is the element volume and A'_k is the face surface in the reference frame Ω' . Some terms can be expressed in the initial coordinate system:

$$\begin{cases} V'_e J' = V_e, \\ \frac{1}{A_k} \int_{\gamma_k} \cdot d\Gamma = \frac{1}{A'_k S'} S' \int_{\gamma'_k} \cdot d\Gamma' & \text{with} \quad S' = \frac{d\Gamma}{d\Gamma'}, \end{cases}$$

so that the inequality (2.21) becomes:

$$\sum_{e} \int_{\Omega_{e}} \nabla C \cdot \underline{\underline{\kappa}} \cdot \nabla C \ d\Omega \ge \sum_{k} \frac{V_{e}}{c_{s} A_{k}} \int_{\gamma_{k}} (\nabla' C \cdot \underline{n}')^{2} \ d\Gamma.$$

Eventually, the squared term can be rotated in the usual reference frame \varOmega so that:

$$(\nabla' C \cdot \underline{n}')^{2} = \left(\nabla C \cdot \underline{\underline{U}} \cdot \underline{\underline{\lambda}}^{1/2} \cdot \frac{\underline{\underline{U}} \cdot \underline{\underline{\lambda}}^{1/2} \cdot \underline{n}}{||\underline{\underline{\lambda}}^{1/2} \cdot \underline{\underline{U}} \cdot \underline{n}||}\right)^{2}$$

$$= \frac{\left(\nabla C \cdot \underline{\underline{\kappa}} \cdot \underline{n}\right)^{2}}{||\underline{\underline{\lambda}}^{1/2} \cdot \underline{\underline{U}} \cdot \underline{n}||^{2}}$$

$$= \frac{\left(\nabla C \cdot \underline{\underline{\kappa}} \cdot \underline{n}\right)^{2}}{\left(\underline{n} \cdot \underline{\kappa} \cdot \underline{n}\right)}.$$

With this formulation, the bilinear form is bounded as follows:

$$\begin{split} a\left(C,C\right) & \geq \sum_{k} \int_{\gamma_{k}} \frac{2}{n_{0}c_{s}A_{k}} \bigg\{ V_{e} \frac{\left(\nabla C \cdot \underline{\kappa} \cdot \underline{n}\right)^{2}}{\left(\underline{n} \cdot \underline{\kappa} \cdot \underline{n}\right)^{2}} \bigg\} \, d\Gamma \\ & - \frac{1}{\epsilon_{Y}} \sum_{k} \int_{\gamma_{k}} \bigg\{ \left(\nabla C \cdot \underline{\kappa} \cdot \underline{n}\right)^{2} \bigg\} \, d\Gamma + \sum_{k} (\mu - \epsilon_{Y}) \int_{\gamma_{k}} [[C]]^{2} d\Gamma \\ & \geq \sum_{k} \int_{\gamma_{k}} \bigg\{ \left(\frac{2V_{e}}{n_{0}c_{s}A_{k}} \frac{1}{\left(\underline{n} \cdot \underline{\kappa} \cdot \underline{n}\right)} - \frac{1}{\epsilon_{Y}}\right) \left(\nabla C \cdot \underline{\kappa} \cdot \underline{n}\right)^{2} \bigg\} \, d\Gamma \\ & + \sum_{k} (\mu - \epsilon_{Y}) \int_{\gamma_{k}} [[C]]^{2} d\Gamma. \end{split}$$

In order to ensure the coercivity $a(C,C) > c_1 ||C||_S^2$, two conditions are required:

$$\begin{cases} \mu - \epsilon_Y = c_1 > 0, \\ \frac{2V_e}{n_0 c_s A_k} \frac{1}{\left(\underline{n} \cdot \underline{\kappa} \cdot \underline{n}\right)} - \frac{1}{\epsilon_Y} \ge 0. \end{cases}$$

These conditions are satisfied if μ is chosen such as:

$$\mu > \epsilon_Y > \frac{A_k c_s n_0}{2V_e} \ \underline{n} \cdot \underline{\underline{\kappa}} \cdot \underline{n},$$

and this corresponds to the oriented penalty factor. In the same way as for the eigenvalue factor, both kinds of face and then diffusion are studied. For the large horizontal surfaces of the element, and thus smaller diffusion, the penalty factor can be written as:

$$\mu_H = \frac{c_s n_0}{2} \frac{A_H}{V_e} \lambda_m,$$

which matches the eigenvalue factor for the same case (equation (2.18)). For the vertical faces, the oriented factor becomes:

$$\mu_V = \frac{c_s n_0}{2} \frac{A_V}{V_e} \lambda_M.$$

In this case, the ratio $\frac{\lambda_M^2}{\lambda_m}$ also disappears. The oriented penalty factor seems the most appropriate since it will introduce less numerical diffusion. It will now be compared numerically with the eigenvalue penalty factor.

2.4.3 Eigenvalue penalty factor vs oriented penalty factor

In this section, both penalty factors are compared in an oceanic simulation using SLIM and an unstructured mesh. The aim of this experimentation is on the one hand, to illustrate the effects of the penalty factors on the numerical solution and on the other hand, to intuitively understand their differences. A square mesh of 100km side is considered with 50 vertical layers on a total depth of 200m. To compare the simulations with an analytic solution (Spivakovskaya et al., 2007), the isopycnals are supposed to have uniform slopes and to be equally spaced. Hence, the diapycnal vector $\underline{\nu}$ is constant. Then, the isopycnal tensor is constant and an analytic solution of this boundary value problem can be found:

$$C^{h}(\underline{X},t) = \frac{\exp\left(-\frac{\underline{X} \cdot \underline{\underline{\kappa}}^{-1} \cdot \underline{X}}{4t}\right)}{(4\pi t)^{\frac{3}{2}} \sqrt{\det\left(\underline{\kappa}\right)}} \quad \forall t > 0,$$

where $A^I = 1000 \ [m^2/s]$ in the tensor $\underline{\underline{\kappa}}$ of equation (3.4). The analytic concentration field at $t = 1 \ day$ is used as initial condition $C(\underline{X}, 0)$ to replace the delta Dirac function since this function cannot be computed numerically. The tracer only undergoes isopycnal diffusion and a DIRK (Diagonally Implicit Runge-Kutta) semi implicit time integration is chosen (Ascher et al., 1997). With the

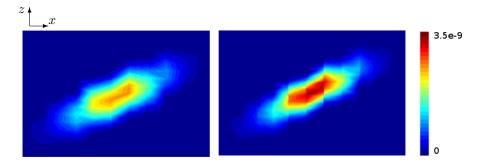


Figure 2.2: Vertical cross-section of a gaussian tracer field $C_r(\underline{X}, t = 20\Delta t)$ with a time step Δt of 1000 seconds when the eigenvalue (left-handside) and oriented (right-handside) penalty factors are used.

eigenvalue penalty factor, the result appears smoothed on the left-handside of the Figure 2.2, which is a vertical cross-section of the tracer field after $20\Delta t$ of 1000 seconds, and no strong jump is observed. But even with the new formulation of the penalty factor of Rivière $\mu \sim \sum_{k \in e} A_k ||\underline{n} \cdot \underline{\underline{\kappa}}||^2$, the eigenvalue

penalty factor is still too large and induces too much numerical diffusion. Indeed, with the anisotropy of both mesh and diffusivity, it varies in the range of $[2 \cdot 10^4, 10^{10}] \ m/s$. In the case of the oriented penalty factor, the value of the oriented penalty factor is much smaller than previously, i.e. in the range of $[2 \cdot 10^{-3}, 10^3] \ m/s$. Nevertheless, the numerical solution on the right-handside of the Figure 2.2 reveals large jumps. Even though the numerical solution obtained with the eigenvalue penalty factor looks smoother, the numerical error resulting from this approach is larger than the error made using the oriented penalty factor. Indeed, too much numerical diffusion in this scheme should be induced and that could distort the solution. When both figures are compared at the same time step, $C_o(\underline{X},t)$ has been less diffused since it has larger values than $C_r(\underline{X},t)$. In order to choose the better penalty factor, the \mathcal{L}_2 error, which is defined as $\|C^h - C\|_{\mathcal{L}_2}^2 = \int_{\Omega} (C^h(\underline{X},t_1) - C(\underline{X},t_1))^2 d\Omega$ where t_1 refers to the time evolution, is computed for each penalty factor. Figure 2.3 shows that the \mathcal{L}_2 error of the oriented penalty is lower than the error of the eigenvalue penalty factor. That means that the oriented factor, which stabilizes enough

the numerical scheme, does not induce too much diffusion, contrary to the eigenvalue penalty factor. This leads us to choose the oriented penalty factor and to pursue the numerical analysis with this one. In large-scale oceanic

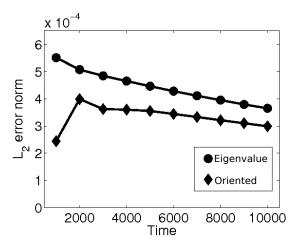


Figure 2.3: Study of the \mathcal{L}_2 error when the eigenvalue and oriented penalty factors are used.

models, the minimum-maximum principle is often violated (Cox, 1987; Harvey, 1995). Hence, the tracer concentrations can be negative, which leads to a local undershooting of this tracer. This situation produces unphysical water masses that can be transported and diffused in the world ocean. The monoticity could be discussed as in Mathieu and Deleersnijder (1998) where under/over-shoots are highlighted. But, as the diffusion is strongly anisotropic, only one property on the coercivity and the moniticity can be satisfied. Considering that the observed undershoots in the oceanic simulations are quite small, i.e. around $10^{-9}[K]$, the coercivity property is selected.

2.5 Comparison with the method of manufactured solutions

In order to know if the oriented penalty factor is well suited numerically, the spatial convergence is investigated. Specifically, the Method of Manufactured Solutions (MMS) allows to verify the code accuracy. A source term is added to the equation such that the analytic solution is known but non-trivial. Here, a simple anisotropic bidimensional diffusion equation is considered:

$$F(C) = \gamma \frac{\partial^2 C}{\partial x^2} + \alpha \frac{\partial^2 C}{\partial y^2} = 0, \qquad (2.22)$$

where the constant diffusion $\alpha=10^{-3}m^2/s$ and $\gamma=1m^2/s$ so that the anisotropy of the diffusion $\epsilon=1000$. First, an arbitrary manufactured solution is chosen as:

$$C_M(\underline{X}) = \frac{\exp\left(-\frac{\beta}{\tau} \left[\frac{x^2}{\gamma} + \frac{y^2}{\alpha}\right]\right)}{4\pi\tau\sqrt{\alpha\gamma}},$$

where the constant $\beta = 10^{-8}$ and the fictional time $\tau = 5$ seconds. Then, we add $F(C_M) = S$ as a source term of Eq. (2.22) and C_M as boundary condition:

$$F(C) = S$$
 $\underline{X} \in \Omega$,
 $C = C_M$ $\underline{X} \in \partial \Omega$.

By construction, the analytic solution of this problem is $C=C_M$. The error of the numerical solution is an indicator of the quality of the numerical method and allows to estimate the performance of the penalty factors. The domain geometry is a square of 100km side. Several meshes generated with the GMSH software (Geuzaine and Remacle, 2009; Lambrechts et al., 2008) are considered to study the spatial convergence. They are composed of quadrilateral elements with side lengths l_x and l_y linked by this relation: $l_y = \sqrt{\gamma/\alpha}l_x$, so that in the space $x'=x,y'=\sqrt{\gamma/\alpha}y$, the diffusivity tensor, the solution and the mesh are isotropic. Next, the domain is rotated in order to slightly misalign the elements and the main diffusion axes which stay along the coordinate axes. The rotation angle ω is taken as 0°, 0.5° and 1° since the oceanic density slope does not exceed 0.01.

In a first phase, the spatial convergence is computed with the norm of the \mathcal{L}_2 error defined as:

$$||C^h - C_M||_{\mathcal{L}_2}^2 = \int_{\Omega} (C^h(\underline{X}) - C_M(\underline{X}))^2 d\Omega.$$

The following penalty factors are studied:

• Rivière : $\mu_R = c_s \max \left(\frac{\sum_{k \in e} A_k}{2V_e} \right) \frac{\lambda_M^2}{\lambda_m}$,

• eigenvalue : $\mu_E = c_s \max \left(\frac{\sum_{k \in e} A_k ||\underline{n} \cdot \underline{\underline{\kappa}}||^2}{2V_e} \right) \frac{1}{\lambda_m}$,

• oriented : $\mu_O = c_s \frac{n_0 A_k}{2 \min(V_e)} \underline{n} \cdot \underline{\underline{\kappa}} \cdot \underline{n}$.

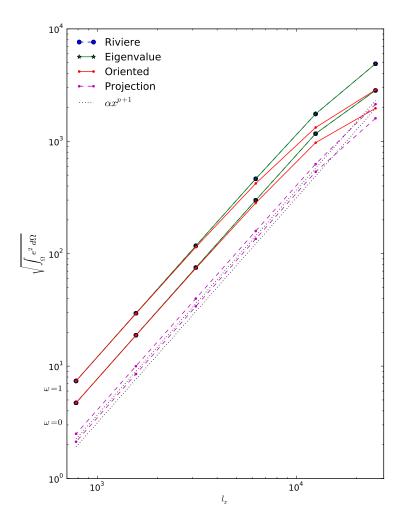


Figure 2.4: Comparison of the norms of the \mathcal{L}_2 error when the eigenvalue, oriented and Rivière penalty factors are used for the method of manufactured solutions at the order p=1 and for two rotation angles $\omega=0-1^\circ$. In both cases, the minimum norm of the \mathcal{L}_2 error shows that the oriented penalty factor is more appropriate, especially at coarse resolution.

and their spatial convergence is illustrated in Figure 2.4 for the order p=1 and the rotation angles $\omega=0^{\circ},1^{\circ}$. As expected, the \mathcal{L}_2 errors are smaller when there is no misalignement between the diffusion and the mesh. At coarse

resolutions, the oriented penalty factor has a smaller error than the other factors, whereas they converge in the same way at the finest resolutions. Besides, the lines for the Rivière and eigenvalue penalty factors cannot be distinguished.

In Figure 2.5, the spatial convergence is illustrated when there is no rotation angle and the orders 1 to 4 are considered. The lines for the Rivière and eigenvalue penalty factors still cannot be distinguished. At coarse resolution, the error when the oriented penalty factor is used is smaller for the odd orders, whereas it is comparable to the other penalty factor for the even orders. But at fine resolution, the error for the oriented penalty factor is lower. In all cases, there is no major difference in the errors obtained by the different penalty factors.

However, the main reason for this investigation was not the accuracy of the solution but the fact that the linear system arising from the Rivière approach is not able to solve the problem. Indeed, with the Rivière penalty factor, the system often crashed at the first time step. In reality, we expect to have a well-conditioned system when the penalty factor is small. For a linear system Ax=B, the condition number defined as $\eta=||A||\cdot||A^{-1}||$ allows to give a measure of the accuracy of the system. If the matrix is symmetric, $\eta=\frac{\sigma_M}{\sigma_m}$, where σ_m and σ_M are the minimum and maximum eigenvalues of the system matrix A, respectively. Indeed, the convergence of the iterative methods depends on the cluster of the eigenvalues of the system. The more η is closed to 1, the more the system is well-conditioned and thus easy and faster to solve. Moreover, the square-root of η gives the number of iterations required to solve the system.

The three penalty factors have been studied at the order p=1 and for the rotation angles $\omega=0^{\circ},0.5^{\circ},1^{\circ}$. Table 2.2 gives the eigenvalues of the system matrix and the condition number η for each case. When the Rivière penalty factor is used, σ_m cannot be found because the system cannot converge. In order to point out this state, the symbol \dagger has been used and σ_m has been replaced by the value computed with the oriented method since it does not vary with the method or the rotation angle. But it decreases with the resolution. Moreover, σ_M is independent of the mesh resolution, and for the Rivière and eigenvalue penalty factors, it is also independent of the rotation angles. For the oriented penalty factor, σ_M increases quadratically with the angle rotations.

For the orders 1 to 4 and the rotation angles $\omega=0^{\circ},1^{\circ}$, Table 2.3 gives the eigenvalues of the system matrix and the condition number η , when the oriented penalty factor is used. As previously, σ_M increases with the rotation angle, whereas σ_m remains the same. With the resolution, σ_M does not change

			$\omega = 0^{\circ}$,	$\omega = 0.5^{\circ}$			$\omega = 1^{\circ}$	
$l_x [m]$		0	臼		0	臼	R		臼	R
	σ_m	0.0041	0.0045		0.0041	0.0045	+		0.0045	
25000	σ_M	0.18	1500		0.19	1500	52000		1500	52000
	ι	44	3.4e5		46	3.4e5	1.3e7		3.4e5	1.3e7
	σ_m	0.0011	0.0012		0.0011	0.0012			0.0012	
12500	σ_M	0.19	1500		0.20	1500	52000		1500	52000
	и	170	1.3e6	4.7e7	180	1.3e6	4.7e7	200	1.3e6	4.7e7
	σ_m	0.00029		l	0.00029	-i			-i	-i
6250	σ_M	0.19	1500		0.19	1500	52000		1500	52000
	ι	650	5.2e6		089	5.2e6	1.7e8		5.2e6	1.7e8
	σ_m	7.4e-5			7.4e-5	- i			- - -	- i
3125	σ_M	0.19	1500		0.20	1500	52000		1500	52000
	μ	2600	2.0e7		2700	2.0e7	7.0e8		2.0e7	7.0e8
	σ_m	1.8e-5			1.8e-5		+-			
1562	σ_M	0.19	1500		0.20	1500	52000		1500	52000
	μ	1.0e4	8.3e7		1.1e4	8.3e7	2.9e9		8.3e7	2.9e9

Table 2.2: Study of the condition number η at the order 1 for each penalty factor (O: oriented, R: Rivière and E: eigenvalue penalty factor) and three rotation angles $(\omega=0^{\circ},0.5^{\circ},1^{\circ})$. The symbol † indicates when the value cannot be found because the system cannot converge. In this case, σ_m has been replaced by the value computed with the oriented method in order to compute η .

		p = 1		=d	= 2	p=3		= d	= 4
$l_x [m]$		$\omega = 0^{\circ}$	$\omega=1^{\circ}$	$\omega = 0^{\circ}$	$\omega = 1^{\circ}$	$\omega = 0^{\circ}$	$\omega = 1^{\circ}$	$\omega = 0^{\circ}$	$\omega=1$ °
	σ_m	0.0041	0.0041	0.0020	0.0019	0.0012	0.0011	0.00074	0.00074
25000	σ_M	0.19	0.22	0.24	0.30	0.61	0.72	1.5	1.7
	u	44	53	120 1	160	540	640	2000 20	2000
	σ_m	0.00029	0.00029	0.00013	0.00013	7.4e-5	7.4e-5	4.7e-5	4.7e-5
6250	σ_{M}	0.19	0.23	0.24	0.30	0.62	0.73	1.5	1.7
	μ	650	220	1800	2300	8400	0066	3.2e4	3.7e4

Table 2.3: Study of the condition number η for the order p=1,2,3,4 and the rotation angles $\omega=0^{\circ},1^{\circ}$ when the oriented penalty factor is used.

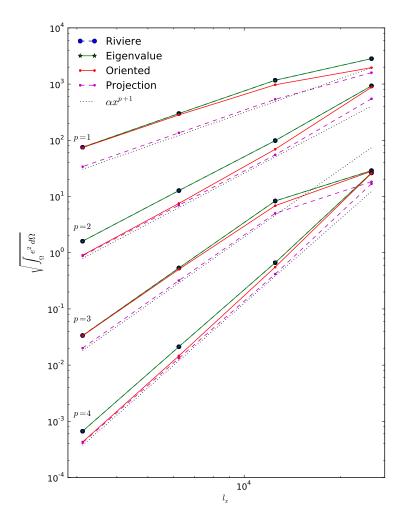


Figure 2.5: Comparison of the norms of the \mathcal{L}_2 error when the eigenvalue, oriented and Rivière penalty factors are used for the method of manufactured solutions without any rotation and for four orders (p=1,2,3,4). At the even orders, the oriented penalty factor converges faster.

but σ_m decreases. In regard to the order, σ_M increases with the order and σ_m decreases in such a way that η becomes larger. This is consistent since there are more nodes in an element but the stabilization remains the same. Actually, the same properties than previously can be observed for the other methods.

Besides, the following relations can be established for each method and for each order:

- $p = 1 : \sigma_M^R \approx 30\sigma_M^E \approx 30 * 250000\sigma_M^O$,
- $\bullet \ \ p=2:\, \sigma_M^R \approx 30 \sigma_M^E \approx 30*15000 \ \ \sigma_M^O,$
- p = 3: $\sigma_M^R \approx 30\sigma_M^E \approx 30*5000$ σ_M^O ,
- p = 4: $\sigma_M^R \approx 30\sigma_M^E \approx 30*5$ σ_M^O ,

where the superior index gives the method used. The relationship between the σ_M from the Rivière and eigenvalue methods remains the same regardless of the order but it becomes closer from σ_M computed with the oriented method when the order increases.

In the aim of a complete numerical analysis, larger rotation angles were taken into account in order to simulate larger anisotropies. In Figure 2.6, the spatial convergence at the order 1 is illustrated for the rotation angles $\omega=10^{\circ}-20^{\circ}$. For each case, the lines for the Rivière and eigenvalue penalty factors cannot be distinguished, as previously. Unlike the small rotation angles, the difference between the norms of the \mathcal{L}_2 error for he Rivière and eigenvalue penalty factors and for the oriented penalty factor is much larger when coarse meshes are used. Indeed, the three lines match further and further when the rotation angle increases. For the oriented penalty factor, the convergence order is reached quite fastly for $\omega=10^{\circ}$. For $\omega=20^{\circ}$, the asymptotic regime is also achieved but with finest meshes. For larger angles, the convergence will certainly be reached but the meshes need to be finer and the asymptotic regime is not really feasible for these cases. However, these large rotation angles require finest meshes which is not practicable for efficient simulations since such resolution take too much computational time.

To conclude, the oriented method has a better spatial convergence at coarse resolutions, which is the case for the oceanic meshes and is not worse than the other methods for the finest resolutions. But in terms of efficiency, it gives the better condition number whatever the order. The oriented penalty factor allows to have a well-conditioned system that can be solved rapidly. Its eigenvalues for the system matrix can always be found for all the orders, which is not the case with the Rivière and the eigenvalue methods. The oriented penalty factor is thus the most appropriate to solve problems with strong anisotropic diffusion.

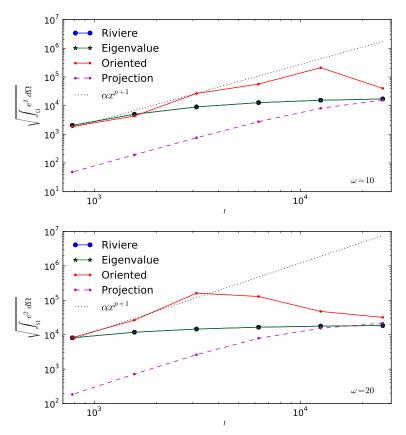


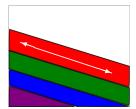
Figure 2.6: Comparison of the norms of the \mathcal{L}_2 error when the eigenvalue, the oriented and the Rivière penalty factors are used for the method of manufactured solutions at the order 1 and for larger rotation angles: $\omega = 10^{\circ}$ (top) and $\omega = 20^{\circ}$ (bottom).

2.6 Physical application

To complete this study, a more realistic simulation is achieved on an idealized Arctic Ocean. This area is well adapted to investigate the strongly anisotropic diffusion since the density field undergoes high variations. Even if this diffusion is non-constant in the time and in the space and thus that, no convergence study will be possible, this application allows to highlight the importance, on the one hand, of a well-conditioned system and on the other hand, of less numerical diffusion that could distort the solutions. The isopycnal diffusion mixed the tracers along the isopycnals due to the presence of the mesoscale eddies. Mesoscale eddies, which have length scale from 75 to 200 km, are found almost

everywhere in the ocean. Their kinetic energy is much larger than that of the time-average circulation. They are formed as a result of instabilities and are highly influenced by the rotation of the Earth; they stir and mix the salt and other tracers, transport quantities and influence the density field and the general ocean circulation (Rhines, 2009).

Iselin (1939) and Montgomery (1940) suggested that the mixing of tracers by mesoscale eddies in the stratified ocean mainly occurs along the surfaces of constant density, i.e., the isopycnals. It appears that some smaller processes also mixed the tracers but orthogonally to the isopycnals, so that these surfaces are called diapycnals. Even with its small magnitude, the diapycnal diffusion should also be taken into account in the parameterization of the mesoscale eddies. This situation creates a strong anisotropy in the diffusion tensor. In order to model the effects of this anisotropic turbulence and transport along and accross isopycnals, Redi (1982) considered a new isopycnal mixing tensor where the main axis of diffusivity have been rotated from the standard cartesian coordinates towards any direction where there is a density gradient. The isopycnal diffusivity operator is then built as a non-linear function of the active tracer concentrations since the diffusion operator depends on the density which, in turn, is a function of salinity and temperature (Gent and McWilliams, 1990). McDougall (1987) emphasizes that the neutral directions are relevant for the diffusive fluxes of the tracers (Figure 2.7). Gent and McWilliams (1990) sug-



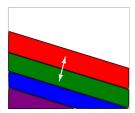


Figure 2.7: Both pictures represent a vertical cross-section of a density field where each color is associated to one density value. The isopycnal direction corresponds to the direction of isopycnals. Hence, an isopycnal diffusivity occurs along the surfaces of constant density (left), whereas the diapycnal one takes place orthogonally to these surfaces (right).

gested that the effects of mesoscale eddies can be taken into account by means of a special closure in ocean models. These eddies are likely generated by baroclinic instability of the mean flow, getting their energy from the enormous potential energy reservoir linked to horizontal density contrasts (Gill et al., 1974). The available potential energy is then reduced by the parameterization, as if it was transformed into kinetic energy. But, eddy kinetic energy is not resolved by models that need this closure. This extra non-divergential velocity,

called the *Gent-McWilliams velocity*, yields some improvements in climate simulations since it relaxes the density slopes and thus releases potential energy (Griffies, 1998).

To observe the effects of the Gent-McWilliams velocity and isopycnal diffusion on a closed domain, a cylindrical geometry modelling the upper central Arctic Ocean, with a 200m depth and a radius of 10° of latitude, is meshed with 30 layers of prismatic elements whose horizontal characteristic length is about 10^{5} m. The temperature and salinity are initialized on this mesh using the PHC data (Polar science center Hydrographic Climatology Steele et al. (2001a)). In order to remove the effects of compressibility of the ocean water, the considered parcel of water is raised adiabatically from its depth to the sea surface (p=0) before computing the density, which in this case is called potential density. The latter is obtained from the Jackett and McDougall (McDougall et al., 2006) equation of state:

$$\rho(S, \vartheta, p) = \frac{P_1(S, \vartheta, p)}{P_2(S, \vartheta, p)},$$

where ϑ is the potential temperature and P_1, P_2 are both polynomial functions of 12 and 13 terms, respectively. Since the potential density field is used in a realistic application, some static instabilities can appear during the simulation. Hence, when a parcel of water with a potential density ρ_1 is below another parcel of potential density ρ_2 such that $\rho_1 < \rho_2$, the column of water is unstable. In nature, convective processes quickly re-establish the static stability of the column. Since these processes are not included into the ocean model because of the hydrostratic assumption, a convective adjustment scheme is added to counteract these undesirable effects (Marotzke, 1991). Various techniques can be used such as a non-penetrative convective adjustment, a turbulent closure scheme or an enhanced vertical diffusion. In this work, the latter is used in the tracer equation. It consists in enlarging the vertical diffusivity coefficient to 1 $[m^2/s]$ when the stratification is unstable, i.e., when the Brunt-Vaïsälä frequency N_b^2 is negative (Madec and team, 2008).

The tracer equation with both advection and diffusion terms is now considered:

$$\frac{\partial C}{\partial t} + \nabla \cdot (\underline{u}_{ed} \ C) = \frac{\partial}{\partial z} \left(\nu_v \frac{\partial C}{\partial z} \right) + \nabla \cdot \left(\underline{\underline{\kappa}}^s \cdot \nabla C \right),$$

where \underline{u}_{ed} is the Gent-McWilliams velocity, ν_v the scalar vertical diffusion coefficient that can be enhanced by the convective adjustment and $\underline{\kappa}^s$ the isopycnal diffusivity tensor. The vertical diffusivity decreases with depth from $10^{-3}m^2/s$ to $10^{-5}m^2/s$ over the upper 200m. In Figure 2.8, the initial states are in the left column, while the states after 520 days are in the right column. Note

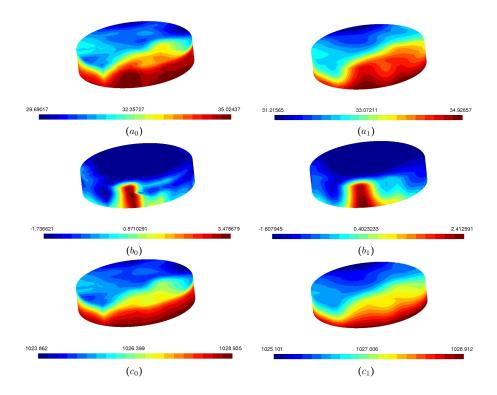


Figure 2.8: (a_0) Initial condition of the tracer S [psu]; (b_0) initial condition of the tracer T [${}^{\circ}C$]; (c_0) potential density computed with the equation of state $\rho = \rho(S, T, p)$ [kg/m^3]; (a_1) tracer S after 520 days [psu]; (b_1) tracer T after 520 days [${}^{\circ}C$]; (c_1) potential density after 520 days [kg/m^3].

that the range of each tracer at the initial time differs from the range at the final time. As the density field is created from temperature and salinity, it is influenced by them during the tracers evolution. But, as the domain is situated in the Arctic, and thus in a cold area, the density is more influenced by salinity than by temperature. Both temperature and salinity are diffused in order to align themselves along the isopycnals. But as the temperature has an initial field much more different than the salinity, it evolves faster. Indeed, the relative difference between the initial and the final maximum values is around $1.06[c^{\circ}]$ for temperature, whereas it is around 0.09[psu] for salinity. As expected, each tracer tends toward its mean value in the time. In fact, their minimum and maximum values increase and decrease respectively, which means that the minimum-maximum principle is kept.

The Gent-McWilliams velocity obtained at the end of the simulation is shown in Figure 2.9. Even if its maximum value is quite small, this velocity really has an impact on the global oceanic circulation but in the long run. As expected, the velocity field never crosses the boundaries of the domain

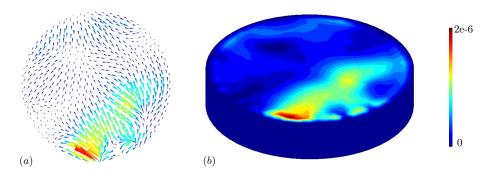


Figure 2.9: Gent-McWilliams velocity [m/s] after 520 days at the surface (a) and its norm on the whole domain (b).

(Fig.2.9.(a)) since it is a divergence-free velocity. A small closed circulation is thus created and can be easily observed. On the front of the middle of the domain in Figure 2.9.(b), the velocity is larger than in other places. This situation points out that the spatial variation of the density is strong at this place (see Figure 2.8). Furthermore, this velocity tends to reduce the slope of the density field (Fig.2.8.(c1)) where the isopycnals have been flattened and smoothened. Finally, all these features show that both isopycnal diffusion and Gent-McWilliams velocity significantly influence the large-scale transport of the oceanic tracers, as discussed by Cox (1987); Gent and McWilliams (1990); Gent et al. (1995). We conclude thus that the discretization of this strong anisotropy isopycnal diffusion with DGFEM is ready for further more complex simulations within the framework of SLIM.

2.7 Concluding remarks

In this chapter, the discretization of a diffusion equation with a strong anisotropy by a discontinuous Galerkin finite element method is investigated. The standard discontinuous Galerkin discretization required a special attention to the penalty factor in order to deal correctly with the jumps between the elements and ensure the numerical stability.

Two penalty factors have been proposed and compared. On the one hand, the penalty factor suggested by Rivière is a function of the anisotropy factor and can sometimes be very large. In this case, the numerical solution is too much diffused and thus more approximate. This penalty factor was then improved and renamed eigenvalue penalty factor. On the other hand, in order to take into account the diffusion in the direction normal to the interface between the elements, the oriented penalty factor is defined by rotating the system to align it with the principal axes of the diffusivity tensor. When strong anisotropy exists in the diffusivity tensor, we suggest a particular value.

The comparison between both factors shows that the oriented factor provides less numerical diffusion than the eigenvalue factor and still stabilizes enough the numerical scheme. Moreover, the method of manufactured solutions revealed that the oriented penalty factor has a better spatial convergence at coarse resolutions, which is the case for the oceanic meshes. But, in terms of efficiency, it gives the best condition number whatever the order, and thus allows to have a well-conditioned system that can be solved rapidly. Finally, this factor is used in a physical application (an idealized Arctic Ocean) where the density field can undergo large variations. Hence, the main features of the isopycnal diffusion as well as that of the Gent-McWilliams velocity are observed: the tracers tend to follow the isopycnals and the slopes of the density field are progressively reduced.

To the best of our knowledge, it is the first time that a strong anisotropic diffusion is discretized with the DGFEM. The numerical simulations carried out show that the choice of the oriented penalty factor is well-adapted to this anisotropy and the conclusions from the physical application goes on the same track. Next work will be devoted to the inclusion of the isopycnal diffusion in the complete three-dimensional oceanic model SLIM where all the governing equations are considered. In this study, the impacts of the mesoscale eddies will be analyzed on the long run. Such a study will allow a better understanding of these complex and still not well-known processes.

CHAPTER SHAPTER

Gent-McWilliams velocity and isopycnal diffusion

This Chapter is based on the following paper, submitted on 23 March 2015: A. Pestiaux, S.A. Melchior, P. Delandmeter, T. Fichefet and E. Deleersnijder. Gent-McWilliams velocity and isopycnal diffusion in a discontinuous Galerkin finite element ocean model. $Ocean\ Dyn.$

Abstract

Isopycnal diffusion has formerly been investigated in a discontinuous Galerkin finite element ocean model through idealized numerical experiments. Here, the Gent-McWilliams velocity and the isopycnal diffusion are evaluated within the framework of a proper ocean model study. Due to the discontinuous discretization, special care is required to deal correctly with the penalty terms and their physical developments. The mass fluxes due to unresolved processes are represented by means of a diffusivity tensor. The Gent-McWilliams velocity computed from the antisymmetric part of this tensor is included in the advective term of the tracer equation. In order to ensure a vanishing transport on all the domain boundaries, a one-dimensional boundary-value problem

is taken and is seen to be well suited to our model thanks to the application to an idealized channel. On the other hand, the symmetric part of the diffusivity tensor, which represents the diapycnal and isopycnal diffusions, has a strong anisotropy that is due to the discrepancy between the order of magnitude of the associated diffusivities and the related length scales. To stabilize the dgFEM numerical scheme, the oriented penalty term investigated in the previous study is selected. To highlight this methodology in the framework of the ocean model, the evolution of a tracer concentration distribution initialized as a Gaussian is studied in a inclining density field. Next, the spurious flux in the diapycnal direction appears to be negligible as compared with the existing diapycnal diffusivity.

3.1 Introduction

Mesoscale oceanic eddies, which have a length scale ranging from 10 to 200 km, have a kinetic energy which is much larger than that of the general circulation. The transfer of energy to the mesoscale eddies from the general circulation is largely a consequence of barotropic and baroclinic instabilities, which take place in most of the World Ocean. They are highly influenced by the rotation of the Earth. They stir and mix salinity and temperature as well as other tracers and, by doing so, influence the density field. They play a role in the general ocean circulation by transporting mass, heat and momentum (Rhines, 2009).

Due to insufficient spatial resolution, the above mentioned eddies cannot be resolved explicitly in oceanic general circulation models used in climate studies. Therefore, parameterizing their effects is necessary even though this can be computationally expensive. Indeed, parameterizing mesoscale processes significantly improves the accuracy of simulations, e.g., the global temperature and salinity distributions, the heat fluxes and the locations of deep water formation (Danabasoglu et al., 1994; Danabasoglu and McWilliams, 1995).

Over half a century ago, Iselin (1939) and Montgomery (1940) suggested that the mixing of tracers by mesoscale eddies in the stratified ocean occurs along isopycnals, i.e. surfaces of constant density. In order to model the effects of this anisotropic turbulence and transport along and accross isopycnals, Redi (1982) considered a new isopycnal mixing tensor where the main axis of diffusivity have been rotated from the standard cartesian coordinates towards any direction where there is a density gradient. The isopycnal diffusivity operator is then built as a non-linear function of the active tracer concentrations since the diffusion operator depends on the density which, in turn, is a function of salinity and temperature (Gent and McWilliams, 1990). In addition to isopycnal diffusion, physical diapycnal diffusion occurs in the direction orthogonal to

the isopycnals, and since the isopycnals are gently sloping, this situation leads to anisotropy because of the much weaker magnitude of the diapycnal diffusion. The isopycnal-diapycnal diffusion operator, initially used by Redi, differs thus fundamentally from isotropic and homogeneous diffusion since the associated diffusivity tensor is neither diagonal nor constant. McDougall (1987) emphasizes that the isoneutral directions, i.e. along the surfaces of constant potential density σ_r at a particular depth r, are crucial for the diffusive fluxes of the tracers.

Gent and McWilliams (1990) suggested that the effects of mesoscale eddies can be taken into account by means of a special closure in ocean models. These eddies are likely generated by baroclinic instability of the mean flow, getting their energy from the enormous potential energy reservoir linked to horizontal density contrasts (Gill et al., 1974). The available potential energy is then reduced by the parameterization, as if it was transformed into kinetic energy. But, eddy kinetic energy is not resolved by models that need this closure. This extra velocity leads to some improvements in the climate simulations since it relaxes the density slopes and thus releases potential energy Griffies (1998).

The aim of this study is to include the Gent-McWilliams velocity and isopycnal diffusion in the Second-generation Louvain-la-Neuve Ice-ocean Model (SLIM², White et al., 2008a; Blaise et al., 2010; Kärnä et al., 2012), which is a discontinuous Galerkin (DG) finite element ocean model. The finite element method presents some advantages: it is highly parallelizable and allows for local refinement using adaptive meshes; the complex geometries and boundary conditions are treated in a simpler manner, so that the coastlines or particular areas of interest are preserved. Even if the mesh is unstructured in the horizontal direction with several layers of triangular prisms, it is also structured along the vertical and this property allows to preserve the natural stratification of the ocean. This difference between both directions is well adapted to the oceanic circulation. In addition, the Discontinuous Galerkin Finite Element Method (DGFEM) theoretically enables arbitrarily high order-of-accuracy solutions, which are represented in each element independently of the solutions in other cells, with inter-elements communications only through the interfaces of adjacent cells. This feature permits the formulation of very compact numerical schemes. A large number of favorable numerical properties make this method extremely flexible in terms of element variety or adaptive techniques. Moreover, DGFEM is better adapted for the advection than the Continuous Galerkin (CG) finite element method, since the numerical fluxes and the slope limiters can be incorporated easily. The approximate solution also contains

¹The potential density is the density that a parcel of water would have if it were raised adiabatically to the surface without change in salinity.

 $^{^{2}}http//www.climate.be/slim/$

less numerical dissipation for an equivalent mesh and an optimal dispersion (Ainsworth, 2004). As a large-scale oceanic model, SLIM requires a mesoscale eddy parameterization in order to capture the effects of eddies on the resolved flow, while special attention must be drawn to its DGFEM discretization since interior penalty terms are introduced to yield a compact scheme. Especially, the estimation of the penalty factor is required to stabilize the finite element method (Oden and Kim, 1982). In Wang et al. (2008), the Gent-McWilliams velocity and isopycnal diffusion terms are already discretized with the CG method, where their implementation is straightforward since there is no penalty term. Indeed, the treatment of the penalty terms in DG remains one of the main difficulties in the improvement of physical processes. In the present work, the Gent-McWilliams velocity and isopycnal diffusion terms are discretized with DGFEM in the framework of SLIM. In the first study (Pestiaux et al., 2014), the strong anisotropic diffusivity tensor associated to the isopycnal diffusion was investigated and validated with some numerical test cases. In this work, emphasis is put on the oceanic analyses of the isopycnal diffusion and the Gent-McWilliams velocity. On the one hand, conservation and consistency properties are seen to be satisfied for both terms. On the other hand, they are validated with a realistic oceanic application after the study of the spurious mixing related to isopycnal diffusion discretization.

The paper is organized as follows. The Gent-McWilliams velocity and the isopycnal diffusion are introduced in Section 2. Their discontinuous finite element discretization is described in Section 3. Section 4 investigates the vanishing of the isoneutral flux when the equation of state is linear. Some analytical and numerical results are presented. Finally, concluding remarks close the paper in Section 5.

3.2 Equations of the tracer model

The impact of mesoscale eddies is usually parameterized in the equations governing the evolution of the scalar quantities, which, for the sake of simplicity, will be often referred to as tracers hereinafter. As a tracer is any fluid property used to track flow, there are three general types of ocean tracers: the tracers representing the concentration of material constituents such as salinity or passive tracers, the tracers representing the thermodynamic properties such as temperature, and the tracers embodying dynamical properties such as potential vorticity³. In SLIM, each tracer concentration field $C(\underline{x},t)$, typically the temperature T or the salinity S, satisfies the following advection-diffusion

³The potential vorticity is a quantity which is proportional to the dot product of vorticity and stratification that, following a parcel of water, can only be changed by diabatic or frictional processes.

equation:

$$\frac{\partial C}{\partial t} + \nabla \cdot (\underline{u} \ C) = \nabla \cdot (\underline{\underline{\kappa}} \cdot \nabla C), \tag{3.1}$$

where \underline{u} is the velocity resolved by the model and the tensor $\underline{\kappa}$ parameterizes two effects: stirring and mixing, associated to its antisymmetric and symmetric parts, respectively: $\underline{\underline{\kappa}} = \underline{\underline{\kappa}}^S + \underline{\underline{\kappa}}^A$. The choice to split $\underline{\underline{\kappa}}$ makes sense due to the special treatment of the strong anisotropy relative to symmetric part in the framework of the dgFEM. Even if each part represents different physical processes, both are computed from the density ρ , which is itself a function of T and S through the equation of state. The symmetric part, which matches up to diffusivity, mixes the tracer concentration along the isopycnal and diapycnal directions, whereas the antisymmetric part stirs the tracer concentration without mixing and flattens the isopycnals. Since the antisymmetric tensor $\underline{\kappa}^A$ has nul eigenvalues, it cannot be treated alone and as it is because it could lead to an ill-conditioned system. Both parts are detailed in the following sections. Initial conditions C(x,0) are supposed to be given and no normal flux of both temperature and salinity is allowed on the boundary $\partial\Omega$ of the domain $\Omega \subset \Re^d$, where d=3 implying that $\underline{x}=(x,y,z)$. In this vector, x and y are the horizontal coordinates whereas the vertical one z increases upwards. The unit normal \underline{n} is defined everywhere on the boundary.

3.2.1 Gent-McWilliams velocity

In this section, the antisymmetric part of the mesoscale tensor $\underline{\underline{\kappa}}$ is seen to be associated with an additional advective term. This transformation is based on the following assumption: the advection of the density field by the extra velocity leads to the reduction of the density slope⁴ \tilde{s} which is obtained from the density ρ as:

$$\widetilde{s} = [s_x, s_y] = -\frac{\nabla_h \rho}{\partial \rho / \partial z},$$
(3.2)

and to the reduction of the available potential energy. Griffies et al. (1998) considered the skew flux which is defined to be perpendicular to the tracer gradient, i.e., $\underline{F}_s = -\underline{\psi} \times \nabla C$, where $\underline{\psi}$ is the streamfunction vector. They proposed to decompose \underline{F}_s into two parts:

$$\underline{F}_s = (\nabla \times \underline{\psi}) \ C - \nabla \times (C \ \underline{\psi}) \ .$$

Since the divergence of a curl is always zero, the divergences of the advective flux $(\nabla \times \psi)$ C and of the skew flux are identical. Hence, the latter is simply the

 $^{^4}$ The tilde refers to a two-dimensional vector, whereas the underline refers to a three-dimensional vector.

product of the tracer concentration with the additional divergence-free Gent-McWilliams velocity $\underline{u}_{GM} = \nabla \times \underline{\psi}$ (Gent and McWilliams, 1990). In Gent et al. (1995), the streamfunction is computed as $\underline{\psi} = -A^I \ [s_x, s_y, 0] \times \underline{\hat{e}_z}$, where A^I is the isopycnal diffusivity parameter. As a result, we get:

$$\underline{u}_{GM} = \left[-\frac{\partial}{\partial z} \left(A^I s_x \right), -\frac{\partial}{\partial z} \left(A^I s_y \right), \frac{\partial}{\partial x} \left(A^I s_x \right) + \frac{\partial}{\partial y} \left(A^I s_y \right) \right].$$

The interchangeability of the algebraic properties of the cross product implies that:

$$\nabla \cdot \left((\nabla \times \underline{\psi}) \ C \right) = -\nabla \cdot \left(\underline{\psi} \times \nabla C \right) = -\nabla \cdot (\underline{\underline{\kappa}}^A \cdot \nabla C),$$

where the antisymmetric tensor $\underline{\kappa}^A$ in the (x, y, z) reference frame is:

$$\underline{\underline{\kappa}}^A = A^I \begin{pmatrix} 0 & 0 & -s_x \\ 0 & 0 & -s_y \\ s_x & s_y & 0 \end{pmatrix}$$

Hence, equation (3.1) can be re-written as follows:

$$\frac{\partial C}{\partial t} + \nabla \cdot \left[(\underline{u} + \underline{u}_{GM})C \right] = \nabla \cdot \left(\underline{\underline{\kappa}}^S \cdot \nabla C \right).$$

3.2.2 The issue of boundary conditions

A recurrent problem in the parameterization of the effects of mesoscale eddies is to impose correct boundary conditions. The normal component of the parameterized eddy-induced Gent-McWilliams flux must vanish on all boundaries (Griffies et al., 1998) because the flux cannot cross the domain boundaries. Instead of using the slope (3.2), Ferrari et al. (2010) suggested to approximate the streamfunction by \widetilde{Y} , which can be obtained from the following partial differential equation:

$$\left(c^2 \frac{\partial^2}{\partial z^2} - N_b^2\right) \widetilde{Y} = \frac{g}{\rho_0} \nabla_h \rho$$

$$\widetilde{Y}(\eta) = \widetilde{Y}(-H) = [0, 0],$$
(3.3)

where $N_b = \sqrt{-\frac{g}{\rho_0} \frac{\partial \rho}{\partial z}}$ is the Brunt-Väisälä frequency, c a depth independent speed, H is the ocean depth, ρ_0 the constant reference density, g the gravitational acceleration and η the ocean surface elevation. Let us notice that when the derivative of the streamfunction is nul in this problem, the traditional parameterization for Ψ is recovered instead of \widetilde{Y} . A detailed analysis from Ferrari et al. (2010) shows that the most accurate value for this speed is the first baroclinic phase speed $c = \frac{N_b H}{\pi}$ for the Eady problem (Eady, 1949). In the latter,

the baroclinic instability is analyzed in a flow on a f-plane with uniform zonal shear between upper and lower bounding surfaces, using the Boussinesq approximation to the full fluid equations. With this partial derivative equation, correct behaviors of the eddies seem to be captured (Ferrari et al., 2010). The approximation $[\widetilde{Y},0]$ is then close to $\underline{\psi}=-A^I[\widetilde{s},0]\times\underline{\widehat{e}}_z$ except near the surface and the bottom since the transport vanishes by construction. With this method, an approximation of the Gent-McWilliams velocity is found to be:

$$\underline{u}_{GM} \approx \underline{u}_{ed} = [\partial_z Y_x, \partial_z Y_y, -\partial_x Y_x - \partial_y Y_y].$$

Note that this allows avoiding to use additional tapering functions (e.g., Griffies (2004)), which are introduced when the density slope is too strong in order to reduce it. None strong modification is then directly applied on the density field. Even small modifications in the choice of their value imply changes in the overall ocean circulation (Gnanadesikan et al., 2007). Since no additional tapering function is required, the present scheme enables us to remain the closest to the theoretical description of this parameterization.

3.2.3 Isopycnal diffusion

Concerning the symmetric part of the mesoscale tensor, let us define $\underline{\nu} = -\nabla \rho$ and create the diapycnal unit vector:

$$\widehat{\underline{\nu}} = \frac{\underline{\nu}}{\|\underline{\nu}\|} = \frac{[s_x, s_y, -1]}{\sqrt{s_x^2 + s_y^2 + 1}}.$$

The $\underline{\widehat{\nu}}$ vector is important since the flux associated with the anisotropic diffusion in the ocean is oriented along and across the density slope. The symmetric diffusivity tensor $\underline{\kappa}^S$, which is made up of isopycnal and diapycnal parts, can then be expressed as:

$$\underline{\underline{\kappa}}^{S} = A^{I}(\underline{\underline{\delta}} - \underline{\widehat{\nu}} \ \underline{\widehat{\nu}}) + A^{D} \ \underline{\widehat{\nu}} \ \underline{\widehat{\nu}},$$

where $\underline{\underline{\delta}}$ is the Kronecker delta and A^I and A^D are the positive isopycnal and diapycnal diffusivities, respectively. Using the local density slope \widetilde{s} , Redi (1982) showed that the tensor $\underline{\kappa}^S$ in the (x,y,z) reference frame is:

$$\underline{\underline{\kappa}}^{S} = \frac{A^{I}}{1 + \|\widetilde{s}\|^{2}} \begin{pmatrix} 1 + s_{y}^{2} + \epsilon s_{x}^{2} & (\epsilon - 1)s_{x}s_{y} & (1 - \epsilon)s_{x} \\ (\epsilon - 1)s_{x}s_{y} & 1 + s_{x}^{2} + \epsilon s_{y}^{2} & (1 - \epsilon)s_{y} \\ (1 - \epsilon)s_{x} & (1 - \epsilon)s_{y} & \epsilon + \|\widetilde{s}\|^{2} \end{pmatrix}, \tag{3.4}$$

where $\epsilon = \frac{A^D}{A^I}$ is the ratio of the diapycnal diffusivity to the isopycnal diffusivity. Moreover, ϵ is supposed to be small since it is a measure of the relatively

weak vertical cross-isopy cnal mixing. In this study, $\epsilon = \frac{10^{-4}}{1000} = 10^{-7}$ is used. Cox (1987) suggested the following approximation:

$$\underline{\underline{\kappa}}^S = A^I \begin{pmatrix} 1 & 0 & s_x \\ 0 & 1 & s_y \\ s_x & s_y & \epsilon + \|\widetilde{s}\|^2 \end{pmatrix},$$

where high order terms for small values of the slope \tilde{s} and ϵ are neglected. Note that Cox originally kept the (1,2) and (2,1) terms in the tensor. They are equal to $-s_x s_y$ but it appears that these terms induce diffusion that could modify the buoyancy field, whereas the full neutral diffusivity tensor does not affect the buoyancy field (Griffies, 2004). Indeed, it does not diffuse locally referenced potential field, but preserving the neutral directions while diffusing the active tracers is not obvious and not always feasible. This characteristic, investigated in section 3.4, means that if the density is used as tracer concentration C in the tracer equation (3.1), the isopycnal diffusion should not modify the density at all.

3.3 Discontinuous finite element discretization

A discontinuous finite element method is applied to solve the tracer equation. Finite element methods involve a double discretization. First, the domain Ω is discretized into a collection of elements:

$$\Omega \approx \Omega^h = \bigcup_e \Omega_e \ , \ \partial \Omega \approx \bigcup_k \partial \Omega_k,$$

which constitute a mesh. This first step is referred to as the *geometrical discretization*. In our case, the mesh has a specific structure. A two-dimensional mesh of the surface of the ocean is created and subsequently extruded in the vertical direction (Figure 3.1).

Then, the continuous function space where the unknown field C is defined is replaced by a finite dimensional subspace. On each element Ω_e , the solution is approximated by a polynomial expansion:

$$C(\underline{x},t) \approx C^h(\underline{x},t) = \sum_{j=1}^{N} C_j^e(t) \ \tau_j(\underline{x}), \quad \underline{x} \in \Omega_e, \quad \forall e,$$

where N is the number of nodes in an element, τ_j is the shape function relative to node j and $C_j^e(t)$ is the degree of freedom relative to node j of element Ω_e . The specificity of DGFEM is that the solution is approximated in each element

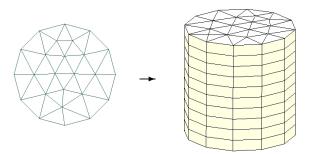


Figure 3.1: Triangulation of non-overlapping elements at the surface of the domain (left) and vertical extrusion in order to create prismatic elements (right).

separately: no a priori continuity requirements are needed. The discrete solution may then be discontinuous at inter-element boundaries. In this paper, elements Ω_e are prisms with vertical faces (Wang et al., 2008) and P_1^{DG} shape functions, i.e. polynomials of degree 1, are chosen in each element (implying that N=6).

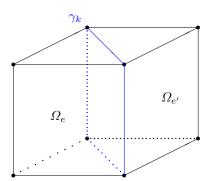


Figure 3.2: Notation used to describe the mesh topology: any interior face γ_k is common to adjacent prisms Ω_e and $\Omega_{e'}$.

Discontinuous Galerkin methods require to compute consistent numerical fluxes at element interfaces in order to satisfy numerical stability conditions. For that, we use the following notation: $\gamma_k = \Omega_e \cap \Omega_{e'}$ (Figure 3.2) for the inter-element interfaces. The set of all element interfaces is noted $\Gamma = \bigcup_k \gamma_k$.

To build a polynomial interpolation on these elements which have the same topology but different geometries, an isomorphism is established with a reference element $\widehat{\Omega}$ (Figure 3.3).

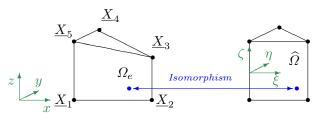


Figure 3.3: Isomorphism between the actual geometry (left) and the reference element (right).

In each element Ω_e , a mapping $\underline{X}(\underline{\chi})$ provides the real coordinates in terms of the reference coordinates $\underline{\chi}=(\xi,\eta,\zeta)\in\widehat{\Omega}$. All the computations are performed in the reference element. At each integration point, the shape function, the gradients of the shape function and the Jacobian⁵ are computed. Finally, a discrete Galerkin formulation is defined to obtain the values of $C_j(t)$, such as the DGFEM formulation described below. To reduce the degree of differentiability required by the shape functions, an integration by parts is usually performed.

The advective part of the tracer equation will be considered separately from the diffusive part since they are treated with different numerical schemes.

3.3.1 DGFEM formulation of the advective part

The evolution of the tracer concentration with only the Gent-McWilliams velocity obeys the equation:

$$\frac{\partial C}{\partial t} + \nabla \cdot (\underline{u}_{ed} \ C) = 0.$$

The associated weak formulation can be written as follows:

$$\int_{\varOmega} \frac{\partial C}{\partial t} \tau_{j} d\Omega + \int_{\varOmega} \nabla \cdot (\underline{u}_{ed} \ C) \tau_{j} d\Omega = 0 \ \forall \tau_{j}, \tag{3.5}$$

where τ_j is the test function. In moving from the domain (Ω) to the elements of the mesh $(\Omega_e, \partial \Omega_e)$, the test functions are chosen to be similar to the shape

 $^{^5{}m The}$ determinant of the Jacobian matrix which is the matrix of all first-order partial derivatives of a vector-valued function, is called the Jacobian.

functions τ_i . The divergence theorem and integration by parts lead to⁶:

$$\int_{\Omega_e} \frac{\partial C}{\partial t} \tau_j d\Omega + \sum_k \int_{\gamma_k} \underline{n} \cdot \{\underline{u}_{ed}\} C \tau_j d\Gamma - \int_{\Omega_e} \nabla \tau_j \cdot (\underline{u}_{ed} C) d\Omega = 0 \quad \forall e,$$

where $\{\cdot\}$ is the average value at the interface, such that $\{\underline{u}_{ed}\} = \frac{\underline{u}_{ed}^+ + \underline{u}_{ed}^-}{2}$ with \underline{u}_{ed}^- and \underline{u}_{ed}^+ being the velocity at both sides of the boundary across the element. In ocean models, local consistency must be enforced (White et al., 2008b). This requires that, if there is no source or sink, a constant tracer concentration is conserved in a closed domain. Expressing the velocity \underline{u}_{ed} as a function of the discrete field $\underline{\psi}^h$ and setting C=1, the local tracer consistency criterion becomes (see appendix A1 for more details):

$$\sum_{i} \left[\left(\frac{\psi_{iy}^{-} - \psi_{iy}^{+}}{2} \right) \int_{\Omega_{e}} \left(\frac{\partial \tau_{i}}{\partial x} \frac{\partial \tau_{j}}{\partial z} - \frac{\partial \tau_{i}}{\partial z} \frac{\partial \tau_{j}}{\partial x} \right) d\Omega + \left(\frac{\psi_{ix}^{-} - \psi_{ix}^{+}}{2} \right) \int_{\Omega_{e}} \left(\frac{\partial \tau_{i}}{\partial z} \frac{\partial \tau_{j}}{\partial y} - \frac{\partial \tau_{i}}{\partial y} \frac{\partial \tau_{j}}{\partial z} \right) d\Omega \right] = 0,$$
(3.6)

where $\psi_{i\ y}^-$ is the y-component of the streamfunction induced by the eddies ψ at the node i and at the left-hand side of the interface. It appears that, if $\underline{\psi}^h$ is continuous, the tracer equation is consistent. Thanks to the form of relation (3.6), this property is also satisfied if \widetilde{Y} is continuous. Moreover, the global tracer conservation is obtained (the details are presented in the appendix A2). Equation (3.3) is solved implicitly using the Newton's method in order to ensure impermeable domain boundaries. Otherwise, the solution would be a less good approximation.

3.3.2 DGFEM formulation of the diffusive part

The usual Galerkin finite element formulation of the tracer equation without the advection term and the Gent-McWilliams velocity is:

$$\int_{\Omega} \left(\frac{\partial C}{\partial t} - \nabla \cdot (\underline{\underline{\kappa}}^{S} \cdot \nabla C) \right) \tau_{j} d\Omega = 0$$

$$\Leftrightarrow \int_{\Omega} \frac{\partial C}{\partial t} \tau_{j} d\Omega = - \int_{\Omega} \nabla \tau_{j} \cdot \underline{\underline{\kappa}}^{S} \cdot \nabla C d\Omega + \int_{\partial \Omega} \underline{n} \cdot \underline{\underline{\kappa}}^{S} \cdot \nabla C \tau_{j} d\Gamma.$$

To obtain the discontinuous Galerkin (DG) formulation, the integral over the whole domain Ω is decomposed into the sum of integrals over each element and

⁶The complete formulation (advection and diffusion) of the dgFEM discretization includes penalty terms, but here they are not present since only the advective part is present and does not need to be stabilized.

the interface term is computed over each face:

$$\sum_{e} \int_{\Omega_{e}} \frac{\partial C}{\partial t} \tau_{j} \ d\Omega = -\sum_{e} \int_{\Omega_{e}} \nabla \tau_{j} \cdot \underline{\underline{\kappa}}^{S} \cdot \nabla C \ d\Omega + \sum_{k} \int_{\gamma_{k}} \underline{n} \cdot \underline{\underline{\kappa}}^{S} \cdot \nabla C \ \tau_{j} \ d\Gamma.$$

In DGFEM, the weak formulation consists in finding C such as $a(C,\tau) = b(\tau)$, where a is a bilinear form and b is a linear form. The right-hand side term of the equation is replaced by the bilinear form (Rivière, 2008), which is defined as:

$$a(C,\tau) = -\sum_{e} \int_{\Omega_{e}} \nabla \tau_{j} \cdot \underline{\underline{\kappa}}^{S} \cdot \nabla C \, d\Omega$$

$$+ \sum_{k} \int_{\gamma_{k}} \left([[\tau_{j}]] \cdot \{\underline{\underline{\kappa}}^{S} \cdot \nabla C\} + [[C]] \cdot \{\underline{\underline{\kappa}}^{S} \cdot \nabla \tau_{j}\} + \mu[[C]] \cdot [[\tau_{j}]] \right) \, d\Gamma$$

$$= -\sum_{e} \int_{\Omega_{e}} \nabla \tau_{j} \cdot \underline{\underline{\kappa}}^{S} \cdot \nabla C \, d\Omega + \sum_{k} \int_{\gamma_{k}} [[\tau_{j}]] \cdot \{\underline{\underline{\kappa}}^{S} \cdot \nabla C\} \, d\Gamma$$

$$\vdots$$

$$+ \sum_{k} \int_{\gamma_{k}} [[C]] \cdot \{\underline{\underline{\kappa}}^{S} \cdot \nabla \tau_{j}\} \, d\Gamma + \sum_{k} \int_{\gamma_{k}} \mu[[C]] \cdot [[\tau_{j}]] \, d\Gamma, \qquad (3.7)$$

$$\textcircled{2}$$

where [[.]] is the jump vector at the interface such that $[[C]] = \underline{n} \frac{C^+ - C^-}{2}$ and μ is the penalty factor. The term ① stems from the divergence theorem and the integration by parts. The interior penalty (IP) terms, i.e., the symmetric interior penalty term ② and the penalty term ③, stabilize the diffusion in the discontinuous Galerkin method. Hence, the value of μ must be chosen carefully. If μ is not large enough, the bilinear form does not satisfy the property of coercivity which ensures that the problem is well-posed, i.e., uniqueness and continuity. Hence, the approximate solution is not stable and numerical artifacts such as spurious oscillations that deteriorate the quality of the solution appear. But, if μ is too large, too much numerical diffusion is involved, which leads to a poor approximation of the solution (Shahbazi, 2004). In Pestiaux et al. (2014), an oriented penalty factor, which only takes into account the diffusion in the normal direction to the interface, is selected when the diffusivity tensor is strongly anisotropic. It is defined as follows:

$$\mu = \frac{(k+1)(k+d)}{d} \frac{A_k n_0}{2V_e} \ \underline{n} \cdot \underline{\underline{\kappa}} \cdot \underline{n},$$

where d is the dimension, k the degree of the polynomial shape function, A_k the area of the interface, V_e the volume of the element and n_0 the number of

neighbors of the element, i.e., $n_0 = 5$ for prisms.

The local tracer consistency and conservation properties are easily obtained for the diffusion equation. When the tracer concentration is constant in time and space, its gradient is null and the consistency property is satisfied. In other cases, the divergence theorem is used for the diffusion term and the Dirichlet boundary condition is then applied on the interface term. Only the time integration remains, which means that the tracer concentration is conserved. Moreover, as this parameterization is added in SLIM, the monotonicity can be achieved in the advection scheme by means of slope limiters (Kärnä et al., 2012). This method is a common cure when some nonphysical oscillations around high gradient discontinuities which sometimes appear are enough severe to cause stability problem.

3.4 Investigation of the vanishing isoneutral flux

The vanishing of the isoneutral flux consists in preserving the density field, while the temperature and salinity tracer concentrations are diffused by the isopycnal diffusion. This characteristic is important since this diffusion should not affect the buoyancy field, and thus it should not diffuse the locally referenced potential density. Even if this feature is easily guaranteed with a continuous discretization when a linear equation of state is used, it is more complex with DGFEM. As the diffusion equation is linear, solving the isopycnal diffusion for both temperature and salinity tracers and deducing the density as a diagnostic is exactly equivalent to iterating the isopycnal diffusion on the density field itself, in both discretizations. For the sake of simplicity, a linear equation of state is chosen but it is not a realistic choice for all oceanic areas.

The seawater density is a strongly non-linear function of temperature and salinity. In cold regions, it becomes nearly linear with respect to salinity, whereas in warm regions it is nearly linear with respect to temperature. Therefore, it is also useful to study how tracer concentrations behave in these areas. For this reason, a linear expression of the density is considered:

$$\rho(T, S) = \rho_0 + a(T - T_0) + b(S - S_0),$$

where a and b are the thermal expansion and saline contraction coefficients⁷, respectively, and T_0 and S_0 are the constant reference temperature and salinity. Because of the linearity of the tracer equation (3.1) applied on T and S without the antisymmetric part of the diffusivity, they can be multiplied by a and b,

⁷In OGCMs, these coefficients are usually function of the temperature and salinity fields. Nowadays, this approximation is still a topic of discussion for scientists.

respectively, and then added to obtain an equation for the evolution of the density:

$$a\frac{\partial T}{\partial t} + b\frac{\partial S}{\partial t} = \frac{\partial \rho}{\partial t} = \nabla \cdot (\underline{\underline{\kappa}}^S \cdot \nabla \rho).$$

Since there are discontinuities with the DG approximation, the density gradient can be defined in several ways. On the one hand, $\underline{\kappa}^S$ is computed from the slope \tilde{s} which is obtained from the gradient of the density using (3.2). In order to have a good estimate $\underline{\nu}^h$ of $\underline{\nu} = -\nabla \rho$, the discretization of the following weak formulation, obtained after integration by parts, is used:

$$\int_{\Omega} \underline{\nu} \ \tau \ d\Omega = -\int_{\Omega} \nabla \rho \ \tau \ d\Omega$$

$$= -\int_{\Gamma} \underline{n} \left\{ \rho \right\} \tau \ d\Gamma + \sum_{e} \int_{\Omega_{e}} \rho \nabla \tau \ d\Omega \quad \forall \tau. \quad (3.8)$$

It is important to compute the gradient of ρ in this way in order to take into account the discontinuities at the interfaces. On the other hand, deriving the finite element approximations of the tracer concentration C is achieved in a standard way by taking the gradient of the shape functions:

$$\nabla C^h = \sum_i C_i \nabla \tau_i, \tag{3.9}$$

where τ_i is the shape function related to node *i*. The gradient of the density can be computed in the same way:

$$\nabla \rho^h = a \ \nabla T^h + b \ \nabla S^h. \tag{3.10}$$

Hence, the equation of evolution can be written as:

$$\frac{\partial \rho^h}{\partial t} = \nabla \cdot (\underline{\underline{\kappa}}^S \cdot \nabla \rho^h),$$

where $\rho^h = \rho(T^h, S^h)$. Looking at the diffusivity flux without diapycnal diffusion (i.e., $A^D = 0$ and $A^I > 0$), it yields:

$$\underline{\kappa}^S \cdot \nabla \rho^h \quad = \quad A^I (\underline{\delta} - \underline{\widehat{\nu}}^h \ \underline{\widehat{\nu}}^h) \cdot \nabla \rho^h,$$

where $\widehat{\underline{\nu}}^h = \frac{\underline{\nu}^h}{\|\underline{\overline{\nu}}^h\|}$. After distribution, its becomes:

$$\underline{\underline{\underline{\varepsilon}}}^S \cdot \nabla \rho^h = A^I \left(\nabla \rho^h - \underline{\widehat{\nu}}^h \ (\underline{\widehat{\nu}}^h \cdot \nabla \rho^h) \right) = 0 \quad \text{if} \quad \nabla \rho^h \quad \propto \quad \underline{\widehat{\nu}}^h, \quad (3.11)$$

i.e., the isoneutral flux of density vanishes if the finite element approximations of the gradient of the density and the diapycnal unit vector are aligned.

In the continuous Galerkin finite element method, the relation (3.11) is satisfied since $\hat{\nu}^h$ in the isopycnal diffusivity is simply computed by interpolation of the gradient of the shape function. Moreover, there is no penalty term in equation (3.7). To illustrate this property, the tracer equation is integrated in

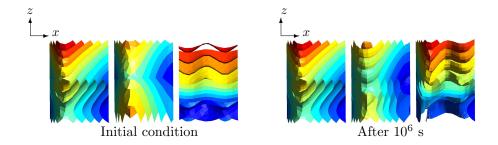


Figure 3.4: Illustration from Comblen (2010) of the vanishing isoneutral fluxes on a toy problem. Both panels are cross-sections of a domain $1000km \times 1000km \times 1000m$. The left panel represents the temperature (right) and the salinity (center) that are used to compute the density (left), all at the initial time. After 10^6 seconds, these same fields are showed on the right panel. As expected, the density (left) does not change even if salinity (center) and temperature (right) exhibit large variations.

time for both temperature and salinity; then, the density is deduced as a diagnostic. This scheme is exactly equivalent as computing the isopycnal diffusion on the density itself since the equation of state is linear. Therefore, temperature and salinity can be diffused strongly, whereas the density is preserved, as represented in Figure 3.4.

In the discontinuous Galerkin method, it is not possible to guarantee the vanishing isoneutral flux of the density even when the equation of state is linear. In general, the terms ② and ③ in equation (3.7) do not disappear. Moreover, $\nabla \rho^h$ is not aligned with $\underline{\widehat{\nu}}^h$ even though their corresponding continuous fields satisfy $\nabla \rho = -\underline{\widehat{\nu}} \|\nabla \rho\|$ since the relation (3.8) is used instead of interpolation of the gradient of the shape function. The penalty factor μ in ③ could be imposed to be zero when the diffusivity flux is zero. However, this condition would imply a non-linear discretization scheme and it would not necessarily guarantee the stability.

When an advection term is present, the discontinuous Galerkin method is really advantageous. But, for pure diffusion, the continuous Galerkin method is a more appropriate choice. When advection is present in CG, a stabilization term is also necessary if the Peclet number is larger than one; i.e.,

$$\frac{h\|v\|}{k} > 1,$$

where h is the element length, v is the velocity and k is the constant diffusivity. In that case, numerical diffusivity is introduced and thus the vanishing property will also be lost with the continuous discretization. The vanishing isoneutral flux is thus a difficult feature to obtain. Even a linear equation of state is not sufficient to satisfy this property, so that an equation of state better adapted for all oceanic areas appears to remain the best choice to describe the density field at best. In this approach, the Jackett and McDougall equation of state (McDougall et al., 2006) is usually employed in SLIM.

3.5 Results

In this section, the GM velocity and the isopycnal diffusion are analyzed in order to highlight their behaviour in the framework of SLIM. First, the effects of isopycnal diffusion are analyzed in a progressively inclining density field. Next, the spurious flux in the diapycnal direction is studied and compared to the existing diapycnal diffusion. Finally, an application to an idealized channel is studied when a regular temperature field with a constant stratification is tilted due to the surface wind forcing. In the two first simulations, only the tracer equation without the advection term is considered. For the last simulation, all the governing equations are solved in the cartesian coordinates on an ocean sector domain.

3.5.1 Illustration of the isopycnal diffusion

First, only the symmetric part of the isopycnal tensor is implemented in the framework of SLIM. The aim is to see the effect and the rate of tracer diffusion. As the diffusivity tensor is not aligned with the mesh, it is really important to know if the tracer concentration tends to follow isopycnals. A cylindrical geometry with a 200m depth and a radius of $10^4 {\rm km}$ is meshed with 30 layers of prismatic elements whose horizontal characteristic length is about $10^5 {\rm m}$. To build the tensor $\underline{\kappa}^S$ with $\epsilon=10^{-7}$ and $A^I=1000~[m^2/s]$, a simple analytical density is created from the equation:

$$\rho(x,z) = 1035 \left(1 - 50 \frac{z}{l} \sin\left(\frac{5(x-l)}{2\pi l}\right)\right) [kg/m^3],$$

where $l=10^6\mathrm{m}$. This density shape was chosen since its slope increases progressively. Moreover, the tracer concentration evolution under the isopycnal diffusivity will be easier to observe.

3.5. Results 67

A normalized tracer concentration is selected to observe the diffusivity rate. The initial state of this tracer concentration is chosen as a Gaussian function which takes advantage of the axial symmetry:

$$C(\underline{x},0) = e^{-\left(\frac{(y-0.3l)^2 + (x-0.55l)^2}{2.10^{10}} + \frac{(z+100)^2}{200}\right)}.$$

In order to emphasize the tilt of the tracer concentration with time, the tracer fields are put on the density field. The numerical scheme is solved with an explicit Runge-Kutta scheme of order 3 and a time step of one day. In Figure

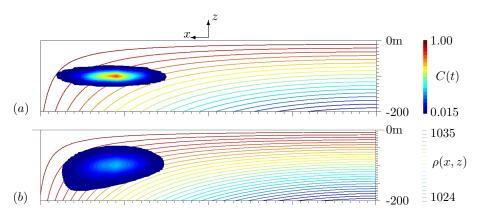


Figure 3.5: (a) Initial distribution of the tracer concentration $C(\underline{x}, t = 0)$ placed in the density field $\rho(x, z)$; (b) Evolution of the tracer concentration after 20 days placed in the same density field.

3.5, the isopycnals are illustrated by the colored lines and the tracer concentration is shown with the full shape on the same domain. In the bottom panel, it is diffused as well as it tends to follow the isopycnals. On the right hand side, it goes downwards, while on the left hand side, it goes slightly upwards. Usually, in ocean models, slope limiters are introduced in order to avoid infinite slopes in the computation of the diffusivity tensor and thus numerical instabilities. Nevertheless, for this illustration, none was considered. The diapycnal diffusion will be studied in the next section.

3.5.2 Spurious flux

As the diffusivity tensor is not aligned with the mesh, the diffusivity is more complex and the numerical errors appear more easily. The main idea is to only consider isopycnal diffusivity and to study the spurious flux in the diapycnal direction. Already considered by Shah et al. (2011) but with a non-flat

isopycnal surface, this kind of idealized test case allows to highlight the intrinsic properties of the isopycnal diffusion. Let us consider a simple density field with two planar isopycnals and assume no diapycnal diffusion, i.e., $\epsilon=0$. Initially, a small concentration of tracer (a Gaussian distribution) is placed on the isopycnal interface (Figure 3.6). If ocean models were perfect, the tracer concentration would follow the isopycnal direction. In practice, however, the tracer is diffused also in the diapycnal direction due to spurious numerical flux. The spurious flux can be measured by computing the tracer variance in the diapycnal direction.

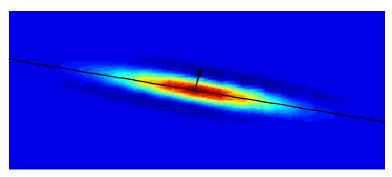


Figure 3.6: A tracer concentration initially placed on the isopycnal interface (black line) is diffused but not only along the isopycnal. The spurious flux is then computed in following the diapycnal direction (black vector).

The center of gravity of the tracer concentration is defined as:

$$\underline{\underline{x}}(t) = \frac{\int_{\Omega} C(\underline{x}, t) \ \underline{x} \ d\Omega}{\int_{\Omega} C(\underline{x}, 0) \ d\Omega},$$

where $C(\underline{x},t)$ is the tracer concentration. The variance can be written as:

$$\sigma^2 = \frac{\int_{\Omega} C(\underline{x}, t) \ \|\underline{x} - \underline{\check{x}}(t)\|^2 \ d\Omega}{\int_{\Omega} C(\underline{x}, 0) \ d\Omega}.$$

If the isopycnals have a small slope, the distance $\|\underline{x} - \underline{x}(t)\|^2$ can be approximated by $\|z_i - z_t\|^2$, where z_i and z_t are the z coordinate of the isopycnal and the tracer concentration, respectively. Figure 3.7 shows the result of a simulation of 90 days with a time step of 10 days. The evolution appears to be linear which means that the tracer concentration distribution moves away from the isopycnal. As the variance of the spurious flux grows approximately with t, this spurious flux can be defined as a spurious diffusivity (Karger, 1992).

3.5. Results 69

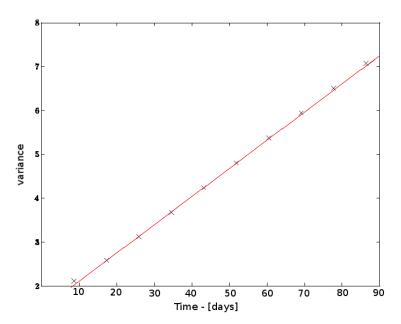


Figure 3.7: Evolution of the tracer variance in the diapycnal direction with time $(\Delta t = 10 \ days)$.

In order to compare this spurious diffusivity in the diapycnal direction, a diapycnal diffusion where the analytical solution should be a Gaussian distribution is considered. Hence, the variance of this Gaussian distribution should follow the law 2kt, where k is, in this case, the constant diapycnal diffusivity. The range of k is then about $[10^{-5}, 10^{-4}] \ m^2/s$. This law is also applied on the observed spurious diffusivity. As the computed variance has a slope of around $9 \cdot 10^{-7} \ m^2/s$, it is thus associated to a diffusivity k_v . This method allows to easily compare the spurious diffusivity with the diapycnal one, and it appears that the spurious diffusivity is weaker than the diapycnal diffusivity since:

$$k_v = 9 \cdot 10^{-7} \ m^2/s$$

 $\ll k \in [10^{-5}, 10^{-4}] \ m^2/s$

In this study, the discretization and parameterization are seen to be well suited to our model since this spurious flux is negligible. The numerical errors associated to the isopycnal diffusion should not thus deteriorate the results.

3.5.3 Application to an idealized channel

Since the oceanic model used in this study (SLIM) is still in development, long global simulations with high resolution are not currently possible, and complex tracer concentration fields cannot be simulated in details as they can be observed in the real ocean. In order to examine the effects of the GM velocity, a simplified domain is thus chosen. Inspired by laboratory studies (Marshall et al., 2002; Henning and Vallis, 2004), an idealized configuration is the channel shown schematically in Figure 3.8. The domain extends from 30°

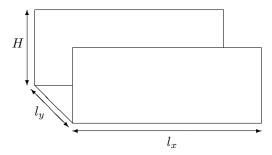


Figure 3.8: A schematic drawing showing the domain used in the idealized simulations. Subject to a periodic boundary condition, this channel is characterized by its depth H, its width l_y and its length l_x .

to 45° in latitude (the Coriolis parameter f is taken as $2\Omega \sin(35)$) and from 0° to 20° in longitude, with 23 vertical layers of increasing thickness up to 1600m. The mesh, composed of quadrilateral elements, has a horizontal resolution of 1° × 1°. This channel is subject to a periodic boundary condition in the zonal direction. A constant gradient of temperature defined as $T(z) = 26 - 8 \cdot 10^{-3} z$ and a constant salinity of 30 psu are used for the initialization. The model forcing consists of a surface wind stress defined as follows:

$$\left\{ \begin{array}{ll} \tau_x = \left\{ \begin{array}{ll} 0.2 \sin \left(\pi \frac{l_y - 4y}{2l_y} \right) & \text{if} \ y \in \left[-\frac{l_y}{2}, \frac{l_y}{2} \right], \\ 0 & \text{if} \ y \notin \left[-\frac{l_y}{2}, \frac{l_y}{2} \right], \\ \tau_y = 0. \end{array} \right.$$

where the meridional length $l_y=15.10^4{\rm km}$. There is no sea surface temperature restoring.

In this study, SLIM is based on Kärnä et al. (2012). To achieve a realistic oceanic simulation, the 3D hydrostatic Boussinesq equations are considered.

3.5. Results 71

With the velocity decomposed as $\underline{U} = (\underline{u}, w)$, the horizontal momentum equation is given by:

$$\frac{\partial \underline{u}}{\partial t} + \nabla_h \cdot (\underline{u} \ \underline{u}) + \frac{\partial (w \ \underline{u})}{\partial z} + f \underline{\widehat{e}_z} \times \underline{u} + \frac{1}{\rho_0} \nabla_h p = \nabla_h \cdot (\nu_h \nabla_h \underline{u}) + \frac{\partial}{\partial_z} \cdot \left(\nu_v \frac{\partial \underline{u}}{\partial z} \right),$$

where f is the Coriolis factor. The horizontal and vertical viscosities are $\nu_h = 3.5 \ 10^4 m^2/s$ and $\nu_v = 10^{-4} m^2/s$, respectively. The hydrostatic assumption reduces the vertical momentum equation to

$$\frac{\partial p}{\partial z} = -g\rho(S, \theta, p),$$

where ϑ is the potential temperature and p the oceanic pressure. The seawater density is computed from the Jackett and McDougall equation of state (McDougall et al., 2006):

$$\rho(S, \vartheta, p) = \frac{P_{12}(S, \vartheta, p)}{P_{13}(S, \vartheta, p)},$$

where P_{12} and P_{13} are polynomial functions of 12 and 13 terms, respectively. The continuity equation reads

$$\nabla_h \cdot \underline{u} + \frac{\partial w}{\partial z} = 0,$$

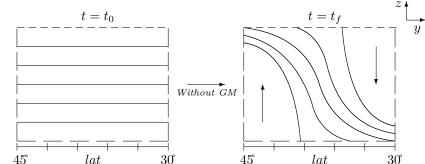
from which the vertical velocity is computed. Finally, the tracer equation with the advection term is considered:

$$\frac{\partial C}{\partial t} + \nabla \cdot ((\underline{u}_{ed} + \underline{U}) \ C) = \frac{\partial}{\partial z} \left(\lambda_v \frac{\partial C}{\partial z} \right),$$

where \underline{u}_{ed} is the Gent-McWilliams velocity and the vertical diffusion coefficient λ_v is computed with the parameterization of Pacanowski and Philander (1981). This parameterization of vertical mixing is particularly useful when there are small vertical temperature gradients and large wind-induced shear. Because of the absence of salinity variation, the isopycnal diffusion has in this case a null tensor and does not influence the simulation. Since the potential density is computed from the Jackett and McDougall equation, some static instabilities can appear during the simulation. Hence, when a parcel of water with a potential density ρ_1 is below another parcel of potential density ρ_2 such that $\rho_1 < \rho_2$, the water column is unstable. In nature, convective processes quickly re-establish the static stability of the column. Since these processes are not included in our ocean model due to the hydrostratic assumption, a convective adjustment scheme is added to account for this effect (Marotzke, 1991). Various techniques can be applied such as a non-penetrative convective adjustment, a

turbulent closure scheme or an enhanced vertical diffusivity. The latter is used in this study in addition to the Pacanowsky-Philander parameterization. It consists in enlarging the vertical diffusivity to 1 $[m^2/s]$ when the stratification is unstable. Such instabilities happen when the Brunt-Vaïsälä frequency N_b^2 is negative (Madec and team, 2008). For the time integration, the coupled 2D-3D water equations are considered. The 3D equations advance in time with the split-explicit scheme from Shchepetkin and McWilliams (2005). In the predictor stage, the tracer concentration C is updated from the time $t_{n-1/2}$ to $t_{n+1/2}$ with the third order Leap-frog-Adams-Moulton (LF-AM3) numerical algorithm. After, the 2d equations are solved separately from t_n to t_{n+1} with smaller time steps thanks to a standard third order Adams-Bashforth (AB3) scheme. Then, the corrector stage gives C at the time t_{n+1} and is completed by a semi-implicit evaluation of the vertical diffusion of momentum and the tracer concentrations.

In order to highlight the positive effects of the GM velocity, two different simulations are run over 6 years. In the "standard run", the idealized test case described above is runned without any eddy parameterization, whereas the GM velocity is included in the second one and called "GM run". It is important to notice that both simulations only differ in the addition of the GM velocity; all the other parameters and equations are the same in each case. The key idea



 45° lat 30° 45° lat 30° Figure 3.9: A schematic drawing of vertical cross-sections, showing the evolution of the isotherms (full lines) from the initial time (left) and to the end of the simulation (right) when the GM velocity is not taken into account. On the right hand-side pannel, the Ekman pumping (represented by the vectors), which is created under the action of winds, tends to strongly tilt the slope of the isotherms.

of this test case is that the thermal wind balance with the density gradient acts to overturn the isopycnals. From a theoretical point of view, the initial flat temperature field will undergo Ekman pumping and, without the GM parameterization, the isotherms will become nearly vertical in some places, as

3.5. Results 73

illustrated in Figure 3.9. Indeed, an oceanic simulation without eddy parameterization leads to the formation of vertical isopycnals (Vallis, 2000), and thus to high instabilities. Without the GM velocity, this field will be almost vertical at the bottom of the channel because the resolution is too coarse, and this representation will not be realistic at all. Moreover, they will be compressed at the surface on the eastern side and at the bottom on the western side of the domain. This situation will lead to an accumulation of cold water at the southern bottom and of warm water at the northern surface. These main characteristics should be observed in the standard run conducted with SLIM. When the extra velocity is added, the density slope will tend to become smooth at the bottom, even with a coarse resolution. This difference of steepness will thus be studied in this section.

Meridional potential temperature sections from both runs, that are here equivalent to density sections since the salinity is constant, are shown in Figure 3.10. Since the mesh resolution is coarse, the simulated temperature fields are quite uneven because of the DG formulation. Indeed, the large variations of temperature between two neighbouring elements lead to large jumps between these two elements, and thus to some scattered fields. A finest mesh resolution should improve this issue but it should also require a much larger computational time or a best efficiency of the solver. In order to avoid this issue and to make the results interpretation easier, both temperature results have been discretized in continuous fields. In the standard run, the principal characteristics highlighted through the theoretical illustration are found in Figure 3.10 (left). Indeed, some isotherms at mid-latitudes are getting extremely steep, almost vertical, under the action of wind without eddies. Transient motions are present, but they are by far insufficient to properly smooth the slope. Moreover, there is an accumulation of cold water that remains at the southern bottom. Nevertheless, the accumulation of warmer water at the northern surface is missing. The convective adjustment as well as the Pacanowsky-Philander parameterization which have been added in these simulations in order to remove static instabilities could be responsible for this difference with the theory. The main differences between both panels are the cold deep water which slowly slumps in the GM run, and the isotherm slope which tends to become less steep than in the standard run.

As expected, this GM velocity have a pronounced effect on the circulation in the channel. The real oceanic system is of course more complex than the model presented here. The invariability of salinity and the simplified geometry are indeed large simplifications. Nevertheless, eddies greatly influence the stratification, and the transport too, which are scaled by the relative strength of wind and diffusion. In addition to the smoother slopes, the other observed effect is the larger vertical diffusion in the standard run. Since the isotherms

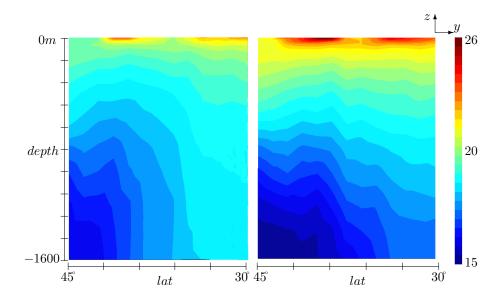


Figure 3.10: Comparison between the vertical cross sections of temperature discretized in a continuous field for the standard run (left) and for the GM run (right) after 6 years of simulation.

are very steep, they are highly baroclinically unstable. This situation leads to large spaces between these isotherms. In the GM run, the eddy parameterization creates quite uniformly spaced isotherms, presumably a consequence of its tendency to homogenize isopycnal layers (Henning and Vallis, 2004). In this way, the temperature decreasing from the surface to the bottom is slower in this last run. The expected behavior is noticed: the isotherms are slumped and the available potential energy is released, as minimizing the artifacts of the penalty term.

3.6 Concluding remarks

In this paper, we present the discretization of the Gent-McWilliams velocity and the isopycnal diffusion with the discontinuous Galerkin finite element method. In order to deal with the issues related to the boundary conditions, the boundary-value problem suggested by Ferrari et al. (2010) for the Gent-McWilliams velocity is adapted in this discretization and, to ensure impermeable boundaries, a Newton solver is used. Thanks to a continuous streamfunction \widetilde{Y} , the computed velocity field is numerically consistent with the tracer

equation in such a way that the constant tracer concentration is preserved.

In the discussion of the vanishing isoneutral flux, it appears that this flux of density cannot be guaranteed in the discontinuous Galerkin method. But in presence of advection, this method remains just as advantageous as the continuous Galerkin method. In this last case, even the CG method lost this property. In the analysis of the isopycnal diffusion effects, the tracer concentration tends, as expected, to align itself along the density field. Besides, the spurious diapycnal mixing remains much smaller than the physical diapycnal diffusion when a Gaussian distribution is used as tracer concentration field. Moreover, the numerical error relative to this spurious diapycnal mixing is accordingly negligible. At the end, the idealized channel simulation revealed that the GM velocity affects, as expected, the temperature field, which is, in this case, equivalent to study the density field. Without the GM parameterization, the isotherms are getting extremely steep under the action of wind since the transient motions are by far insufficient to properly smooth their slopes. When the GM parameterization is taken into account, the available potential energy is released in such a way that the isotherms are slumped. Moreover, the stratification at the ocean surface is greatly influenced by this mesoscale parameterization.

To the best of our knowledge, it is the first time that the Gent-McWilliams velocity and isopycnal diffusion processes are included in a discontinuous Galerkin finite element ocean model, thanks to, respectively, the boundary-value problem suggested by *Ferrari* and a special treatment of the stabilization of the numerical scheme with the oriented penalty factor. The first results highlight the performance of the isopycnal diffusion in simple test cases, and the idealized channel simulation goes on the same track for the Gent-McWilliams velocity but for a more complete oceanic simulation where all the governing equations are considered. Future work could be devoted to an improvement of the oceanic model in order to save the computational time and to realize some larger or global simulations. In this way, the impacts of mesoscale eddies could be analyzed on a longer run and in more complex regions, such as in the Gulf Stream or in the Southern Ocean. Such studies could allow a better understanding of these complex and still not well-known processes.

C H A P T E R

The coupled model FESOM-LIM3

Summary

In this chapter, key components of the sea ice model LIM3 are coupled with the global ice-ocean model FESOM in order to combine the advantages of each model. Thanks to the finite element discretization, and thus to unstructured meshes, FESOM allows to locally increase the mesh resolution and to better represent the coastlines. LIM3 brings halo-thermodynamics with a subgrid-scale representation of the ice thickness. First, each model is described and the coupling strategy is presented. Then, preliminary calibration simulations are performed and analyzed in order to adjust the albedo parameterization in FESOM-LIM3 and prepare a model configuration suitable for long-term simulations.

4.1 Introduction

Sea ice models basically consist of two components: thermodynamic and dynamic. Since the heat transfers across the sea ice occur mostly along the vertical direction, the evolution of sea ice thickness by thermodynamic growth or melt can be computed from the atmospheric and oceanic forcings at any location without any horizontal interaction with neighbouring sea ice. From this perspective, Maykut and Understeiner (1971) developed the first thermo-

dynamic sea ice model, later simplified by Semtner (1976) by keeping its most important components. Sea ice models are frequently based on these latter simple models, called the 0- and 3-layer models. Following their configurations, they allow to simulate the landfast ice evolution (Flato and Brown, 1996) or study the sea ice sensitivity to atmospheric drag coefficients (Lüpkes et al., 2012). On the other hand, the dynamic processes relate to the ice drift in response to wind and oceanic currents, the Coriolis force, the force due to the tilt of ocean surface and the internal sea ice forces. The viscous-plastic representation suggested by Hibler (1979) knew many successes but it was not well suited for efficient parallel integrations because it must be solved with an implicit method (Zhang and Rothrock, 2000). The elastic-viscous-plastic (EVP) formulation, with an easy parallelization, is the most popular alternative (Hunke and Dukowicz, 1997) and has been adopted by numerous GCMs (Randall and Taylor, 2007; Montoya et al., 2005).

The Louvain-la-Neuve sea Ice Model (LIM) is a state-of-the-art three-dimensional global model of sea ice designed for climate studies. Its latest version, LIM3 (Vancoppenolle et al., 2009b), is fully coupled with the oceanic general circulation model OPA (Ocean PArallélisé) on the modelling platform NEMO (Nucleus for European Modelling of the Ocean). Like the majority of sea ice models, it is based on structured grids and finite difference schemes because of their ease of implementation and runtime efficiency. However, coastlines are not well defined and a finest mesh resolution requests a larger computational time. A way to overcome these issues is to opt for unstructured meshes which allow local adaptation of the mesh at anytime and the improvement of the resolution near the coasts (van Scheltinga et al., 2010).

Both finite element and finite volume methods used by a number of new models (Chen et al., 2003; Ford et al., 2004; Fringer et al., 2006; Kärnä et al., 2012) gave some promising results in the oceanic simulations. Yet, in 1975, Fix (1975) highlighted the advantages of such methods in GCMs: easier handling of energy conservation, natural treatment of the boundary conditions and mesh flexibility. The finite element method is based on a variational formulation which enables to treat the complex boundary conditions as natural or free boundary conditions. But this method remains computationally expensive and quite complex. In particular cases, finite element methods have early been suggested for sea ice modelling in order to simulate the cracks propagation in sea ice (Mukherji, 1973). More idealized investigations were thereafter performed about sea ice rheology or motion in specific areas (Thomson, 1988; Schulkes et al., 1998; Kliem, 2001; Wang and Ikeda, 2004). Some regional studies were then achieved (e.g., Schulkes et al., 1998; Yakovlev, 2003; Wang and Ikeda, 2004; Sulsky et al., 2007; Lietaer et al., 2008; Wekerle et al., 2013). Among them, Lietaer et al. (2008) was the first to investigate the effects of resolving the Canadian Arctic Archipelago on the Arctic ice cover features. Indeed, 10% of the annual sea ice volume is enclosed in this area and its omission considerably influences the freshwater balance of the Arctic.

The Finite Element Sea ice-Ocean Model (FESOM, Danilov et al., 2004; Wang et al., 2008; Timmermann et al., 2009) is a sea ice-ocean general circulation model using unstructured triangular surface meshes. (Sidorenko et al., 2011) showed that FESOM is now ready to be considered as a reliable tool or studying the large-scale ocean general circulation. Recently, Wekerle et al. (2013) showed that increasing the mesh resolution in the Canadian Arctic Archipelago improves the simulation of the freshwater export interannual variability. In addition, these results indicate that the multi-resolution allows small-scale processes such as some fluxes to influence the large-scale circulation. While the model produces realistic estimates of the sea ice cover, the relative simplicity of its sea ice thermodynamic component can be significantly improved.

In this study, key components of LIM3 are coupled to FESOM in order to integrate the multi-category representation of the sea ice thickness, the halodynamics and thermodynamics of sea ice, the mechanical and thermodynamical redistributions, while keeping the advantages of the finite element discretization. For the sake of simplicity, the coupling of all these processes in LIM3 will hereafter be referred to as the coupling of LIM3 with FESOM.

4.2 Description of the models

In the following subsection, the ocean model as well as the sea ice dynamics and thermodynamics of FESOM are presented. Then, the sea ice model LIM3 in its initial configuration is introduced with a brief description of the sea ice thermodynamics, halodynamics, dynamics, Ice Thickness Distribution (ITD), mechanical and thermodynamical redistributions and the atmospheric fluxes used.

4.2.1 **FESOM**

FESOM was the first GCM using unstructured meshes that was developed for the purpose of climate research. The global version that we use here is discretized using the finite element method (Danilov et al., 2004; Wang et al., 2008; Timmermann et al., 2009). The grid is composed of tetrahedral elements, so that an unstructured mesh of triangles materializes the ocean surface (Figure 4.1). As the model equations are solved with the finite element method, linear basis functions are utilized for velocity, tracers and sea surface elevation, leading

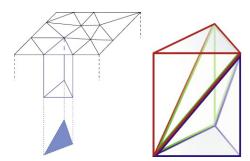


Figure 4.1: Illustration of the three-dimensional mesh of FESOM (left) where the surface mesh is composed of triangular elements and where the resulting prisms are split into three thetrahedra (right) [figures from S. Harig (AWI)].

to the continuous representation (the so-called $P_1 - P_1$ discretization) of the model variables.

Ocean model

The oceanic component of FESOM is the hydrostatic primitive-equation Finite Element Ocean Model (FEOM) initially developed by Danilov et al. (2004). The standard set of hydrostatic primitive equations under the Boussinesq approximation are solved and the North Pole is placed in Greenland to avoid the North Pole singularity. Continuous linear representations of temperature, salinity, horizontal velocities and sea surface elevation are used. The tracer equation is solved with an explicit flux-corrected-transport scheme (Lohner et al., 1987). A semi-implicit discretization for the Coriolis term is utilized for the time-stepping of the momentum equation, an implicit discretization for the viscosity and surface elevation, and an explicit scheme for momentum advection and pressure contribution. The solver proceeds in three steps: (i) a predictor step for the horizontal velocity, (ii) an update of the surface elevation, and (iii) a correction for the horizontal velocity. Last, the vertical velocity is diagnosed. The temperature and salinity time-stepping uses the explicit second-order Taylor-Galerkin scheme (Wang et al., 2014), and a no-slip boundary condition is applied along the coasts.

To parameterize the subgrid-scale processes, the Redi diffusion (Redi, 1982) and the Gent-McWilliams parameterization (Gent and McWilliams, 1990) are applied with a critical neutral slope of 0.004. The skew and isopycnal diffusivity are both parameterized as $V\Delta$, where V=0.006~m/s is the bolus velocity and Δ is the square root of the surface triangle area. Moreover, the horizontal biharmonic viscosity is $B\Delta^3$, with B=0.027~m/s. The Pacanowski and Philander (1981) scheme is used for vertical diffusion, with a background diffusion

of $10^{-4}m^2/s$ for momentum and $10^{-5}m^2/s$ for tracers, with a maximum value set to $10^{-2}m^2/s$. In order to avoid unrealistic shallow mixed layers in summer, an additional vertical diffusivity of 0.01 m^2/s is applied over a depth given by the Monin-Obukhov scheme (Timmermann et al., 2002).

Sea ice

The FESOM sea ice component is a dynamic-thermodynamic sea ice model in which the thermodynamics follow the work of Parkinson and Washington (1979) and the dynamics are represented by the EVP rheology from Hunke and Dukowicz (2001).

Sea ice thermodynamics. The thermodynamics of sea ice in FESOM are based on models by Semtner (1976) and Parkinson and Washington (1979) where the surface heat balance equation is separately solved for the ice and the snow:

$$(1 - \alpha)Q_{SW} + Q_{LW} - \epsilon \sigma T_s^4 + Q_{se} + Q_{la} + Q_c = 0, \tag{4.1}$$

where α is the surface albedo, Q_{SW} the shortwave solar radiation, Q_{LW} the longwave radiation, ϵ the surface emissivity (of ice or snow), σ the Stefan-Boltzmann constant, T_s the surface temperature (of snow or ice), Q_{se} the sensible turbulent heat flux, Q_{la} the latent turbulent heat flux and Q_c the conductive heat flux accross the slab of ice and snow. The latter is expressed as:

$$Q_c = k_i \frac{T_f - T_s}{\widetilde{h_i}},$$

where T_f is the seawater freezing point, k_i the thermal conductivity of ice and \tilde{h}_i the effective thickness. From the 0-layer approach of Semtner (1976), \tilde{h}_i is computed by:

$$\widetilde{h_i} = \frac{1}{a_i^T} \left(\frac{M_i}{\rho_i} + \frac{M_s}{\rho_s} \frac{k_i}{k_s} \right),$$

where M_i and M_s are the ice and snow masses per unit area, respectively, ρ_i and ρ_s their densities, a_i^T the total ice concentration and k_s the snow conductivity. In this configuration, if the surface temperature T_s is greater than the melting point T_m , T_s is set equal to T_m and the extra heat goes to ice/snow melting. The snow thickness changes with precipitation. The ice growth rate which depends strongly on the ice thickness, evolves following the seven-level approximation suggested by Hibler (1979) under assumption of a linear distribution. At the ice base, the balance equation of Lemke (1987) is chosen with an instant conversion of mixed layer heat to ice thickness change.

Sea ice dynamics. The sea ice model simulates the sea ice drift velocity $\vec{u}_{ice} = (u_i, v_i)$ on the same surface mesh as the oceanic one. The two-dimensional momentum equation can be written as follows:

$$M(\partial_t + f\vec{k} \times) \vec{u}_{ice} = a_i^T (\vec{\tau}_{ai} + \vec{\tau}_{oi}) + \vec{F} + M \ g \nabla \eta, \tag{4.2}$$

where f is the Coriolis factor, τ_{ai} and τ_{oi} are the atmospheric and oceanic stresses, respectively, \vec{F} the internal force and g the gravity acceleration on the tilted ocean surface. In this representation, \vec{k} is the unit vector pointing upwards and η is the surface ocean elevation. The mass M is the combination of ice and snow contributions $M = a_i^T(\rho_i \ h_i^T + \rho_s \ h_s^T)$, where h_i^T and h_s^T are the total ice and snow thicknesses, respectively. The divergence of the stress tensor is used to express the internal force: $\vec{F} = \nabla \cdot \sigma$. Sea ice is treated as a non-linear elastic-viscous-plastic fluid (EVP; Hunke and Dukowicz, 2001) and the rheology is solved with an internal time step of 60s. The associated parameters for the EVP formulation are defined as follows: the eccentricity e=2, the empirical constant c=20, the creep limit $\tilde{\Delta}=5\ 10^{-9}s^{-1}$ and $P^* = 15000 N/m^2$, and explained in more details in the Appendix B.1. In order to conserve tracers and have a low dispersion, an explicit second-order Flux Corrected Transport (FCT) advection scheme is preferred to the old backward Euler advection scheme for sea ice transport. In practice, there is a special parameter to control the monotonicity of the FCT algorithms, and no additional diffusivity is required to stabilize it.

The continuity equation for the total ice thickness h_i^T :

$$\frac{\partial h_i^T}{\partial t} + \nabla \cdot (h_i^T \vec{u}_{ice}) = Q_h,$$

is solved with a splitting technique. First, the advection step is realized with the thermodynamic sources/sinks Q_h set to zero. The effects of the thermodynamics are taken into account to update the ice thickness.

Sea ice-ocean coupling in FESOM. The coupling interface between the ice and the ocean uses a flux-averaging method. The heat flux between the ocean and the ice base is described in details in section 4.3.4. Besides, the salinity flux F^S is composed of the part related to the freezing and melting of ice and snow, F_i^S , and another one relative to the open ocean F_w^S which is computed from the evaporation E and precipitation P according to the air temperature T_a as follows:

$$F_w^S = S_o^* \left\{ \begin{array}{ll} P - E & \text{if } T_a \ge 0^{\circ} C \\ (1 - a_i^T)(P - E) & \text{if } T_a < 0^{\circ} C \end{array} \right.$$

with the constant ocean surface salinity $S_o^* = 34.7psu$. Only the thermodynamic changes are considered for the salt flux computation:

$$F_i^S = (S_o^* - S_i^T) \frac{\rho_i}{\rho_w} \frac{\partial h_i^T}{\partial t} + S_o^* \frac{\rho_s}{\rho_w} \frac{\partial h_s}{\partial t},$$

where the total sea ice salinity S_i^T is assumed to be 5psu and the snow salinity is set equal to zero. This total flux is applied to the ocean model and the vertical mixing contributes to its distribution into the mixed layer.

Surface stresses at the ice-ocean interface and in the open water are, respectively, computed as follows:

$$\begin{array}{lcl} \vec{\tau_{io}} & = & \rho_w c_{io}^d | \vec{u}_{ice} - \vec{u}_w | (\vec{u}_{ice} - \vec{u}_w) \\ \vec{\tau_{ao}} & = & \rho_a c_{ao}^d | \vec{u}_{10} | \vec{u}_{10}, \end{array}$$

using the drag coefficients $c_{io}^d=3\cdot 10^{-3}$ and $c_{ao}^d=10^{-3}$. The ocean and 10*m*-wind velocities are written as \vec{u}_w and \vec{u}_{10} , respectively. Finally, the total ocean surface stress is expressed as:

$$\vec{\tau_o} = a_i^T \ \vec{\tau_{io}} + (1 - a_i^T) \ \vec{\tau_{ao}}.$$

4.2.2 LIM3

LIM3 is a C-grid dynamic-thermodynamic sea ice model which includes a representation of the subgrid-scale distribution of ice thickness, enthalpy and salinity, which is initially coupled to the finite difference ocean model (NEMO). Its main features are developed in the paragraphs hereinafter.

Sea ice dynamics. The ice velocity is also determined by the equation 4.2, solved using the C-grid formulation (Bouillon et al., 2009) of the EVP rheology (Hunke and Dukowicz, 1997). 300 sub-iterations are used for ice dynamics with a time step of dt=96s. For ice strength, the formulation of Hibler (1979) is used with $P^*=40000N/m$ which depends on the resolution and configuration of LIM3 (in this case, NEMO.3.1 with a resolution of ORCA2°). The sea ice state variables are then transported using the advection scheme of Prather (1986) which conserves the second-order moments of their spatial distributions. Pratically almost non-diffusive, it is also quite computationally expensive.

Ice thickness distribution. The ice thickness distribution (ITD) in LIM3 follows the formulation of Bitz et al. (2001) and Lipscomb (2001) with 5 thickness categories ($N_c = 5$). For each of them, the ice cover is vertically divided into five layers of sea ice, covered by one of snow. Each thickness category has a mean thickness (h_l , $l \in [1, N_c]$) in the interval $[H_{l-1}, H_l]$, as shown in Figure

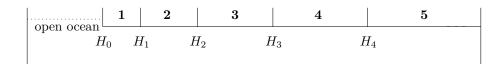


Figure 4.2: Boundaries of the model ice thickness categories.

4.2. This discretization of ice thickness is used for the distribution of the global variables: the sea ice concentration a_i , the sea ice volume per unit area v_i , the sea ice enthalpy per unit area e_i , the salt content smv_i , the snow volume per unit area v_s and the snow enthalpy per unit area e_s .

Mechanical redistribution. Due to ice motion, the ice pack is opened by divergence, and this situation can create areas of open water, whereas the convergence creates thicker ice. Besides, the shear can contribute as to convergence as to divergence following the situation (Kwok and Cunningham, 2002; Tuhkuri and Lensu, 2002). In order to ensure area and volume conservations, the redistribution of sea ice over thickness categories is partly done according to the mechanical deformation of the pack (Thorndike et al., 1975). This mechanism is developed in detail in Section 1.3.

Sea ice thermodynamics. The thermodynamic processes include vertical diffusion of heat in the snow/ice system, snow/ice growth and decay, and creation of new ice in open water. In LIM3, there is no explicit account for lateral melting because it is controlled by floe size (Steele, 1992) as it is implicitly taken into account with the thin ice melting (Bitz et al., 2001). The vertical ice growth and decay rates are determined by the energy conserving model of Bitz and Lipscomb (1999) using the 1D heat diffusion equation. Whereas the solar radiation cannot penetrate into the snow, it is attenuated following Beer's law with an extinction coefficient of 1/m. As in equation (4.1) utilized in the FESOM thermodynamics, the sea ice growth/melt rates are then computed from the imbalance between the different fluxes at the ice interfaces with the atmosphere and the ocean. The boundary conditions are fixed, on the one hand, by the seawater freezing point at the sea ice bottom and, on the other hand, by the surface energy balance. When the surface temperature is equal to T_m , the ice layers successively melt until the available energy of melting is exhausted. Ice grows if the balance between the conductive radiative and ocean heat fluxes at the ice bottom is negative, and melts otherwise. If the seawater surface temperature is equal to T_f , the surface lost heat and new ice can appear. The effects of brine pockets on the heat transfer and storage in ice are taken into account thanks to the formulation of Maykut and Understeiner (1971) and Bitz and Lipscomb (1999). The sea ice thermal properties are then expressed as functions of salinity and temperature. The formation of snow ice, which results from the refreezing of seawater-soaked snow into ice (Fichefet and Maqueda, 1997), occurs, in particular, when the snow is sufficiently thick to depress the snow-ice interface under the sea level so that the seawater floods and refreezes into the snow. This leads to modifications in the salt and heat contents of the sea ice surface layers in the Southern Ocean. Ultimately, the new temperature profile is computed in order to take the thicknesses and salinity changes into account.

Thermodynamical redistribution. After the thermodynamical growth/melt of sea ice is computed, the linear remapping scheme described in Lipscomb (2001) is used to redistribute the ice over the different categories of ice thickness. This second-order semi-Lagrangian scheme, shown to be weakly diffusive and rapidly converging, is valid as long as the ice velocities are not too large. Based on three steps, the category boundaries are first shifted, the thickness distribution is then re-computed on these new categories and, finally, the original boundaries are restored.

Halodynamics. The evolution of the sea ice salt content is determined using parameterizations for brine entrapment and drainage processes (Vancoppenolle et al., 2009a). Gravity drainage prevails in winter, whereas flushing occurs mostly in summer when melting makes sea ice permeable. Moreover, snow ice formation induces the concentration of salt at the ice surface as observed by Jeffries et al. (1997). The evolution of the salinity profile is thus computed from basal ice formation, snow ice formation, gravity drainage and flushing. The salinity in new ice is computed as a function of the sea surface salinity following the formulation of Cox and Weeks (1988). A vertical salinity profile is only considered for thermodynamic computations, while the sole salt content is advected horizontally with the sea ice (Vancoppenolle et al., 2007).

Atmospheric fluxes. Initially, LIM3 uses the atmospheric CLIO forcing combining daily reanalyses of 10m wind velocity and air temperature from NCEP/NCAR (Kalnay et al., 1996) and monthly climatologies of relative humidity (Trenberth et al., 1989), cloud fraction (Berliand and Strokina, 1980) and precipitation (Large and Yeager, 2004). The net solar radiation is then computed as a linear combination of clear and overcast skies contributions with the formulation of Shine (1984). The parameterization of the longwave radiation flux follows Goosse (1997) with a correction factor to take the effects of clouds into account. The turbulent latent and sensible heat fluxes are also computed as in Goosse (1997) where the specific humidity of the air at satura-

 $^{^{1}\}mathrm{The}$ CORE forcing is also an other configuration that can be used sometimes by LIM3.

tion is expressed as a non-linear function of the surface temperature.

Freshwater flux. Using the approach of Tartinville et al. (2001), the freshwater fluxes for the ocean and sea ice follow a special convention: a freshwater flux is computed based on evaporation and precipitation, but all gains or losses of freshwater through ice melting or freezing are treated as a salt flux in the system. With this formalism, the sea ice can be seen as a negative reservoir of salt. The salt is rejected during new ice formation in open water, basal congelation, snow ice formation and melt of salty ice. Then, the freshwater flux at the ocean surface is written as $F_w^S = P - E + R + FM + SE$, where R is the river runoff, FM the flux associated to the freezing and melting of snow ice and SE the flux relative to the salt uptake and release.

4.3 Coupling strategy

As FESOM and LIM3 have not the same data structures, the storage of the sea ice state variables in LIM3 must be first treated as in FESOM. Then, the key components of LIM3 are integrated in FESOM following a specific calling sequence. An overview of those components chosen in each model is provided

Characteristics	FESOM	LIM3
Thermodynamics		×
Halodynamics	NA	×
Dynamics	×	
ITD	NA	×
Mechanical redistribution	NA	×
Thermodynamic redistribution	NA	×
Fluxes/Forcing	×	

Table 4.1: Illustration of the features kept for the coupled model, where NA (Not Available) refers to a missing characteristic in the particular model.

in Table 4.1. In order to complete a successful coupling, the inputs required by LIM3 and the outputs given back to FESOM are also detailed. The last section is devoted to the heat fluxes needed for the balance equation (4.1), which must be consistent with the oceanic component.

4.3.1 Storing sea ice state variables on the FESOM grid

The FESOM surface mesh is constituted of n^E elements and each of them can be identified by a number: $e=1,..,n^e$. Each element is characterized by three nodes, that can also be nodes for other elements. From this discretization, the ice thickness field is expressed as

$$h(x,y) = \sum_{j}^{N^{n}} h_{j}\phi_{j}(x,y),$$

where N^n is the number of nodes, h_j are the nodal values and ϕ_j are the basis functions. Following the same formalism, each variable field has its own nodal values, and these values are ordered by node number in an associated vector for the different computations. This is a major difference with the finite difference method where the variables are directly stored into a 2D matrix and organized according to their longitude and latitude coordinates, respectively.

Global variables	LIM3	FESOM-LIM3	Units
Sea ice concentration Sea ice volume Sea ice enthalpy Sea ice salt content Snow volume Snow enthalpy Total lead fraction	$a_{i}(N_{x}, N_{y}, N_{c}) \\ v_{i}(N_{x}, N_{y}, N_{c}) \\ e_{i}(N_{x}, N_{y}, N_{l}, N_{c}) \\ smv_{i}(N_{x}, N_{y}, N_{c}) \\ v_{s}(N_{x}, N_{y}, N_{c}) \\ e_{s}(N_{x}, N_{y}, N_{c}) \\ ato_{i}(N_{x}, N_{y})$	$a_{i}(N^{n}, N_{c})$ $v_{i}(N^{n}, N_{c})$ $e_{i}(N^{n}, N_{l}, N_{c})$ $smv_{i}(N^{n}, N_{c})$ $v_{s}(N^{n}, N_{c})$ $e_{i}(N^{n}, N_{c})$ $ato_{i}(N^{n})$	

Table 4.2: Transformation of the global variables by the bijective mapping, where N_x and N_y are the dimensions of the matrix along the x and y coordinates of the finite difference grid, and N_c and N_l are the number of categories and layers, respectively.

All components from LIM3, coupled to FESOM, represent processes that are independent from one grid cell to another. LIM3 matrices of dimension N are thus transformed into matrices of dimension N-1, as illustrated in Table 4.2. By this way, a particular position in a LIM3 vector is directly linked to the same particular node in FESOM, as schematized in Figure 4.3. Thanks to this formulation, the source code of LIM3 does not need to be fully modified and a bijective mapping must be applied between the different approaches. Given the non-intuitive correspondence in variables names between FESOM and LIM3, a technical note is provided in Appendix B.2.

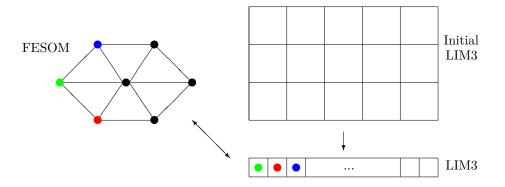


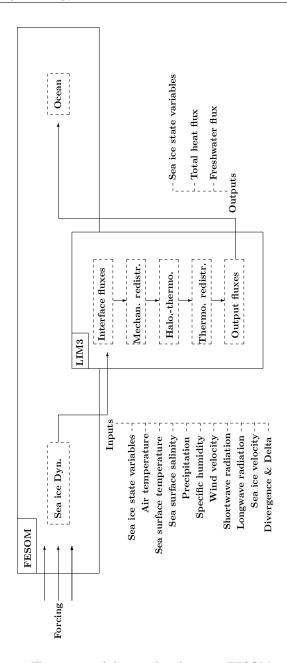
Figure 4.3: Schematic illustration of the coupling of variables between LIM3 and FESOM. An initial matrix from LIM3 is transformed into a vector for the coupling of LIM3. Next, each FESOM node is directly linked to a specific position in this LIM3 vector for all the computations.

4.3.2 Calling sequence

A new interface FESOM-LIM3, illustrated in Figure 4.4, is built in order to exchange the necessary variables between the two models. In practice, FESOM starts by reading the forcing and computing sea ice dynamics. Then, the main call to LIM3 is performed thanks to the interface. For the sake of simplicity, the main source code of LIM3 is conserved but adjusted to remove the call to its dynamic component. Thus, all the processes summarized in Table 4.1 are kept. Before the call of the halo-thermodynamics in LIM3, the mechanical redistribution must be called because the global ice state variables which have been advected by FESOM, have not been updated. All variables are consistently transformed from LIM3 to FESOM by the bijective mapping. After the execution of LIM3, FESOM receives the net freshwater and heat fluxes back, as well as the global ice state variables and their average, which completes the ice ocean time step.

4.3.3 Inputs/Outputs

In addition to the global sea ice state variables that are exchanged between both models, LIM3 requires specific inputs. First, the atmospheric fields are necessary to compute the heat fluxes at the ice or ocean surface: air temperature [K], wind velocity [m/s], specific humidity, solid and liquid precipitations $[kg/m^2/s]$. Then, the sea surface temperature $[^{\circ}C]$ and sea surface salinity [psu] are also required. For the forcing, the shortwave and longwave radiations from



 ${\bf Figure~4.4:~Illustration~of~the~coupling~between~FESOM~and~LIM3}.$

the Coordinated Ocean-ice Reference Experiments data set (COREv2, Large and Yeager, 2008) are directly given to LIM3. The latest variables required especially for the ice redistribution, are the ice velocity [m/s], the friction velocity [m/s] and the divergence ϵ_d and a measure of deformation rate Δ which are computed from the ice rheology of FESOM. With respect to the ice velocity (u_i, u_j) and using the deformation rate of the sea ice cover $\dot{\epsilon}_{ij} = \frac{1}{2} \left(\frac{\partial u_i}{\partial x_j} + \frac{\partial u_j}{\partial x_i} \right)$, the latter variables can be written as:

$$\begin{array}{rcl} \epsilon_d & = & \epsilon_{11} + \epsilon_{22}, \\ \Delta^2 & = & \left(\epsilon_{11}^2 + \epsilon_{22}^2\right) \left(1 + \frac{1}{e^2}\right) + 4 \frac{\epsilon_{12}^2}{e^2} + 2 \epsilon_{11} \epsilon_{22} \left(1 - \frac{1}{e^2}\right). \end{array}$$

All sea ice-related global variables are provided to FESOM at the end of the sea ice time step, as well as the net heat and freshwater fluxes (including the contributions from the ice growth and melt).

4.3.4 Input heat fluxes to LIM3

Heat fluxes	Formulations	Parameterization used
Net shortwave radiation	$(1-\alpha) SW \downarrow$	König-Langlo and Augstein (1994)
Net longwave radiation	$LW \downarrow -\epsilon \sigma T^4$	Stefan-Boltzmann Law
Latent heat flux	$\rho_a L C_E W (q_a - q)$	
Sensible heat flux	$\rho_a L C_H W (T_a - T)$	Parkinson and Washington (1979)
Ocean to ice flux	$\rho_o c_o C_{ht} u^* (T_o - T_f)$	

Table 4.3: Description of the heat fluxes where T[K] refers to the sea ice temperature or to the ocean temperature (T_o) depending on the case, q_a is the specific humidity at 10m, q the specific humidity at the surface (sea ice or ocean), u_i and u_o are the ice and ocean velocity, respectively, C_E and C_H refer to the latent and sensible transfer coefficients, respectively, of the sea ice (constants then) or of the ocean (variables) as the case may be.

All heat flux calculations realized in LIM3 must be consistent with the forcing fields read by FESOM at the beginning of the time step. Those fluxes and their formulations are listed in Table 4.3. The computation of these fluxes is based on the physical variables and parameters described in Table 4.4 and 4.5, respectively. Those fluxes are used in LIM3 to compute the energy balance at the ice interfaces with the atmosphere and the ocean. Following FESOM's

parameterizations, the incident shortwave $(SW\downarrow)$ and longwave $(LW\downarrow)$ radiations are derived from satellite observations. These fluxes include the effects of clouds, decreasing $SW\downarrow$ and increasing $LW\downarrow$. The expressions of the latent and sensible heat transfer coefficients depend on the surface type (ocean or sea ice). In the case of the ocean, the wind and the atmospheric instability are taken into account according to the formula of Large and Yeager (2008), whereas these coefficients are constants for the sea ice. The sea ice albedo used in FESOM does not depend on the sea ice thickness and only takes four different surface state-depending values. As LIM3 uses the Shine and Henderson-Sellers (1985) parameterization which is more complex, the choice of the sea ice albedo will be developed separately in section 4.5.

Variables in the heat flux	Formulations	Units
Surface geostrophic wind speed	$ \vec{W} = \sqrt{u_w^2 + v_w^2}$	[m/s]
Friction velocity	$u^* = \sqrt{Cd_{i,o} \vec{u_i} - \vec{u_o} ^2}$	[m/s]
Atmosphere-ocean drag coefficient	$Cd_{a,o} = \frac{2.7 \ 10^{-3}}{ \vec{W} } + 0.142 \frac{ \vec{W} }{13090}$	
Latent heat transfer coefficient for the ocean	$C_{E,o} = \sqrt{Cd_{a,o}}$	[]
Sensible heat transfer coefficient for the ocean in-situ freezing temperature	$C_{H,o} = 18\sqrt{Cd_{a,o}}$ for $\zeta > 0$ = 32.7 $\sqrt{Cd_{a,o}}$ for $\zeta \leq 0$ $T_f = -0.0575 S + 1.7105 10^{-3} S^{3/2}$ - 2.155 10 ⁻⁴ S^2	[]
Specific humidity	$q = \frac{6.89 \ 640380}{\rho_a} \exp \frac{-5107.4}{T}$	[K] $[kg/kg]$

Table 4.4: Description of the variables used in the heat flux calculations, where S is the salinity of the upper oceanic layer and ζ is the atmospheric stability.

Physical parameters	Symbols	Values	Units
Ocean albedo	α_o	0.1	[]
Emissivity	ϵ	0.97	[]
· ·	-		[]
Stefan-Boltzmann constant	σ	$5.68 \ 10^{-8}$	$[W/(m^2K^4)]$
Air density	$ ho_a$	1.3	$[kg/m^3]$
Reference seawater density	$ ho_o$	1025	$[kg/m^3]$
Snow density	$ ho_s$	290	$[kg/m^3]$
Bare sea ice density	$ ho_i$	910	$[kg/m^3]$
Seawater specific heat	c_o	4190	[]
Heat transfert coefficient	C_{ht}	0.006	[]
Latent heat of vaporization	L	$2.5 \ 10^6$	[J/K]
Latent heat of sublimation	L	$2.834 \ 10^6$	[J/K]
Latent heat transfer coefficient			
for the sea ice	$C_{E,i}$	$1.75 \ 10^{-3}$	[]
Sensible heat transfer coefficient	,		
for the sea ice	$C_{H,i}$	$1.75 \ 10^{-3}$	[]
Ice-ocean drag coefficient	$Cd_{i,o}$	$5.5 \ 10^{-3}$	[]
Ice-atmosphere drag coefficient	$Cd_{i,a}$	$1.32 \ 10^{-3}$	[]

Table 4.5: List of the constant parameters initially defined by FESOM and now used also in LIM3 in order to be consistent with the setup.

4.4 Experimental design

We use a mesh with a resolution that varies with the location: the global ocean has a 1.5° horizontal resolution which increases along the coasts. With the aim of studying the Arctic Ocean, this mesh is also refined to 24km north of 50° , and further to 5km in the Canadian Arctic Archipelago (Figure 4.5). The narrowest locations: Lancaster Sound, Nares Strait and Hell Gate-Cardigan Straits are represented by 11, 6 and 3 grid points, respectively. Fury and Hecla Strait connecting the Canadian Arctic Archipelago and the Fox bassin are closed in the model. There are 55 vertical z-levels of increasing thickness. The IBCAO data (Jakobsson et al., 2008) are used to build the Arctic bathymetry whereas the GEBCO data is taken for other regions. From 64° to 69° , a linear combination of both data is taken (Figure 4.6).

In order to be consistent with respect to heat fluxes in each model, the simulations were initialized in the same way in LIM3 as in FESOM. Initialized in FESOM, the mean temperature and salinity fields from the PHC3 global ocean

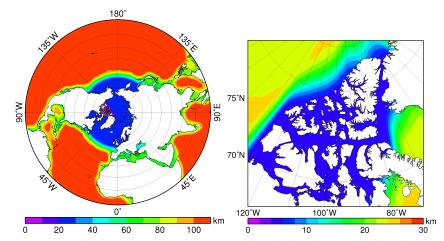


Figure 4.5: Resolution [km] of the global mesh in the Northern Hemisphere (left) and in the Canadian Arctic Archipelago (right) [figures from C. Wekerle (AWI)].

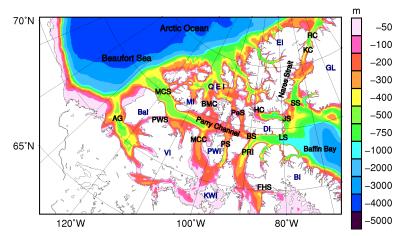


Figure 4.6: Model bathymetry in the Canadian Arctic Archipelago [figure from C. Wekerle (AWI)].

climatology were used (Steele et al., 2001b). In regions with an initial sea surface temperature below -1° C, an initial mean sea ice thickness of 2.0m in the Northern Hemisphere (1.0m in the Southern Hemisphere), ice concentration of 0.95 (0.9) and snow thickness of 0.1m in both areas are prescribed. This initialization allows to yield a sea ice distribution in agreement with the observations.

The COREv2.0 data set (Large and Yeager, 2008), which includes 6 hourly data for 10m specific humidity, 10m air temperature and 10m zonal and meridional wind, as well as monthly data for precipitation and daily date for shortwave and longwave radiations, was taken for the atmospheric forcing. We use a climatology of monthly river runoff from Dai et al. (2009), and a sea surface salinity restoring to the PHC 3.0 climatology with a piston velocity of 10m per 60days. FESOM-LIM3 was integrated over the time period 1970-2007, and the last 29 years are used in the analysis. Monthly mean prognostic variables were saved for this purpose.

4.5 Model tuning

As any sea ice-ocean coupled model, FESOM-LIM3 uses a large range of parameters that are not strictly constrained by physical observations. In order to obtain simulated results that are close to observations, some of these parameters need to be tuned depending on the forcing data. For instance, in Miller et al. (2007), the optimal set of parameter values (cold, thick ice albedo, drag coefficient and P^*) appears to change with the atmospheric forcing data. The sea ice albedo is often the first parameter chosen by modellers to adjust the simulated sea ice thicknesses and concentrations (Hunke, 2010). However, it is also important to maintain albedo near realistic values.

As the surface heat fluxes in FESOM-LIM3 are the same as those used in FESOM, it should make sense to also keep the sea ice albedo that FESOM employs. It depends on the snow presence and on the surface temperature and takes the following values:

0.81 if sea ice is cold and covered by snow,

0.77 if sea ice is melting and covered with snow,

0.70 if sea ice is cold and bare,

0.68 if sea ice is melting and bare.

However, these constant values are not well adapted to the multi-category formalism since a very thin bare ice category has the same albedo as a thick one. In LIM3, the sea ice albedo is parameterized following Shine and Henderson-Sellers (1985), as a function of snow depth, ice thickness and surface temperature, hence a distinct value for each sea ice category. This parameterization which interpolates the albedo between several pivotal values depicted by the solid blue line in Figure 4.7, whereas the plain red line corresponds to the albedo of melting ice. Both maximum values of these albedo parameterizations (0.53 and 0.65, respectively) are quite smaller than those of FESOM. Keeping those values causes the sea ice to melt much faster in summer, and leads to an unrealistically small sea ice extent. Naturally, some other parameter changes

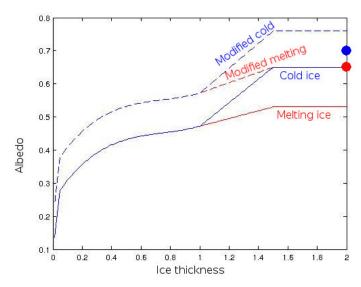


Figure 4.7: Illustration of the modification of the albedo parameterization of Shine and Henderson-Sellers (1985). The blue and red solid lines correspond to the unmodified albedos of the freezing and melting bare ice, respectively. The dashed lines are the modified albedos in order to be in the range of the albedo values initially in FESOM. The two plain circles are the initial contant values of the FESOM parallelization for the freezing (blue) and melting (red) bare ice.

could be investigated in this thesis, but the albedo values usually are the first to be tuned. Two preliminary simulations were performed with the albedo parameterizations of FESOM and of LIM3. Table 4.6 shows the mean value of the sea ice extent and volume in the Northern and Southern Hemispheres for each parameterization. With regards to the observed values, the results with the initial albedo parameterization of LIM3 are too low for the coupled model, but the initial FESOM one does not vary according to the thicknesses and gives thus larger averages. The main differences are seen in the Arctic where the mean values are too large for the simulation α_F and too small for the α_L one, especially for the minima. In the Southern Ocean, the albedo parameterization does not have a big influence. Some other parameters that could be tuned in order to improve the volume results in this area are the boundaries of the ITD or the lead closing parameter. Due to shearing deformation, some open water areas, also called leads, can appear in the ice pack. When convergence forces leads to close, the thin ice is piled up into ridges (Stern et al., 1995). The new ice can then be reordered to a mean thickness referred to as a lead closing parameter. In Timmermann et al. (2005), it appears, as in this simulation with

		N.H.				S.H.		
	Obs/Rea	$lpha_F$	$lpha_L$	$lpha_U$	Obs/Rea	$lpha_F$	$lpha_L$	$lpha_U$
Extent								
Mean	11.94	13.05^{-}	11.89	$\bar{1}\bar{2}.\bar{2}\bar{1}$	11.93	10.10^{-}	-9.96	9.96
Max	15.58	16.89	16.61	16.66	18.76	19.45	19.42	19.33
Min	6.54	8.45	4.37	5.79	3.01	0.18	0.07	0.08
Volume								
Mean	-23.51	28.08	$18.\overline{5}6$	20.58	6.35	4.34	-4.15	-4.15
Max	31.04	37.41	29.43	31.10	9.96	9.34	9.20	9.12
Min	15.04	19.01	7.87	10.08	1.92	0.22	0.10	0.12

Table 4.6: Overview of the simulated sea ice extent $[10^6km^2]$ and volume $[10^3km^3]$ with the different albedo parameterizations in FESOM-LIM3, where α_F refers to the simulation with the initial albedo of FESOM, α_L to the initial albedo in LIM3 (Shine and Henderson-Sellers, 1985) and α_U to the adjusted one. All diagnostics are computed with respect to the mean seasonal cycles. The observed values (Obs) were retrieved from the National Snow and Ice Data Center (NSIDC) sea ice index (Fetterer et al., 2012) for the extent, the PIOMAS reanalyses (Rea) (Schweiger et al., 2011) for sea ice volume in the Northern Hemisphere (N.H.) and the reanalyses (Rea) from Massonnet et al. (2013) for sea ice volume in the Southern Hemisphere (S.H.).

FESOM-LIM3, that a small lead closing parameter leads to an underestimation of the sea ice thickness, especially in the S.H. However, in this coupled model, a better estimation of this parameter should maybe require two distinct values because a larger value than 0.1[m] could be appropriate for the Antarctic, but this increasing would also lead to too much Arctic ice. In order to keep satisfactory results in both hemispheres and because Antarctic sea ice is not the focus of this study, the single initial value for the lead closing parameter is prime kept. Besides, defining new boundaries for the ice thickness distribution in the S.H. may also be a solution of this problem. Indeed, the maximum observed sea ice thickness in this area is only about 3m, whereas the fifth category begins at 3.8m. This category is thus never filled in the simulations of Antarctic sea ice. Finding better boundary values for the ITD in the Southern Ocean is then a path of investigations that should also be explored. In order to reduce the errors, the pivotal values in the parameterization of Shine and Henderson-Sellers (1985) were increased to get the final albedo in the same range of the FESOM values (Table 4.6). This modified albedo was chosen for all other simulations and analyses with FESOM-LIM3. Some other parameters could be adapted in further studies.

4.6 Concluding remarks

The advantages of coupling LIM3 to FESOM are manifold. LIM3, so far used in models utilizing the finite difference formalism, already provides satisfactory results but suffers from the coarse definition of coastlines in some regions. Using FESOM instead allows to refine among others the coasts of the Canadian Arctic Archipelago. On the other hand, the thermodynamics of sea ice in FESOM remain relatively simple. LIM3 offers the possibility of representing the subgridscale distribution of ice thickness thanks to the multi-category formalism and includes a state-of-the-art representation of the sea ice halo-thermodynamics. This new coupled model FESOM-LIM3 hence brings together the advantages of each model. The coupling of both models was performed and required some technical adaptations with regard to the fluxes at the interfaces: the parameterizations of the shortwave and longwave radiation, the sensible and latent heat fluxes, as well as the ocean to ice heat flux. Moreover, an adjustment of the albedo values was also necessary in order to get a realistic mean sea ice cover over the period 1979 - 2007. The preliminary analysis of the model with the new albedo provides satisfactory results with respect to the sea ice mean state. A comprehensive evaluation of the model is now required, as well as the study of the physical impacts of LIM3's most important features on the model outputs in regions where its capabilities were never properly assessed due to the limiting resolution and coastline definition.

CHAPTER

Assessment of the coupled model FESOM-LIM3

Summary

Numerous sea ice-ocean estimates from FESOM-LIM3 are compared with various observational datasets, first at the hemispheric scale and then in particular coastal regions. The model yields mean seasonal cycles and geographical distributions of ice concentration and velocity that are in relatively good agreement with observations. In the Southern Ocean though, contrary to the Arctic, the ice thickness is clearly underestimated everywhere by 40% in summer and by more than 50% in winter. This feature, discussed in detail in the previous chapter, could be due to some parameters that are not well-adapted for this hemisphere, such as to low a lead closing parameter, or unadapted boundaries in the ice thickness distribution. The sea ice seasonal evolution is also analyzed in the Canadian Arctic Archipelago, in the main gates of the Arctic Ocean (Davis, Fram and Bering Straits as well as the Barents Sea Opening) and in the Weddell sea. The overall growth and decay of sea ice, as well as the solid freshwater fluxes, are simulated realistically in all those regions, except the Bering Strait. In the Northern Hemisphere, FESOM-LIM3 is found to be appropriate for large-scale sea ice and climate simulations while in the Southern Hemisphere, some adjustments deserve to be studied in more details.

5.1 Introduction

In the previous chapter, FESOM and LIM3 have been coupled together in order to take the advantages of each model. The use of an unstructured mesh in FESOM allows for a higher and adaptative resolution and well-defined coastlines. On the other hand, LIM3 brings a state-of-the-art representation of the sea ice halo-thermodynamics and the subgrid-scale distribution of the ice thickness thanks to the multi-category formalism. After an adjustment of the heat fluxes and a calibration (see Chapter 4), the model must be evaluated by means of some observational datasets or reanalyses.

In the next section, a global evaluation of the new coupled model FESOM-LIM3 is performed. The purpose is to document the model behaviour, in particular the improvements due to the combination of the refined resolution at high latitudes with the key components of LIM3. A simulation over the period 1970 – 2007 has been conducted with FESOM-LIM3 and the results over the period 1979 – 2007 are discussed. The ice areal coverage is investigated, as well as the sea ice thickness and velocity. In the following section, analyses are performed to assess the capabilities of the new model at the regional scale. The seasonal evolution of ice concentration in the Canadian Arctic Archipelago highlights realistic regional features during the sea ice growth and melt periods. In the Arctic, the simulated exports through the main gates give results in general agreement with the available observations. Finally, in the Weddell Sea, the modelled ice thicknesses in particular locations are studied and compared to observations from upward looking sonars.

5.2 Global evaluation of FESOM-LIM3

The model has been run over the period 1970-2007, but the studied period is 1979-2007 in order to skip the model spin up phase. In this section, we discuss the simulated general sea ice physical state variables: the ice areal coverage and volume in the Northern Hemisphere (N.H.) and in the Southern Hemisphere (S.H.), as well as the ice velocity. The model results are compared with available observations from different sources. For the sea ice extent, the observations are taken from the National Snow and Ice Data Center (NSIDC) sea ice index (Fetterer et al., 2012). Initially interpolated on a polar stereographic 25km-resolution grid, they are provided as monthly values. Sea ice volume cannot be observed directly and continuously. In situ measurements through autonomous submarines or moorings provide observations limited in time and space, and satellite observations still suffer from large uncertainties. For instance, the estimated errors can reach 0.7m in the IceSat datasets (Kwok and Cunningham, 2008). In a few cases, the observations are assimilated into numerical models. In order to estimate the sea ice volume in the N.H., the Pan-Arctic Ice

Ocean Modelling and Assimilation System (PIOMAS, Schweiger et al. (2011)) outputs are used. This Arctic sea ice reanalysis is obtained by assimilation of sea ice concentration and sea surface temperature data into an ocean-sea ice model. For the S.H., we use sea ice volume estimates from the model of Massonnet et al. (2013) assimilating ice concentration data using an ensemble Kalman filter. The latter sea ice volume products are hereinafter referred to as reanalyses. Through this chapter, some indicative comparisons are also made with the initial sea ice-ocean model FESOM, which has run over the same period and under the same conditions (forcing, mesh, constant parameters) as FESOM-LIM3. However, no systematic comparison has been made since the comparison of the results between FESOM and FESOM-LIM3 is not necessarily meaningful. While comparing FESOM-LIM3 to FESOM, we sometimes refer to the NEMO model when the sea ice model LIM2 has been changed for LIM3 (Massonnet et al., 2011). The latter transition also concerns the improvement of an initial simple representation (3-layer Semtner model and VP rheology) of the sea ice physics towards LIM3 (version 3.1).

5.2.1 Ice areal coverage

In this section, the simulated mean seasonal cycle and interannual variations of the global hemispheric ice extent as well as the modelled geographical distribution of ice concentration are discussed in both the N.H. and S.H.

Mean seasonal cycle

Averaged over 1979 – 2007, the modelled mean seasonal cycle (Figure 5.1) of sea ice extent in the N.H. follows the cycles derived from the satellite observations (NSIDC) and the reanalyses. In summer, the simulated minimum extent appears somewhat underestimated $(5.79 \times 10^6 km^2)$ whereas it was largely overestimated in the FESOM simulation $(8.8 \times 10^6 km^2)$. The maximum value in winter is overestimated by $10^6 km^2$, as in the FESOM simulation. In this hemisphere, the areal decay is faster than observed, whereas the growth seems realistic. Somehow similarly, NEMO-LIM3 coutperformed NEMO-LIM2 in simulating the mean seasonal cycle of ice extent, as NEMO-LIM2 overestimated the ice extent, especially in summer. In the S.H., the simulated maximum ice extent differs from the observations by only $0.5 \times 10^6 km^2$ (also as in the FESOM simulation). However, the minimum value is strongly underestimated since almost no ice remains. In the FESOM simulation, the winter sea ice which persists with a minimum at $1.2 \times 10^6 km^2$ is not so much underestimated as in FESOM-LIM3, but is significantly different from the observed value. The time of the winter maximum ice extent is realistically reproduced, as well as the time of the summer minimum one.

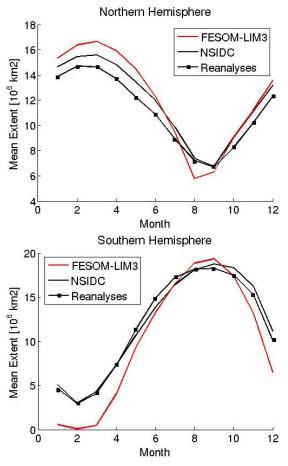


Figure 5.1: Mean seasonal cycles over the period 1979-2007 of N.H. (top) and S.H. (bottom) sea ice extents in the FESOM-LIM3 simulation (red) and in observations derived from satellite measurements (NSIDC) and reanalyses from Massonnet et al. (2013).

Spatial distribution

Maps of simulated and observed sea ice concentrations give further insight into the strengths and weaknesses of FESOM-LIM3. Even if there are notable regional errors, the model generally simulates the position of the ice edge properly and the spatial distribution of ice concentration is in reasonable agreement with the observations. Note that these data must be considered with caution because they can present some significant errors. For example, the melt pond effects, which influence the observations of ice concentration, lead to large uncertainties in summer (Comiso, 2007). During summer melt and freeze-up in the fall, the area deduced by the observations may be underestimated by $1.5 \times 10^6 km^2$, and the estimated error is around $0.5 \times 10^6 km^2$ in winter.

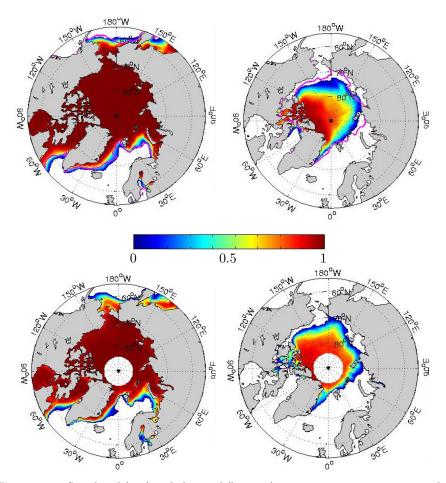


Figure 5.2: Simulated (top) and observed (bottom) mean ice concentrations over the period 1979-2007 for March (left) and September (right), indicating the minimum and maximum ice coverages in the Arctic. The ice edge (purple) on the top panels indicates the 15% ice concentration contour of the observed fields derived from the satellite datasets (NSIDC).

For the Arctic summer (Figure 5.2), the widths of the Siberian and Kara-Sea open area waters in summer are largely overestimated, as well as the open

water area north of Alaska, as opposed to the FESOM simulation where the sea ice was really close to coasts and did not melt enough especially in the Hudson Bay. These open area waters explain the overall underestimation of the summer Arctic ice extent in FESOM-LIM3. However, the observed ice retreat in the Laptev Sea is well reproduced, as well as between the Kara Sea and Spitsbergen. The simulated ice concentration decreases, as expected, towards lower latitudes and in the same sharp way as in observations. Finally, only

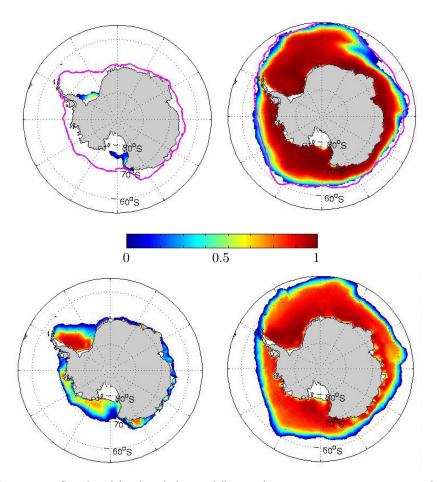


Figure 5.3: Simulated (top) and observed (bottom) mean ice concentrations over the period 1979-2007 for March (left) and September (right), indicating the minimum and maximum ice coverages in the Antarctic. The ice edge (purple) on the top panels indicates the 15% ice concentration contour of the observed fields derived from the satellite datasets (NSIDC).

a small sea ice cover subsists in the northern Baffin Bay and in the southern Canadian Arctic Archipelago. In winter, the model overestimates the ice extent in the Labrador, Greenland and Okhotsk Seas. The Odden Ice Tongue is not visible but sea ice is present in this region. The simulated width of the ice stream along the east coast of Greenland is a little overestimated and extends too much eastwards in the Denmark Strait. The sharpness of ice edge is well represented by FESOM-LIM3, whereas it was too smooth in FESOM.

In the Antarctic (Figure 5.3), the simulated sea ice distribution in summer features a lack of sea ice along most of the Antarctic coasts. Sea ice only persists in the Weddell Sea, contrary to FESOM where sea ice was present in the Ross and Amundsen seas. In winter, the simulated ice is mainly controlled by the westerly winds and the position of the Antarctic Circumpolar Current. The location of the ice edge in the various sectors of the Southern Ocean is realistically simulated, except in the eastern Ross and Enderby Seas where it is slightly too far southwards. Overall, the model ice concentrations within the pack are overestimated compared to the satellite observations (NSIDC), as in FESOM.

Arctic sea ice extent in September 2007

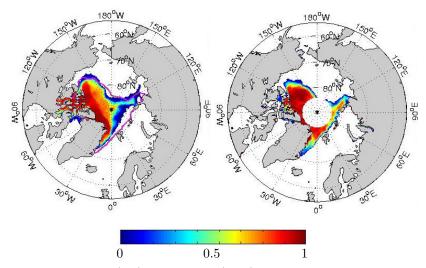


Figure 5.4: Simulated (left) and observed (right) sea ice concentrations for September 2007 where the ice edge (purple) on the left panel indicates the 15% ice concentration contour of the observed fields, derived from satellite datasets (NSIDC).

Since 1953, the Arctic sea ice extent at the end of the summer melt season is declining (Stroeve et al., 2012). In 2007, it reached a particularly low level since satellite observations began. The simulated spatial distribution of sea ice concentration in September 2007 is compared to the satellite observations (NSIDC) in Figure 5.4. FESOM-LIM3 reproduces the main feature of this particular event. The simulated ice edge is close to the observed one on the western side, but sea ice does not sufficiently extend on the eastern side. As previously, FESOM-LIM3 tends to have too much ice in the southern Canadian Arctic Archipelago, but less than in the FESOM simulation. Moreover, there also was too much ice towards the East Siberian and Chukchi seas in FESOM.

Interannual variations

Considering the model annual mean ice extent, a trend in the Arctic of -7.79%per decade is found for the full 1979 - 2007 period, which is faster than for the satellite measurements (NSIDC), suggesting a decline of -5.12% per decade. In the S.H., a negative trend of -1.39% per decade is also simulated, while the trend is positive in satellite observations (0.81% per decade). Time series of monthly anomalies of ice extent (Figure 5.5) indicate that FESOM-LIM3 captures reasonably well the ice extent variability. The correlation between the model and observations reaches 0.87 in Arctic. Fluctuations of Arctic ice extent occurring on a month-to-month time scale are not always reproduced correctly but some particular events happen at the right times. For instance, the large growth in 1997 and the melting during the summer 2007 are well simulated. Besides, the standard deviation derived from the model outputs (0.82) is quite larger than the one from the observations (0.55). This overestimation of the internnual variability was also noticed in NEMO-LIM3 in comparison to NEMO-LIM2 (Massonnet et al., 2011). In the S.H., the simulated anomaly variations are larger than in the Arctic and differ from the anomalies of the observations more significantly. Indeed, the correlation between the model and observations is low (0.22). But, the respective standard deviations are closer, with 0.59 for the model and 0.42 for the observations. Some unusually low ice extents in the austral winters 1979/1980, 1986/1987 and 1996/1997 are well reproduced, but there is an unexpected larger low ice extent in 2006/2007 which is not noticed in the satellite data (NSIDC). The latter feature may be due to an inappropriate response to the atmospheric forcing fields. Compared to the observed minima and maxima, the model often represents these events with a shift of one or two months.

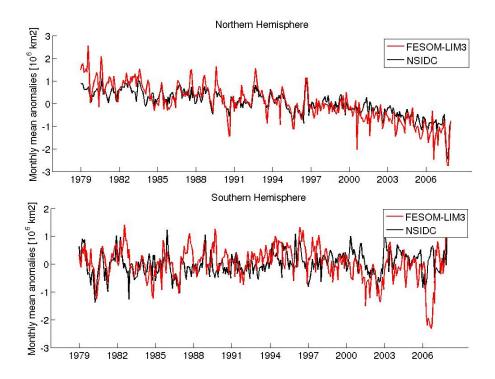


Figure 5.5: Times series of monthly mean anomalies (i.e. differences of individual monthly means from the mean seasonal cycle, which corresponds to the monthly means over the 1979-2007 period.) of sea ice extent $[10^6km^2]$ for the N.H. (top) and S.H. (bottom) as simulated by FESOM-LIM3 (blue) and from the satellite observations (NSIDC, black).

5.2.2 Ice thickness and volume

Mean seasonal cycle

Figure 5.6 shows the simulated mean seasonal cycles of sea ice volume compared to reanalyses through 1979-2007. In the N.H., the simulated cycle has a larger amplitude than those from PIOMAS and the reanalyses from Massonnet et al. (2013). In summer, the simulated minimum volume is underestimated, with a value of $10.08 \times 10^3 km^3$, against $15.04 \times 10^3 km^3$ for PIOMAS, but the maximum value in winter is particularly well estimated with a difference of only $0.06 \times 10^3 km^3$ compared to the PIOMAS data. The summer melting in this hemisphere is faster than observed and due to the thickness-growth feedback, the thinner ice tends to grow also faster. The seasonal cycle of FESOM-LIM3 is quite better than those of FESOM since it overestimated the whole observed

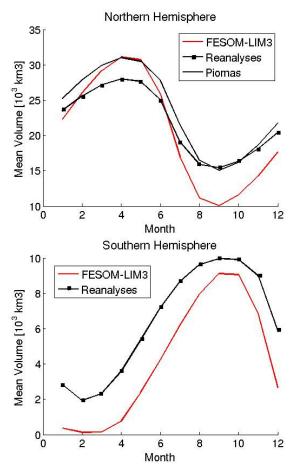


Figure 5.6: Mean seasonal cycles of N.H. (top) and S.H. (bottom) sea ice volume over the period 1979-2007 in FESOM-LIM3 (red) and in reanalyses from PIOMAS and Massonnet et al. (2013) (referred to as *reanalyses* from Massonnet et al. (2013) in this figure).

cycle by at least $10 \times 10^3 km^3$. For the S.H., FESOM well reproduced the minimum mean volume but largely overestimated the maximum with $16 \times 10^3 km^3$. In FESOM-LIM3, the biases are consistent with those in extent: the sea ice volume underestimation is particularly pronounced during the austral summer where the difference between the model and observations is around $1.80 \times 10^3 km^3$. In austral winter, this difference is smaller by $0.80 \times 10^3 km^3$. The times of the ice volume extrema are realistically reproduced.

Ice thickness

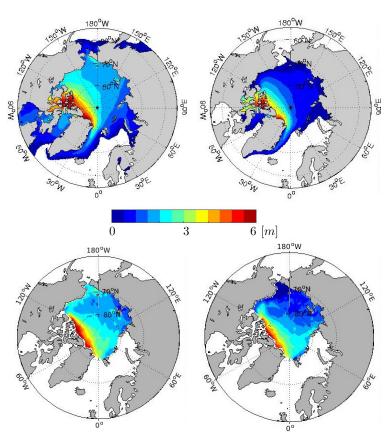


Figure 5.7: Simulated (top) and observed (bottom) spring (left) and autumn (right) sea ice thicknesses [m] in the N.H. over the period 2003-2007. Modelled ice thicknesses are displayed for spring and autumn (mean values for February-March and October-November, respectively) and compared to the IceSat observations (Kwok et al., 2009), in which sea ice has only been detected inside the Arctic basin. Some satellite data are then missing in the other regions.

The spring and autumn sea ice thicknesses derived from the IceSat satellite data by Kwok et al. (2009) are used here to evaluate the model results (Figure 5.7). A qualitative comparison of the modelled spring sea ice thicknesses with the observations shows a general agreement. Sea ice thickness decreases from 5-6m off the north coast of Greenland and the Canadian Arctic Archipelago to 3.5m at the North Pole, and 0-2m on the Siberian shelf. In FESOM, this progressive decreasing in ice thickness was not as well described and an ice

thickness of 9m remained at the northern Canadian Arctic Archipelago over the seasons. In the seasonal ice zone, ice thickness in FESOM-LIM3 does not exceed 1.5m in winter. The thickness gradient between the Siberian shelf and Greenland is also well captured. In autumn, sea ice has a smaller thickness in the center of the northern Canadian Arctic Archipelago than observed, and the thickness between Greenland and the Laptev sea is underestimated by about 2m.

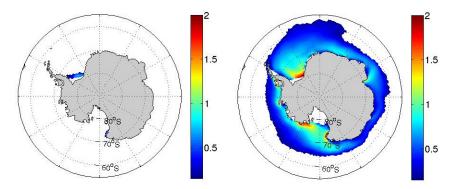


Figure 5.8: Simulated mean sea ice thicknesses [m] in March (left) and September (right) in the S.H. over the period 1979 - 2007.

The simulated austral winter sea ice thicknesses (Figure 5.8) feature ice values between 0.75 to 1.5m in the Weddell Sea, with a maximum of 2.0m at the Filchner Ice Shelf edge. Some thinner areas, maybe polynyas, appear along the east coast of East Antarctica and in the Ross Sea. A area of thicker ice extends from the Amundsen Sea into the Ross Sea. These characteristics show an overall underestimation of 1m everywhere compared to observations (Worby et al., 2008), whereas FESOM was in reasonable agreement with them and NEMO-LIM2 showed an overestimation of the thickness in the Weddell Sea. In the FESOM simulation, the sea ice thicknesses extended from 1m to 3m in the Ross and Weddell Seas in September and had a maximum value of 2m in March in the Weddell sea, which are more realistic than FESOM-LIM3. In March, the thickness simulated by FESOM-LIM3 does not exceed 0.7m in the Weddell Sea and is very thin in other places. This very low ice feature of FESOM-LIM3 will be discussed below. As in NEMO-LIM3 vs NEMO-LIM2 studies, the representation of ice thickness is better reproduced in the N.H.

Ice thickness distribution

The annual cycle of the ice thickness distribution (ITD) averaged above the Ellesmere Island $(80-85^{\circ}N$ and $75-105^{\circ}W)$ is represented in Figure 5.9, where each category of sea ice concentration is illustrated. The sea ice growth is most important in October, resulting in a substantial increase in thin ice area. The ice continues to form throughout the fall and winter, filling in the thicker ice categories until the spring. The thickest ice category remains nearly

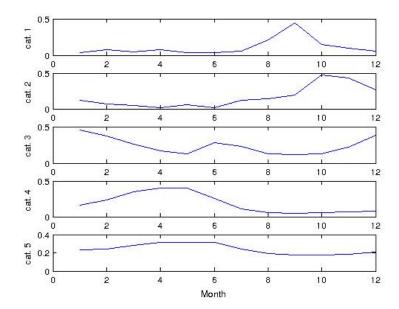


Figure 5.9: Annual cycle of the ice thickness distribution simulated by FESOM-LIM3 above the Ellesmere Island $(80 - 85^{\circ}N)$ and $75 - 105^{\circ}W$ in 2007, where the fractional coverage in each ice category (cat.#) is shown.

constant throughout the year and represents 10% of the areal coverage. Qualitatively, the annual cycle of the ITD simulated by FESOM-LIM3 reflects well the main sea ice features in this area.

In order to evaluate the ice thickness distributions simulated by FESOM-LIM3, the datasets from Operation IceBridge (Kurtz et al., 2013) are used. These observations are provided thanks to airborne remote sensing platforms which measure a wide variety of sea ice properties (sea ice thickness, free-board, snow depth,...) over the period 2009 - 2012. The spatial coverage extends from -165° to 15° in longitude and from 80° to 90° in latitude. For

the comparison, only the mesh nodes of FESOM-LIM3 located in this area are used and even if the time period chosen (2003-2007) is earlier than the one observed since no forcing data COREv2 is available for these last years (2008, 2009, 2010, 2011, 2012), they are even though quite close. The simulated ITDs show in Figure 5.10 an underestimation in both months of all ice thick-

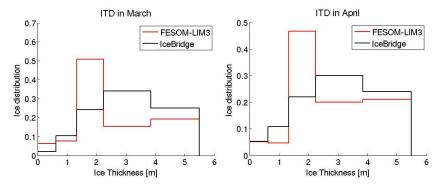


Figure 5.10: Simulated (black) and observed (red) ice thickness distributions in March (left) and April (right) with bounds in sea ice thickness fixed to those from the ITD in FESOM-LIM3. The observations from the IceBridge flights concern the period 2009 - 2012 whereas the FESOM-LIM3 results are averaged over the period 2003 - 2007.

nesses, except for the middle one where there is a large overestimation of more than 50%. In March, the distribution in the first simulated category is also overestimated by 50% but the second one is in good agreement with the Ice-Bridge observations, as well as the last one. The amount of ice in the 4th category is underestimated by 50%. In April, the sea ice thicknesses are well distributed in the first and last categories, and overestimated in the second and fourth ones by 30%.

5.2.3 Ice velocity

The simulated sea ice drifts in the N.H. and S.H. reflect the general patterns of the atmospheric circulation. In the Arctic, the two main circulation features, i.e., the Beaufort Gyre and the Transpolar ice Drift, are captured by FESOM-LIM3 (see Figure 5.11). Sea ice which drifts along the eastern Greenland coasts is notably fast, with an ice velocity around 20cm/s. The particularly large ice drift in Fram Strait was also noticed in NEMO-LIM3 and the grid formulation was suggested by Massonnet et al. (2011) as possible reason. However, higher drifts compensate for thinner ice north of Fram Strait. In FESOM-LIM3, the mean ice drift FESOM-LIM3 highlights the divergent motion over the Siberian

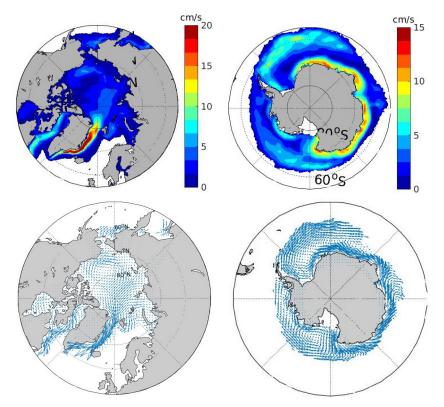


Figure 5.11: Simulated annual mean ice velocity distribution (top) in the N.H. (left) and S.H. (right), and their associated vector fields (bottom) over the period 1979 - 2007.

shelf and the Canadian Arctic Archipelago is a nearly motionless ice zone.

In the S.H., the strong westward drift adjacent to the coast of Antarctica (around 10cm/s) and the offshore circulation (around 5cm/s) are well represented by FESOM-LIM3 (see Figure 5.11). These patterns are similar to those shown by Schmitt et al. (2004). Moreover, the Weddell and Ross Gyres are captured by the model, with drift speeds of 5-10cm/s. These motions are in agreement with observations, although maxima of ice velocity are observed in the Indian and West Pacific sectors of the Southern Ocean, where satellite data show on the contrary an ice cover nearly at rest there (Fedotov et al., 2013). Finally, the position of the transition zone between coastal and offshore ice currents is well located, between 65° and $70^{\circ}S$.

5.2.4 Discussion

In this section, we discuss some hypotheses about the external factors and physical mechanisms that could be responsible for the previously described differences between model and observations. As for NEMO-LIM3, the role of the halo-thermodynamics remains quite difficult to quantify in the simulations since numerous processes are involved.

Lead closing parameter. In the S.H., the lead closing parameter, also called the initial ice thickness (0.1[m]), which we chose not to tune (initial value of NEMO-LIM3), has a strong influence on the new ice formation. As a reminder, open water areas that appear in the ice pack due to ice divergence and shearing deformation are called leads. When convergence forces leads to close, the thin ice formed in these leads is piled up into ridges and reordered to a mean thickness referred to as a lead closing parameter. A low value for this parameter leads to thin new ice by the end of winter which will quicker disappears in summer than a thicker one, and the thick multi-year ice cover is then more difficult to keep. After several tests performed to check this dependency, the intense melting in Antarctic seems due, in part, to the low value of the lead closing parameter. However, it was kept as it is because it is well-adapted for the N.H., it allows a stable simulation with a quick spin-up phase and it proved its efficiency in NEMO-LIM3. Moreover, this initial ice thickness must stay below the low boundary of the second category ([0.6m]), otherwise the ITD becomes meaningless since the new ice will be directly transferred to the second category. This parameter is thus to handle with care. The creation of a double lead closing parameter which would allocate a different value for each hemisphere would require further investigations in order to find the suitable values and check if there is not another parameter that could induce this ice underestimation.

Oceanic convection. Sea ice formation and ocean mixed layer are strongly linked in the Southern Ocean. The brine released when sea ice forms induces a large variation between seawater and sea ice salinities, which may lead to convective mixing. This intense vertical mixing mainly occurs during winter with a local maximum mixed layer depth above 500m in the Weddell sea (Barthélemy et al., 2015). Besides, the mixed layer also influences the sea ice energy balance since it modifies the ocean heat flux at the base of the ice layer or at the ocean surface. If too much warm deep waters are moved at the surface due to the oceanic convection, the sea surface temperature could prevent the sea ice formation or to avoid to keep the multi-year ice in the expected areas (Weddell sea, Ross sea and shelves). The mixed layer depth in September simulated by FESOM-LIM3, shown in Figure 5.12 (left), is in good agreement with respect to other recent modeling studies (e.g., Petty et al., 2014; Holland et al., 2014;

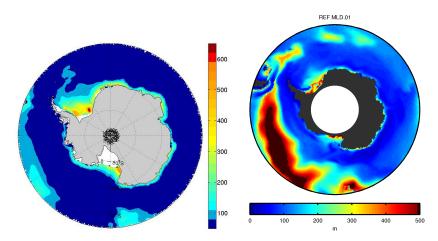


Figure 5.12: Simulated mixed layer depth [m] averaged for September by FESOM-LIM3 (left) over the period 1979 – 2007 and by NEMO-LIM3 (right,Barthélemy et al. (2015)) over the period 1983 – 2005.

Barthélemy et al., 2015)(right Figure 5.12). In the Ross and Weddell seas, the mixed layer is particularly deep (600m) and over some local continental shelves, it exceeds 200m whereas it is low in the Bellingshausen and Amundsen seas. In March, the overall mixed layer depth is quite smaller (30-70m), as expected. These characteristics are similar with other modeling studies (Holland et al., 2014; Petty et al., 2014) and do not suggest an ocean anomaly in FESOM-LIM3 that could lead to the underestimation of the sea ice thickness in March. The sea surface salinities simulated by FESOM-LIM3 do not reveal any singularity in March or September with values around 33-34psu.

ITD. A major advance in the coupled model FESOM-LIM3 is the introduction of an ice thickness distribution (ITD). With the ITD formalism, thin ice disappears faster in early summer in the marginal ice zones, which leads to a lower ice concentration. More shortwave radiation is then absorbed in the ocean, and the processes finally increase the ice bottom melt as well as the freezing in autumn-winter. This partially explains the large amplitude of the seasonal cycles. As NEMO-LIM3, FESOM-LIM3 seems to be more responsive than with its former sea ice model version to atmospheric forcing due to the inclusion of the ITD. In the annual cycle of the ITD above the Ellesmere Island, the seasonal changes through the ice categories highlights the growth and melt phases in FESOM-LIM3. The comparisons of ITDs with the IceBridge observations show that the simulated ice is thinner than observed since the distribution in the third category is larger than the fourth one, whereas the fourth

category in the observations is the larger in March and April. The ice distribution is then mainly shifted towards the thinner categories, as in the studies of Massonnet et al. (2011), in which the contribution of the first category is the largest or, Vancoppenolle et al. (2009b), in which the largest proportion of ice is often found in the second category. However, the thicker categories (4 and 5) are in good agreement with observations, whereas this feature was not found in the work of Lecomte et al. (2013). The lack of precision in the simulated ITDs could be due to some uncertainties related to the IceBridge observations, which can reach values of around 0.5 - 1.5m, and this kind of range can easily shift ice thickness from a category to another one. These errors vary with respect to the sensors and to the constant approximations of variable parameters used to compute the ice thickness. Besides, the boundaries defined for the ITD are the same for the N.H. and the S.H., whereas the maximum ice thicknesses in both hemispheres are quite different: around 9m for the N.H. and about 3m for the S.H. This choice means that the fifth category is never filled for Antarctic sea ice and the ITD is not optimal in this area. An adjustment of these boundaries for the S.H. probably may deserve further investigations.

Forcings. In the model, sea ice in the northern Canadian Arctic Archipelago does not melt sufficiently in summer. This problem arises because there is a negative bias in the shortwave radiation of COREv2 forcing fields in this area. Moreover, as this data set is based on the NCEP reanalyses, the warm bias in the NCEP temperatures in summer (Hunke and Holland, 2007) may also be responsible for the complete retreat of the sea ice in the northeastern Kara Sea and off the Siberian and Alaskan coasts. In the S.H., the overall underestimation of ice thickness can be related to the poor representation of the atmospheric forcing fields (Windmuller, 1997), and near the tip of the Antarctica Peninsula, a warm bias is also found in the NCEP-NCAR surface air temperatures.

Average. In the N.H., the Odden/Nordbukta ice tongue is not sufficiently developed in the simulated geographical distribution of mean winter ice concentration. However, the number of mesh cells should be sufficiently large to support the hypothesized mechanisms for its formation (e.g., cold air outbursts, instabilities of the East Greenland Current, Comiso et al., 2001). From the satellite observations, it appears that the ice tongue has a large interannual variability in the size, location and even persistence, mainly due to the deepocean convection that also varies from year to year in this area (Shuchman et al., 1998). From this perspective, it appears that the averaging of the model results over the 1979-2007 period masks out the location of the ice tongue that varies a lot on internnual time scales. For this reason, it is interesting to notice for instance that the Odden/Nordbukta ice tongue is simulated by FESOM-LIM3 in March 1997, as illustrated in Figure 5.13. Besides, some important processes in the shelf regions are misrepresented because the summer

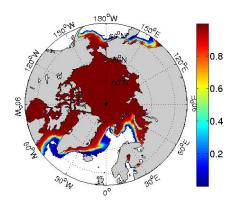


Figure 5.13: Simulated Arctic ice concentrations in March 1997, highlighting the Odden/Nordbukta ice tongue.

ice retreat is too important in the East Siberian Sea. In the S.H., the underestimation of ice cover could also be due to the absence of ocean waves and tides component. Indeed, the surface waves break the ice pack into numerous ice floes, which directly affect the exchanges between the ocean, the atmosphere and the ice. Tidal currents add a highly variable stress force at the ice-ocean interface. Because of the speed up of their retreats, they tends to reduce the expansion of the ice cover (Koentopp et al., 2005).

5.3 Sea ice seasonal variability in coastal regions

After this first standard evaluation, some specific analyses are now performed on the sea ice variability in the Canadian Arctic Archipelago, the main gates of the Arctic Ocean and the Weddell Sea. With the local mesh refinement in the Arctic, the geometry of the Canadian Arctic Archipelago is very realistic in the model and the sea ice evaluation can thus be conducted there with details. The exports in the main gates of Arctic: Bering, Davis, Fram Straits and the southern Barents sea, are also investigated. In this subsection, the mean ocean volume flux and solid freshwater exports are investigated, as well as the seasonal variation of these same fluxes. As the resolution around the Antarctica is also rather fine, the last study concerns the ice draft at some particular locations in this area which are compared through time series with the datasets obtained from the upwards looking sonars.

5.3.1 Canadian Arctic Archipelago

The Canadian Arctic Archipelago (CAA) is a region of particular interest because of it makes the link between the Arctic and Atlantic Oceans. Its narrow straits and shallowness (see Figure 5.14) also constitute a challenge for numer-

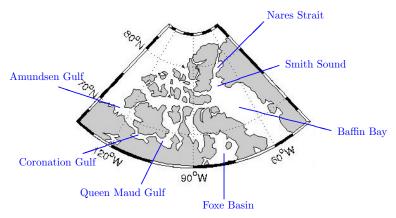


Figure 5.14: Labels of the geographical places of interest for this study in the Canadian Arctic Archipelago.

ical modelling. While numerous GCMs can reproduce sea ice processes in the Arctic, a larger number of them are unable to resolve those processes in the CAA. In Lietaer et al. (2008), the CAA is shown to be important in terms of ice mass balance because it contains 10% of the total Arctic ice volume. Sou and Flato (2009) developed a regional CAA model with a 0-layer sea ice component and a horizontal resolution of 22km. The simulated mean ice concentrations were evaluated against observations in terms of spatial and seasonal variability. Some specific patterns, such as polynyas in Amundsen Gulf and Smith Sound, were reproduced but the model retained too much ice near Alaska and not enough in the southern channels of the CAA. Moreover, the minimum ice cover did not occur at the right time, but several weeks too early.

Every winter, sea ice forms and fully covers the CAA. During the summer months, sea ice does not completely melt in some straits or gulfs. In these sea ice regions, the ice conditions are often stable because of the sea ice persistence (Tivy et al., 2011) Between both extrema, the evolution of the sea ice cover can be followed from spring to autumn by means of satellite data (NSIDC). The observed sea ice melt from May to July is shown in Figure 5.15 and the growth from October to December in Figure 5.16. In the following, the monthly mean ice concentrations simulated by FESOM-LIM3 are qualitatively compared with them, and the results from FESOM simulations which have been performed un-

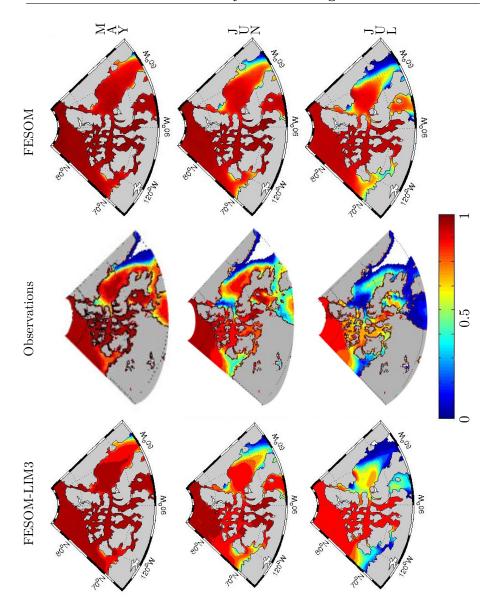


Figure 5.15: Monthly mean ice concentrations for May (top), June (middle) and July (bottom) over the period 1979-2007. Simulated results from FESOM-LIM3 (left) are compared with satellite observations (NSIDC,middle) and simulated results from FESOM (right).

der the same conditions (mesh resolution, forcings).

In Figure 5.15, the FESOM results are illustrated on the right hand-side panels and the FESOM-LIM3 results on those of its left hand-side. In May, the sea ice melting is better represented in FESOM-LIM3. The Amundsen Gulf and the Baffin Bay are the first areas where the sea ice starts to melt, still not sufficiently, but the local ice concentrations are lower than in FESOM. However, the annual North Water Polynya (NWP) does not begin to form in Smith Sound as observed in the satellite datasets (NSIDC). In this open water area, shortwave radiation is highly absorbed, which enhances the ice melt. This is in June that the NWP begins to open in FESOM-LIM3, whereas this region is completely ice free in reality. In the Amundsen Gulf, the ice concentration is 70% which is closer to the 50% value derived from observations than the 90%ice concentration in FESOM. However, the Foxe Basin does not begin to melt in June where its sea ice concentration should be around 0.8. The main features observed in July are well represented by FESOM-LIM3 whereas they are all missing in FESOM. Indeed, in FESOM-LIM3, the Amundsen Bay is almost free of ice, the center of the CAA begins to melt and the ice concentration in the Queen Maud Gulf is low. Besides, the June characteristics are now present: there is 50 - 60% of ice in the Baffin Bay and in the Foxe Basin, and a large NWP. However, the ice remains too compact in the center of the CAA, which is due to the shortwave radiation bias in this area, already mentioned in section 5.2.

Let's now have a look at the sea ice growth in autumn. The satellite observations (NSIDC) show for October ice free areas in the Baffin Bay, the Foxe Basin and the Amundsen Gulf. The NWP is no longer present and the Queen Maud Gulf is half-covered by ice. In November, the Amundsen Gulf becomes fully ice-covered, as well as the north of Baffin Bay. The ice concentration in Foxe Basin is 50%. The CAA is fully covered by ice in December, only some open water areas remain along the eastern Greenland coasts. FESOM-LIM3 well represent these main features with the appropriate timing (Figure 5.16-left), contrary to FESOM in which ice concentrations are generally too large (Figure 5.16-right).

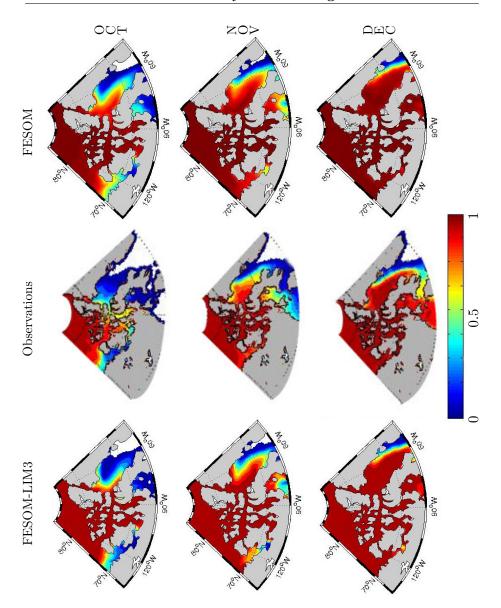


Figure 5.16: Monthly mean ice concentrations for October (top), November (middle) and December (bottom) over the period 1979-2007. Simulated results from FESOM-LIM3 (left) are compared with satellite observations (NSIDC, middle) and simulated results from FESOM (right).

5.3.2 Exports through the main gates of the Arctic basin

The Arctic Ocean is a key component of the global hydrological cycle because it exports, stores, receives, transforms freshwater and has limited connections to the World Ocean. As illustrated in Figure 5.17, the main gates of the

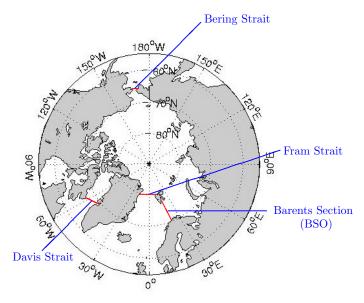


Figure 5.17: Locations of the main Arctic gates studied in this section.

Arctic basin, which are studied in this section, are the Bering Strait, Fram Strait, Davis Strait and the southern Barents Sea Opening (BSO). Between the Baffin Island and Greenland, the Davis Strait is characterized by the relatively warm and salty West Greenland Current (WGC) which flows northwards, and the relatively cold and fresh Baffin Island Current (BIC), which flows in the opposite direction (Figure 5.18). With its narrow width of 350km, it connects the CAA to the Labrador Sea. The only deep path from the Arctic Ocean to the North Atlantic is taken by the cold and fresh East Greenland Current (EGC) and the warm West Spitzbergen Current (WSC) coming from Fram Strait. The BSO allows to the Barents Sea to receive salty water. The Bering Strait, with its width of 85km and depth of 50m, is the only connection between the Pacific and Arctic Oceans. The Pacific waters flowing into the Arctic basin represent an important source of freshwater.

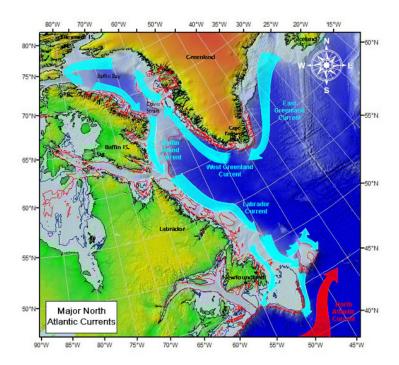


Table 5.1 provides the averages of ocean volume flux through these gates computed for FESOM-LIM3 over the period 1979-2007, and gives observational estimates for comparison. In both cases, a positive value indicates a

	Fram	Bering	Davis	BSO
FESOM-LIM3	-2.22	0.43	-0.206	1.98
Observations	-2.0 ± 2.7^a	0.8 ± 0.2^{b}	-1.6 ± 0.2^{c}	$[2.0; 2.3]^d$

Table 5.1: Mean ocean volume fluxes [Sv] simulated by FESOM-LIM3 and observed (a: Schauer et al. (2008), b: Roach et al. (1995), c: Curry et al. (2013), d: Smedsrud et al. (2010)).

source for the Arctic Ocean. The volume flux F_v is computed by integrating the normal velocity over a vertical cross section of area A:

$$F_v = \int_A \vec{u} \cdot \vec{n} \ dA,$$

where \vec{n} is the unit normal. The results in the Fram Strait and BSO are in good agreement with observations, whereas there is a largely underestimated volume transport in the Davis Strait. However, its mean direction is correct and corresponds to an export. FESOM-LIM3 also underestimates the Bering Strait volume export mostly because of the coarse resolution used in this area (24km).

The solid freshwater flux, which contains contributions from ice and snow, is also studied in these gates. The solid freshwater flux F_{fw} is computed as suggested by Aagaard and Carmack (1989), with the reference salinity of $S_{ref} = 34.8psu$ defined in FESOM, as follows:

$$F_{fw} = \int_0^l \left(\frac{S_{ref} - S_i}{S_{ref}} \frac{\rho_i}{\rho_w} h_i + \frac{\rho_s}{\rho_w} h_s \right) \vec{u_i} \cdot \vec{n} dl,$$

where dl is the ocean depth, $\vec{u_i}$ is the ice velocity, the sea ice salinity S_i is fixed to 6psu, the ice and seawater densities to $940kg/m^3$ and $1000kg/m^3$, respectively. Then, F_{fw} depends on both sea ice thickness and velocity. In the Arctic, the sea ice is mainly formed inside the basin with a small import from the Bering Strait (Woodgate and Aagaard, 2005). There is a net export through all other gates: the Fram and Davis Straits, and BSO, as shown in Table 5.2. Since the CAA limits the ice exports with its narrow straits, the main

	Fram	Bering	Davis	BSO
FESOM-LIM3	-2836	-6.78	-455	-155
Observations	-2300 ± 340^a	100 ± 70^{b}	$[-644; -427]^c$	

Table 5.2: Solid freshwater fluxes $[km^3/year]$ simulated by FESOM-LIM3 and observed (a: Serreze et al. (2006), b: Woodgate and Aagaard (2005), c: Kwok (2007)).

gateway for the solid freshwater to leave the Arctic Ocean is the Fram Strait, where the export is the strongest. In FESOM-LIM3, its particularly high value is related the large ice velocities. All the simulated solid freshwater (FW) fluxes correspond to exports, although it should be an import in the Bering Strait. This small export in this area could be explained by two different behaviours according to the seasons. This feature will be investigated in the discussion below. The Davis Strait export is within the range of observed values.

Figure 5.19 shows the seasonal variability of the solid FW fluxes through the main gates. These exports mainly occur during winter. The vanishing transports in summer in the BSO, Davis and Bering Straits are due to the nearly ice-free conditions. With the largest seasonal variations, a continuous ice export is always observed in the Fram Strait. With its weakest export in August, it remains the major component of the solid freshwater mass balance of the Arctic Ocean since it exports 10% of the total Arctic ice mass each year. As the ice flux

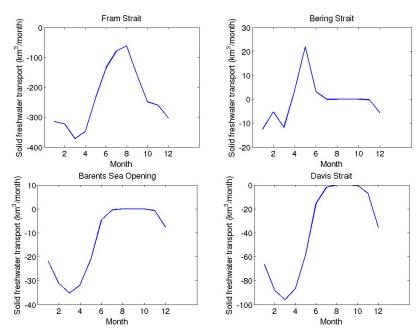


Figure 5.19: Mean seasonal cycles of solid freshwater fluxes through the main gates of the Arctic basin, averaged over 1979 - 2007.

is estimated by Rothrock et al. (2000) in a range from 1600 to $5000km^3/year$ ([130, 415] $km^3/month$), the results are in good agreement with observations for this area. The work of Kwok et al. (2004) also shows a good agreement for this strait, with a montly mean export of around $280 \pm 125 \ km^3/month$. In the Bering Strait, it appears that there is ice export during spring and import in winter, while observed values only show an import anytime (Woodgate and Aagaard, 2005).

5.3.3 Weddell Sea

In the Southern Ocean, the Antarctic Sea Ice Processes and Climate (ASPeCt) database provides sea ice thickness visual estimates (Worby et al., 2008). These measurements are performed from icebreakers as they travel through the ice pack. However, this method is quite subjective and the data may be biased since they are collected on the ship's path only, i.e., where the ice is the thinnest. Over long periods, the only source for information for sea ice thickness variability in the Antarctic remains the data recorded from upward looking sonars (ULS).

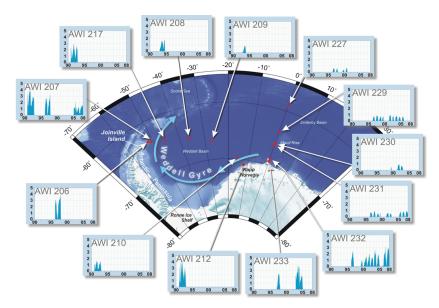


Figure 5.20: Locations of the AWI ULS in the Atlantic sector of the Southern Ocean with diagrams of mean sea ice drafts over the period 1990 - 2008 [figure from A. Behrendt (Behrendt et al., 2013)].

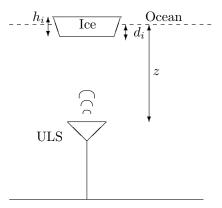


Figure 5.21: Illustration of the measurement principle with ULS, where h_i is the total ice thickness, i_d the ice draft and z the instrument depth.

The Alfred Wegener Institute dropped off 13 instruments in the Weddell Sea, as shown in Figure 5.20, which recorded data over several time periods since 1990. Covering the period 1990 - 2008, this data set includes 3.7 million observations and contains uncorrected raw ice drafts, corrected drafts and basic parameters measured by ULS. In order to assess the sea ice thicknesses simulated by FESOM-LIM3, the four most extensive data sets were considered: ULS 207 to the north of the Antarctica Peninsula and, ULS 229, 231 and 232 located along the prime meridian. The mesh nodes closest to the ULS locations were selected for com-

parison between the model results and observations, as illustrated in Table 5.3.

The sonars transmit sound pulses towards the sea surface, which are reflected both by the water-air interface and by the sea ice bottom. When the pulses gets to the ocean surface, the computed distance is equal to the instrument depth z, as shown in Figure 5.21. When sea ice is present, this is the measure between the ice bottom and ULS. The height of the sea ice portion below the water level, e.g. the ice draft d_i , is then calculated by subtracting this distance from the instrument depth. This information can be used to compute the total ice thickness h_i^T , if the sea ice and snow densities as well as the snow thickness h_s^T are known. The accuracy of these measurements is affected by errors from different sources. For the sake of simplicity, the observed ice drafts will be kept as they are, and the simulated ice thicknesses by FESOM-LIM3 will be transformed into ice drafts by using the equation of hydrostatic balance:

$$\begin{aligned} \rho_s h_s^T + \rho_i h_i^T &= \rho_w d_i \\ \Leftrightarrow d_i &= \frac{\rho_i h_i^T + \rho_s h_s^T}{\rho_w}, \end{aligned}$$

where ρ_i , ρ_s and ρ_w are the ice, snow and seawater densities, respectively.

	Point 207		Point 229	
	Lon	Lat	Lon	Lat
ULS	63°43′W	50°51′S	63°57′W	$0^{\circ}02'E$
Nodes of model	63°48′W	50°54′S	$63^{\circ}45'W$	0°17′W
	Point 231		Point 232	
	Lon	Lat	Lon	Lat
ULS	Lon 66°30′S	Lat 0°01′W	$\frac{\text{Lon}}{69^{\circ}00'S}$	$\frac{\text{Lat}}{0^{\circ}00'E}$

Table 5.3: Locations of the ULS chosen and the closest FESOM-LIM3 nodes, where *Lon* and *Lat* refer to the longitude and latitude, respectively.

Although the ULS database does not cover a large geographical domain, these observations allow to study the temporal variability of ice drafts in particular locations. Figure 5.22 depicts the seasonal evolution of the ice draft derived from the ice thicknesses simulated by FESOM-LIM3. The ice growth and melt timing are in good agreement with observations. However, the ice is much thinner than observed. Near the Antarctica Peninsula, the simulated ice draft is particularly low, with a maximum value around 1m, whereas the largest observations at Point 207 range from 2m to 4m. Along the prime meridian, the results are relatively good, especially for Points 229 and 231. The observations vary from 0m to 1.0-1.3m, and the model thicknesses from 0 to 0.8m. At Point 232, the ULS ice drafts are quite large (3m), while model values do not evolve in the same range,

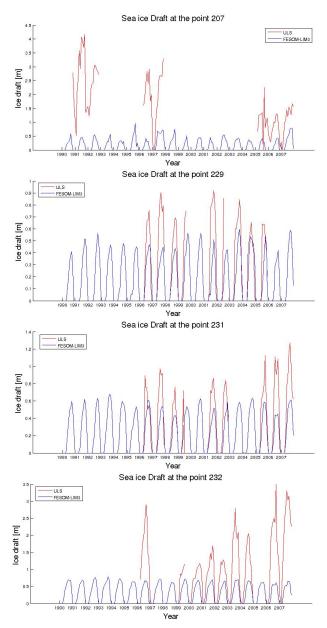


Figure 5.22: Comparison of monthly mean sea ice draft-derived from simulated ice thickness by FESOM-LIM3 (blue) with the ULS ice draft (red) over the period 1990-2007.

with a maximum of 0.7m. As previously mentioned, the FESOM simulation gives ice thicknesses in the S.H. in reasonable agreement with observations. Likewise, its simulated ice drafts have larger amplitudes than FESOM-LIM3 with average values around 1-1.2m.

5.3.4 Discussion

In FESOM-LIM3, the seasonal evolution of the sea ice concentration is particularly well represented in the CAA thanks to the unstructured mesh. As the channels are properly resolved, the straits open and close at the right times in comparison to the satellite observations (NSIDC). For the first time with a state-of-the-art description of the sea ice thermodynamics, this area can be studied in more details. In previous works, LIM3 was used with, at best, a grid of 1° horizontal resolution in global configuration with only one or two channels represented in the CAA (NEMO-LIM3, version 3.1). Even if the new version of NEMO-LIM3 (version 3.5) now permits high-resolution simulations in particular areas, for instance the Svalbard Archipelago (Rousset et al., 2015), no published work has so far been made with more than two resolved channels in the CAA. The too high ice concentrations in the CAA center may be due to a low bias in the shortwave radiation forcing fields, as already mentioned. Besides, the ITD could also be responsible for this characteristic because this is an area of strong convergence and shear (Bitz et al., 2001). Inspired by the work of Thorndike et al. (1975), a fundamental assumption is also made in the function of distribution when shear deformation builds ridges. The thickness distribution is computed according to the same hypothesis as when the ice is broken and piled into ridges, meaning that all the energy is dissipated by shearing. But, Flato and Hibler (1995) showed that only half of this energy is used by shearing, the rest lost to sliding. Nevertheless, this qualitative study gives a first overview of the simulated sea ice state in the CAA and it is in relatively good agreement with observations, contrary to the FESOM simulation which largely overestimated the ice concentration through all the channels of the CAA.

The exports of ocean volume and solid freshwater have been also investigated through the main gates of the Arctic basin. The mean ocean volume fluxes are in good agreement with the various datasets of observations, except for the Davis Strait which has a lower value than observed. The annual mean meridional ocean velocity over all the studied period is computed in order to check the intensity of oceanic currents in this area (Figure 5.23). As expected, the WGC flows northwards along the western Greenland coasts and the BIC goes southwards along the Baffin Islands. In the Davis Strait, the BIC takes up the 2/3 of the channel width but their maximum values are similar. The mean

solid freshwater exports through these same gates are in very good agreement with the observations, but a strange behaviour in the Bering Strait is noticed:

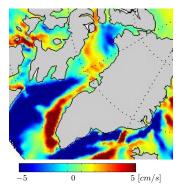


Figure 5.23: Mean annual meridional ocean velocity at the sea surface over the period 1979 – 2007, where a positive value indicates a northwards velocity.

the net export is slightly negative which means that the solid freshwater tends to go out of the Arctic Basin. This behaviour was already observed in other GCMS such as MRI-A, MRI-F or FSU-HYCOM as shown in Wang et al. (2015), but no explanation or hypothesis has been found in this work. Among the different saved prognostic variables, the study of the sea surface elevation in this area does not reveal anything in particular. In the Bering Strait, the monthly mean meridional wind fields from the COREv2 are mainly oriented southwards, whereas the ocean velocity is directed northwards, but both are in the same range of intensity which is around Considering those elements, the 10cm/s. atmosphere-ice drag is maybe too large in this area with the inclusion of the ITD. Indeed, the ITD representation tends to give

thinner ice in the marginal ice zones. The Figure 5.24 shows the ice velocities in March and May, when the minimum and maximum exports are simulated by FESOM-LIM3. Likewise, the ice is exported in March with a meridional velocity of around 3cm/s towards the Bering Sea where the ice velocity is particularly strong (15cm/s), and towards the Chukchi Sea in May with a velocity around 7.5cm/s. With these investigations, no pertinent conclusion can be drawn and this area may deserve a further study.

Finally, the ice draft in the S.H. has been studied in some particular locations of the Weddell Sea where ULS data are available. As previously mentioned, the underestimation of the ice thickness could be due to unadapted parameters, such as too small a lead closing parameter value or the large ITD boundaries. The difference of amplitude could also come from the wrong locations correspondence which has been established between the ULS position and the node coordinates. Besides, the numerous ridges and raftings which influence the ice distribution in a small area cover, could amplify this amplitude difference. Especially, the underestimation of ice drafts at Points 207 and 232 could be attributed to the forcing data. The computation of the ice draft is based on the ice and snow densities which are taken constant in FESOM-LIM3 $(910kg/m^3)$ and $290kg/m^3)$, whereas their observed values range from 720 to $940kg/m^3$ (Timco and Frederking, 1996) and from 100 to $400kg/m^3$ (Meløysund et al., 2007), respectively. Moreover, the snow thickness is also

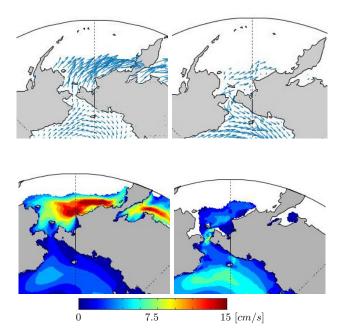


Figure 5.24: Mean ice velocities in March (left) and May (right) simulated over the period 1979-2007 in the Bering Strait.

required in this computation and is given by FESOM-LIM3 itself. In order to compute d_i , all these constant approximations can lead to some quite large errors. Some other errors can also appear through the measure uncertainties of the sonars or in the parameters used in the correction approach's (Behrendt et al., 2013). Despite that, the freezing and melting timing phases in the simulated time series are realistic with regard to the observations.

5.4 Concluding remarks

In the global evaluation, FESOM-LIM3 provides a first reasonably good description of the mean sea ice states in both the N.H. and S.H. In the Arctic, the sea ice concentrations, volumes and velocities are in agreement with the available observations, and the ITDs are reasonably represented over a part of the Arctic basin. Only the center of the CAA slightly remains covered by sea ice in summer, which is mainly due to the low bias of the COREv2 shortwave radiation forcing in this area. In the Southern Ocean, the underestimation of the ice thickness in summer may be due to not-well adapted parameters for this

area, such as the single value of the lead closing parameter or the large values for the ITD boundaries. However, the ice concentrations and velocities remain realistic, especially in summer since almost all the sea ice melts in winter.

In the second part of this chapter, the seasonal variability of different ice state variables was evaluated in particular coastal regions. In the straits of the CAA, the spring melting and the autumn freezing, which open or close different channels or gulfs, occur at the right times and places according to the satellite observations (NSIDC). Through the main gates of the Arctic basin (Bering Strait, Fram Strait, BSO, Davis Strait), the annual mean of the ocean volume flux and the solid freshwater exports are in good agreement with regard to the available observations, and their seasonal variability also remain within the range of the observations, except for the Bering Strait. A strange behaviour in this place is noticed in winter with ice exported towards the Bering Sea. The time series of ice draft in the Weddell Sea are reasonably consistent with the ULS data, even if the ice thickness in this hemisphere is quite underestimated.

The coupling of FESOM and LIM3 thus provides a sophisticated sea iceocean model discretized in finite element. The inclusion of the key components
of LIM3 in FESOM allows to study in details some areas which were, until now,
often unresolved or represented with a coarse resolution. This first version
of FESOM-LIM3 proves to be quite well tuned for the mean sea ice state,
especially in the N.H. With the knowledge of its flaws, the coupled model is
suitable for large-scale sea ice and climate simulations. In order to improve
the sea ice simulation in the S.H. considerably, a fine calibration of the various
parameters should be the first of priorities. For instance, an idea may be to
differentiate the value of the lead closing parameter in order to distinguish
both hemispheres. Besides, the boundaries in the ITD could be adapted or
another deep oceanic convection scheme could be used to see if some changes
are noticed. All these changes should be studied and improved in the future.
In the N.H., it could be interesting to analyze in more details the ITD impact
on FESOM-LIM3 or to use other atmospheric forcing fields.

C H A P T E R

Conclusions

Even if the use of parameterizations of subgrid-scale processes is widespread in GCMs discretized with structured grids, their inclusion in finite element sea ice - ocean models still raises questions about the influences of these parameterizations on the model results or the improvements of the model skills. Indeed, the unstructured meshes in which the elements size can strongly vary, bring issues about the adjustments of these parameterizations according to the shape and the sizes of the grid elements.

The parameterization of mesoscale eddies, which occur in most places of the World Ocean, is usually treated as two distinct processes: the isopycnal diffusion and the Gent-McWilliams (GM) velocity, that are represented as suggested by Redi (1982) and Gent et al. (1995), respectively. Although these parameterizations significantly improve the oceanic results, they also sometimes produce unwanted behaviours, such as unexpected diffusion (Griffies, 2004). The follow question: How to reduce the use of numerical artefacts associated with those parameterizations to the benefit of their physics?, was one of the central questions of this thesis. Thanks to the oriented penalty factor introduced, which is especially built for the strongly anisotropy diffusivity tensor, the numerical scheme is sufficiently stable and the numerical errors associated to the inclusion of this isopycnal diffusion in SLIM appear to be less important than with other penalty factors. Because the penalty factor influences the results, its estimation is not an easy task. In Chapter 2, the oriented penalty

134 Conclusions

factor seems to be the most appropriate (it induces less numerical diffusion, lower \mathcal{L}_2 error¹, better condition number and better convergence) with respect to the other ones. It was then selected for the oceanic applications examined in Chapter 3. The tracer concentration, initialized as a Gaussian, really tends to follow the isopycnals in a progressively inclining density field. As, initially, the penalty factor is not adapted to follow the isopycnals, unwanted diapycnal diffusion is induced by the numerical scheme. But with the oriented penalty factor, this spurious diffusion appears to be negligible with regard to the real diapycnal diffusion. With this parameterization and the special treatment of the penalty factor, the physical processes associated with the isopycnal diffusion really seem to be respected and the remaining artefacts do not seem to consequently affect the ocean results.

For the GM velocity, the one-dimensional boundary value problem suggested by Ferrari et al. (2010) was applied in SLIM in order to avoid additional tapering functions and ensure impermeable boundaries over the domain. The idealized channel simulation investigated in Chapter 3 highlighted the interest to include this parameterization in SLIM. Under the action of the wind, the isotherms are getting extremely steep without the GM parameterization and this kind of pattern could lead to numerical issues, such as high oceanic instabilities. However, this feature is removed when the GM parameterization is activated. Indeed, the isotherms are slumped and the stratification close to the ocean surface is modified. Thanks to the one-dimensional boundary value problem statement, the usual additional numerical artefacts relative to the GM velocity are avoided and the expected oceanic behaviours such as the slumped isopycnals, seem to be well estimated in SLIM applications.

In this first part, I learned that the numerical schemes are far from being perfect and numerous artefacts can appear if we do not pay attention. However, it is often possible to deal with these issues and find adequate methods in order to minimize their effects while better emphasizing the physical processes.

Subgrid-scale processes can also be parameterized in sea ice models in order to improve their skills and to reach a high level of complexity in the physics representation. Although they already yield real improvements when they are taken into account in sea ice models running on structured grids, these parameterizations were never included in sea ice models based on unstructured meshes. This is why we addressed the following question in this thesis: what

¹The \mathcal{L}_2 error is defined as the square root of the sum of the square of the differences between the numerical and analytical solutions.

Conclusions 135

are the interest and potential applications of having a state-of-the-art representation of the sea ice physics on an unstructured mesh? The key components of LIM3 have been coupled with the sea ice - ocean model FE-SOM described in Chapter 4 in order to take the advantages of each model. The unstructured mesh from FESOM associated to the inclusion of a state-of-the-art representation of the halo-thermodynamics and the ice thickness distribution (ITD) with the multi-category formalism of LIM3 required some technical adaptations with regard to the heat fluxes at the interfaces. In particular, the albedo parameterization, initially included in FESOM, which consisted in four constant valuesdoes not appear to be well suited for the multi-category formalism of LIM3. In order to get a realistic mean sea ice state over the 1979 – 2007 period, the parameterization of Shine and Henderson-Sellers (1985) was modified to reach the albedo values in the same range of FESOM's ones and to take the ice thickness into account for albedo calculations.

In Chapter 5, the mean geographical distributions of sea ice concentration are shown to be well simulated in the Arctic. The simulated ice thickness in parts of the northern Canadian Arctic Archipelago is smaller overall than observed in March and April, and its distribution is shifted towards the thinner categories with regard to the IceBridge observations. Such low biases were also observed in studies conducted by NEMO-LIM3 (Massonnet et al., 2011; Vancoppenolle et al., 2009b). The mean seasonal cycle of ice extent only differs by 10% in amplitude compared to the NSIDC observations in which the errors can vary from 5% in winter to 20% in summer (Partington et al., 2003). In the Arctic, the time series of monthly anomalies of ice extent simulated by FESOM-LIM3 and observed (NSIDC) are especially well correlated (0.87), contrary to the S.H. (0.22). This difference of features in both hemispheres can be due to some unadapted parameters for the S.H., such as the lead closing parameter or the boundaries of the ITD. Moreover, in the Antarctic, the ice thickness is clearly underestimated by 40% and the sea ice almost completely disappears in summer.

In the Canadian Arctic Archipelago, where all the narrow straits are represented, FESOM-LIM3 exhibits specific characteristics that were missing in the FESOM simulations, such as polynyas in the Amundsen Gulf and Smith Sound. In the main gates of the Arctic, the simulated solid freshwater fluxes, which contain contributions from ice and snow, are in good agreement with observations, except in the Bering Strait, where the solid freshwater flux tends to go out of the Arctic basin. The seasonal solid freshwater flux is particularly well simulated by FESOM-LIM3 with a continuous ice export all over the year in the range of observations. Even if the ice drafts are underestimated with respect to ULS observations, as for the S.H., the freezing and melting timing

136 Conclusions

phases in these time series remain realistic.

The coupling of FESOM and LIM3 provides a sophisticated sea ice - ocean model discretized on an unstructured mesh and enables to study in details some areas which were, until now, unresolved or represented with a coarse resolution. Even if some improvements are expected from models including a high-level of complexity within the representation of sea ice and ocean physics, this is not trivial. A fine calibration of the parameters should be performed to ensure such improvements in the simulations. From this perspective, further investigations are required.

In this second part, I learned that the coupling between key components of two different sea ice - ocean models is not obvious even if they separately provide satisfactory results with respect to observations. In order to simulate the mean sea ice state in a reasonable way, the calibration of such models remains necessary although complex and difficult to investigate.

Perspectives

In the first two chapters of this thesis, the effects of mesoscale eddies which have been parameterized in SLIM have been only studied in test cases or idealized ocean applications. When the computational time will be optimized, some longer simulations could be conducted as in the studies of (Griffies, 1998; Ferrari et al., 2010) or more complex areas, such as the Gulf Stream region or the Southern Ocean, could be dealt with in greater details (Hallberg, 2013). In this way, the understanding of these still not well-know processes and their impacts could be improved.

With the new coupled sea ice - ocean model FESOM-LIM3, various works are possible. Even if the sea ice is well simulated in the N.H., there is a large underestimation of ice extent in the S.H. This issue is perhaps due to unadapted parameters, such as the lead closing parameter or the number of categories in the ITD. The first improvement to bring would be to achieve a fine calibration for both hemispheres. The most appropriate values should be investigated through several long-term simulations.

Besides, the strange behaviour of the solid freshwater flux noticed in the Bering Strait would deserve further investigations. Even if this feature has already been observed in others GCMs (Wang et al., 2015), no explanation or hypothesis was suggested. The effects of changes in the value of the ice-atmosphere drag coefficient could be examined in order to fix the flux issue in

Conclusions 137

the Bering strait. Indeed, its value is maybe too large with the inclusion of the ITD and as the ice is thinner in the marginal ice zones, its motion can easily be influenced by the winds.

As the model is forced by atmospheric fields, these also have some repercussions on the results. For instance, the simulated too thick sea ice in the center of the Canadian Arctic Archipelago is mainly due to a low bias of the COREv2 shortwave radiation forcing in this area. It should be interesting to use other atmospheric forcing fields to study its impacts on the sea ice results, as for NEMO-LIM3 in the study of Lindsay et al. (2014). Besides, the subgrid-scale parameterizations in the oceanic and sea ice components are often functions of several forcing fields, such as the air temperature or the winds. The resolution of these atmospheric forcing fields then becomes crucial and may lead to an optimum behaviour of the parameterizations only if it is consistent with the model resolution below (Winton et al., 2014). If the forcing resolution is too coarse, the advantages of parameterizations adapted to a finer model grid are lost. From this perspective, running a simulation with another set of high resolution forcing fields should lead to different results with FESOM-LIM3 and may deserve further studies.

After some other adjustments to improve the mean sea ice states in both hemispheres, some more quantitative studies could be performed in order to study areas of particular interest, e.g. the Svalbard Archipelago investigated in Rousset et al. (2015). In addition, some other variables can be influenced by the resolution of specific areas and relative studies can therefore be handled. For instance, the modelled freshwater fluxes could be analyzed in the straits of the Canadian Arctic Archipelago in comparison with the work of Wekerle et al. (2013), where simpler sea ice physics was used.

Finally, some other representations of the sea ice physics, such as a description of the sea ice rheology based on its elasto-brittle behaviour (Girard et al., 2011) or the inclusion of a comprehensive snow scheme (Lecomte et al., 2013) might be implemented in FESOM-LIM3 in order to further increase its level of complexity and to see if these new processes really improve the sea ice simulations.

Appendices

A P P E N D I X

Supplementary material for Chapter 3

A1. Local tracer consistency

The property of local tracer consistency requires that the discrete tracer equation preserves constants in a closed domain, if there is no source or sink (White et al., 2008b). This is equivalent to verifying that a constant tracer concentration is the solution of equation (3.5). After integration by parts, the weak formulation of the free evolution of the tracer concentration with only the Gent-McWilliams velocity follows this equation:

$$\int_{\varOmega_e} \frac{\partial C}{\partial t} \tau d\Omega + \sum_k \int_{\gamma_k} \underline{n} \cdot \{\underline{u}_{ed}\} \ C \tau d\Gamma - \int_{\varOmega_e} \nabla \tau \cdot \underline{u}_{ed} \ C \ d\Omega = 0 \ \ \forall e. \quad (A.1)$$

In order to have consistency, the following equation is obtained by imposing C to be constant in space:

$$\underbrace{\sum_{k} \int_{\gamma_{k}} \underline{n} \cdot \{\underline{u}_{ed}\} \ \tau d\Gamma}_{\widehat{\mathbf{I}}} - \underbrace{\int_{\Omega_{e}} \nabla \tau \cdot \underline{u}_{ed} d\Omega}_{\widehat{\mathbf{Z}}} = 0. \tag{A.2}$$

The Gent-McWilliams velocity is defined from the streamfunction ψ such that:

$$\begin{array}{rcl} \underline{u}_{ed} & = & \nabla \times \underline{\psi} \\ & = & \begin{pmatrix} -\partial_z \psi_y \\ \partial_z \psi_x \\ \partial_x \psi_y - \partial_y \psi_x \end{pmatrix}. \end{array}$$

In terms of the finite element approximation, this yields:

$$\psi_{x,z}^{h} = \sum_{i} \psi_{x}^{i} \frac{\partial \tau_{i}}{\partial z}$$

$$\Longrightarrow \underline{u}_{ed}^{h} = \begin{pmatrix} -\sum_{i} \psi_{y}^{i} \frac{\partial \tau_{i}}{\partial z} \\ \sum_{i} \psi_{x}^{i} \frac{\partial \tau_{i}}{\partial z} \\ \sum_{i} \psi_{y}^{i} \frac{\partial \tau_{i}}{\partial z} - \sum_{i} \psi_{x}^{i} \frac{\partial \tau_{i}}{\partial y} \end{pmatrix}.$$

The term ① of equation (A.2) can be written as:

$$\begin{split} \sum_{k} \int_{\gamma_{k}} \underline{n} \cdot \{ \underline{u}_{ed}^{h} \} \ \tau_{j} d\Gamma \\ &= \sum_{k} \int_{\gamma_{k}} \sum_{i} \left[-n_{x} \left(\frac{\psi_{i y}^{+} + \psi_{i y}^{-}}{2} \right) \frac{\partial \tau_{i}}{\partial z} + n_{y} \left(\frac{\psi_{i x}^{+} + \psi_{i x}^{-}}{2} \right) \frac{\partial \tau_{i}}{\partial z} \right. \\ &+ n_{z} \left(\frac{\psi_{i y}^{+} + \psi_{i y}^{-}}{2} \right) \frac{\partial \tau_{i}}{\partial x} - n_{z} \left(\frac{\psi_{i x}^{+} + \psi_{i x}^{-}}{2} \right) \frac{\partial \tau_{i}}{\partial y} \right] \tau_{j} d\Gamma \\ &= \sum_{k} \sum_{i} \left[-\left(\frac{\psi_{i y}^{+} + \psi_{i y}^{-}}{2} \right) \int_{\gamma_{k}} n_{x} \frac{\partial \tau_{i}}{\partial z} \tau_{j} d\Gamma + \left(\frac{\psi_{i x}^{+} + \psi_{i x}^{-}}{2} \right) \int_{\gamma_{k}} n_{y} \frac{\partial \tau_{i}}{\partial z} \tau_{j} d\Gamma \right. \\ &+ \left(\frac{\psi_{i y}^{+} + \psi_{i y}^{-}}{2} \right) \int_{\gamma_{k}} n_{z} \frac{\partial \tau_{i}}{\partial x} \tau_{j} d\Gamma - \left(\frac{\psi_{i x}^{+} + \psi_{i x}^{-}}{2} \right) \int_{\gamma_{k}} n_{z} \frac{\partial \tau_{i}}{\partial y} \tau_{j} d\Gamma \right]. \end{split}$$

In addition, the integration by parts can be used:

$$\int_{\Omega_e} \frac{\partial}{\partial x} \left(\frac{\partial \tau_i}{\partial z} \right) \tau_j d\Omega = \int_{\gamma_k} n_x \frac{\partial \tau_i}{\partial z} \tau_j d\Gamma - \int_{\Omega_e} \frac{\partial \tau_i}{\partial z} \frac{\partial \tau_j}{\partial x} d\Omega.$$

The equation (A.1) then becomes:

$$\sum_{k} \int_{\gamma_{k}} \underline{n} \cdot \{\underline{u}_{ed}^{h}\} \tau d\Gamma
= \sum_{k} \sum_{i} \left[-\left(\frac{\psi_{i y}^{+} + \psi_{i y}^{-}}{2}\right) \int_{\Omega_{e}} \left(\frac{\partial}{\partial x} \left(\frac{\partial \tau_{i}}{\partial z}\right) \tau_{j} + \frac{\partial \tau_{i}}{\partial z} \frac{\partial \tau_{j}}{\partial x} \right) d\Omega \right.
+ \left. \left(\frac{\psi_{i x}^{+} + \psi_{i x}^{-}}{2}\right) \int_{\Omega_{e}} \left(\frac{\partial}{\partial y} \left(\frac{\partial \tau_{i}}{\partial z}\right) \tau_{j} + \frac{\partial \tau_{i}}{\partial z} \frac{\partial \tau_{j}}{\partial y} \right) d\Omega \right.
+ \left. \left(\frac{\psi_{i y}^{+} + \psi_{i y}^{-}}{2}\right) \int_{\Omega_{e}} \left(\frac{\partial}{\partial z} \left(\frac{\partial \tau_{i}}{\partial x}\right) \tau_{j} + \frac{\partial \tau_{i}}{\partial x} \frac{\partial \tau_{j}}{\partial z} \right) d\Omega \right.
- \left. \left(\frac{\psi_{i x}^{+} + \psi_{i x}^{-}}{2}\right) \int_{\Omega_{e}} \left(\frac{\partial}{\partial z} \left(\frac{\partial \tau_{i}}{\partial y}\right) \tau_{j} + \frac{\partial \tau_{i}}{\partial y} \frac{\partial \tau_{j}}{\partial z} \right) d\Omega \right] \right.
= \sum_{k} \sum_{i} \left[\left(\frac{\psi_{i y}^{+} + \psi_{i y}^{-}}{2}\right) \int_{\Omega_{e}} \left(\frac{\partial \tau_{i}}{\partial x} \frac{\partial \tau_{j}}{\partial z} - \frac{\partial \tau_{i}}{\partial z} \frac{\partial \tau_{j}}{\partial x} \right) d\Omega \right.
+ \left. \left(\frac{\psi_{i x}^{+} + \psi_{i x}^{-}}{2}\right) \int_{\Omega_{e}} \left(\frac{\partial \tau_{i}}{\partial z} \frac{\partial \tau_{j}}{\partial y} - \frac{\partial \tau_{i}}{\partial y} \frac{\partial \tau_{j}}{\partial z} \right) d\Omega \right] . \tag{A.3}$$

As the interface side by default is the left-hand side, the term ② of equation (A.2) can be written as:

$$\int_{\Omega_{e}} \nabla \tau_{j} \cdot \underline{u}_{ed}^{+} d\Omega = \sum_{i} \left[\psi_{i y}^{+} \int_{\Omega_{e}} \left(\frac{\partial \tau_{i}}{\partial x} \frac{\partial \tau_{j}}{\partial z} - \frac{\partial \tau_{i}}{\partial z} \frac{\partial \tau_{j}}{\partial x} \right) d\Omega + \psi_{i x}^{+} \int_{\Omega_{e}} \left(\frac{\partial \tau_{i}}{\partial z} \frac{\partial \tau_{j}}{\partial y} - \frac{\partial \tau_{i}}{\partial y} \frac{\partial \tau_{j}}{\partial z} \right) d\Omega \right].$$
(A.4)

With the solutions (A.3) and (A.4), equation (A.2) can be written as:

$$\sum_{i} \left[\left(\frac{\psi_{iy}^{-} - \psi_{iy}^{+}}{2} \right) \int_{\Omega_{e}} \left(\frac{\partial \tau_{i}}{\partial x} \frac{\partial \tau_{j}}{\partial z} - \frac{\partial \tau_{i}}{\partial z} \frac{\partial \tau_{j}}{\partial x} \right) d\Omega + \left(\frac{\psi_{ix}^{-} - \psi_{ix}^{+}}{2} \right) \int_{\Omega_{e}} \left(\frac{\partial \tau_{i}}{\partial z} \frac{\partial \tau_{j}}{\partial y} - \frac{\partial \tau_{i}}{\partial y} \frac{\partial \tau_{j}}{\partial z} \right) d\Omega \right] = 0.$$

 ψ must then be continuous to be consistent.

A2. Conservation

In this case, the tracer concentration depends on time and space. After integrating on the volume, the free evolution of the tracer concentration with only

the Gent-McWilliams velocity can be written as:

$$\int_{\varOmega} \frac{\partial C}{\partial t} d\Omega + \int_{\varOmega} \nabla \cdot \left(\underline{u}_{ed} \ C\right) d\Omega = 0.$$

After integration by parts, the equation becomes:

$$\frac{d}{dt} \int_{\varOmega} C \ d\varOmega + \int_{\partial \varOmega} \underline{n} \cdot (\underline{u}_{ed} \ C) \, d\Gamma = 0.$$

With the streamfunction \widetilde{Y} , the Gent-McWilliams velocity becomes:

$$\underline{u}_{ed}^{h} = \begin{pmatrix} \sum_{i} \widetilde{Y}_{x}^{i} \frac{\partial \tau_{i}}{\partial z} \\ \sum_{i} \widetilde{Y}_{y}^{i} \frac{\partial \tau_{i}}{\partial z} \\ -\sum_{i} \widetilde{Y}_{x}^{i} \frac{\partial \tau_{i}}{\partial x} - \sum_{i} \widetilde{Y}_{y}^{i} \frac{\partial \tau_{i}}{\partial y} \end{pmatrix}.$$

Since $\widetilde{Y}(\Gamma) = 0$, the second term of the equation disappears and the equation becomes:

$$\frac{d}{dt} \int_{\Omega} C \ d\Omega = 0.$$

The tracer concentration is then conserved.



Supplementary material for Chapter 4

B.1 EVP rheology in FESOM

In the representation of the sea ice dynamics in FESOM, the elastic-visco-plastic (EVP) rheology is performed as suggested by Hunke and Dukowicz (2001). Under the assumption that the sea ice is behaving as a non-linear compressible viscous fluid, its internal stress tensor follows the equation:

$$\sigma_{ij} = 2\eta(\epsilon_{ij} - \frac{1}{2}\delta_{ij}\epsilon_{kk}) + \zeta\delta_{ij}\epsilon_{kk} - \frac{1}{2}\delta_{ij}P,$$

where

$$\epsilon_{ij} = \frac{1}{2} \left(\frac{\partial u_i}{\partial x_j} + \frac{\partial u_j}{\partial x_i} \right)$$

is the deformation rate tensor, η and ζ are the shear and bulk viscosities, respectively, and P is the ice strength which depends on the ice concentration a_i and thickness h_i :

$$P = P^* h_i e^{(-c(1-a_i))}.$$

As empirical parameters, $P^*=23000N/m^2$ and c=20. From these calculations,

$$\Delta^2 = \left(\epsilon_{11}^2 + \epsilon_{22}^2\right) \left(1 + 1/e^2\right) + 4\epsilon_{12}^2/e^2 + 2\epsilon_{11}\epsilon_{22} \left(1 - 1/e^2\right),\,$$

where the eccentricity e = 2. The shear and bulk viscosities are written as:

$$\begin{array}{rcl} \eta & = & \frac{P}{2\Delta}, \\ \\ \zeta & = & \frac{P}{2e^2\Delta}. \end{array}$$

With $\sigma_D = \sigma_{11} + \sigma_{22}$, $\sigma_T = \sigma_{11} - \sigma_{22}$, the EVP model consists in the following time-dependent equations:

$$\begin{split} \frac{\partial \sigma_D}{\partial t} + \frac{\sigma_D}{2T} + \frac{P}{2T} &= \frac{P}{2T\Delta} \epsilon_D, \\ \frac{\partial \sigma_T}{\partial t} + \frac{e^2 \sigma_T}{2T} &= \frac{P}{2T\Delta} \epsilon_T, \\ \frac{\partial \sigma_{12}}{\partial t} + \frac{e^2 \sigma_{12}}{2T} &= \frac{P}{2T\Delta} \epsilon_{12}, \end{split}$$

where the deformation rate components are $\epsilon_D = \epsilon_{11} + \epsilon_{22}$ and $\epsilon_T = \epsilon_{11} - \epsilon_{22}$, and an implicit time stepping scheme (backward Euler) is used to solve them.

B.2 Correspondance in the name of variables between FESOM and LIM3

The purpose of this technical subsection is to provide the information required to reproduce this coupling, especially through the correspondence in the name of variables between FESOM and LIM3.

Equivalence of symbols			
FESOM	LIM3	Variable names	
	a_i	ice concentration (5 categories)	
a_i^T	$\sum_{i=1}^{N=5} a_i$	total ice concentration	
	v_i	ice volume by unit area (5 categories)	
$m_i = \frac{M_i}{ ho_i}$	v_i^T	total ice volume per unit area	
	v_s	snow volume by unit area (5 categories)	
$m_s = \frac{M_s}{\rho_s}$	v_s^T	total snow volume per unit area	
T_s	$\sum_{i=1}^{N=5} \frac{a_i T_{s,i}}{a_i^T}$	total surface temperature (ice or snow)	
$ ilde{h_i}$	$\sum_{i=1}^{N=5} \frac{a_i v_i}{a_i^T}$	effective ice thickness	
$ ilde{h_s}$	$\sum_{i=1}^{N=5} \frac{a_i v_s}{a_i^T}$	effective snow thickness	

Table B.1: Equivalent variables in LIM3 and FESOM.

- K. Aagaard and E. Carmack. The role of Sea Ice and Other Fresh Water in the Arctic Circulation. J. Geophys. Res., 94, 1989. 6, 124
- M. Ainsworth. Dispersive and dissipative behaviour of high order discontinuous Galerkin finite element methods. J. Computational Physics, 198(1):106–130, 2004. 23, 54
- D. Arnold, F. Brezzi, B. Cockburn, and D. Marini. Discontinuous Galerkin methods for elliptic problems. In *Discontinuous Galerkin Methods*, pages 89–101. Springer, 2000. 27
- U. M. Ascher, S. J. Ruuth, and R. J. Spiteri. Implicit-explicit Runge-Kutta methods for time-dependent partial differential equations. Appl. Num. Math., 25:151–167, 1997. 35
- F. Badgley. Heat balance at the surface of the arctic ocean. pages 215–246. Symposium on the Arctic Heat Budget and Atmospheric Circulation, edited by J.O. Fletcher, Rand Corporation, Santa Monica, Calif., 1966. 14
- A. Barthélemy, T. Fichefet, H. Goosse, and G. Madec. Modeling the interplay between sea ice formation and the oceanic mixed layer: Limitations of simple brine rejection parameterizations. *Ocean Mod.*, 86:141–152, 2015. 114, 115
- E. Becker. The finite element method in aidjex. AIDJEX Bull., 33:144–157, 1976. 10
- A. Behrendt, W. Dierking, E. Fahrbach, and H. Witte. Sea ice draft in the weddell sea, measured by upward looking sonars. *Earth Syst. Sci. Data*, 5: 209–226, 2013. 126, 131
- M. Berliand and T. Strokina. Global distribution of the total amounts of clouds (in russian). *Isv. Akad. Nauk. SSSR Ser. Geophys.*, 1, 1980. 85
- P. Bernard, N. Chevaugeon, V. Legat, E. Deleersnijder, and J. Remacle. Highorder h-adaptive discontinuous galerkin methods for ocean modelling. *Ocean Dyn.*, 57:109–121, 2007. 9

D. Bi, M. Dix, S. Marsland, S. O'Farrell, H. Rashid, P. Uotila, A. Hirst, E. Kowalczyk, M. Golebiewski, A. Sullivan, H. Yan, N. Hannah, C. Franklin, Z. Sun, P. Vohralik, I. Watterson, X. Zhou, R. Fiedler, M. Collier, Y. Ma, J. Noonan, L. Stevens, P. Uhe, H. Zhu, S. Griffies, R. Hill, C. Harris, and K. Puri. The access coupled model: description, control climate and evaluation. Aust. Met. Oceanogr. J., 2013. 12

- C. Bitz and W. Lipscomb. An energy-conserving thermodynamic model of sea ice. J. Geophys. Res., 104:15669–15677, 1999. 13, 84
- C. Bitz, M. Weaver, and M. Eby. Simulating the ice-thickness distribution in a couple climate model. J. Geophys. Res., 106:2441–2463, 2001. 12, 83, 84, 129
- S. Blaise, R. Comblen, V. Legat, J.-F. Remacle, E. Deleersnider, and J. Lambrechts. A discontinuous finite element baroclinic marine model on unstructured prismatic meshes. Part I: space discretization-. *Ocean dyn.*, 60:1371–1393, 2010. 1, 23, 53
- S. Bouillon, M. Maqueda, V. Legat, and T. Fichefet. An elastic-viscous-plastic sea ice model formulated on Arakawa B and C grids. *Ocean Mod.*, 27:174–184, 2009. 15, 83
- C. Chen, H. Liu, and R. Beardsley. An unstructured grid, finite-volume, three-dimensional, primitive equations ocean model: application to coastal ocean and estuaries. *J. atm. ocean. tech.*, 20:159–186, 2003. 9, 78
- B. Cockburn, G. Karniadakis, and C. Shu. *Discontinuous Galerkin methods:* theory, computation and applications. Springer, USA, 2000. 23, 28
- R. Comblen. Discontinuous finite element methods for two- and threedimensional marine flows. PhD thesis, Université catholique de Louvain, 2010. 65
- J. Comiso. Bootstrap sea ice concentrations from nimbus-7 smmr and dmsp ssm/i, 1979-2006. Technical report, NSIDC, 2007. 103
- J. Comiso, P. Wadhams, L. Pedersen, and R. Gersten. Seasonal and interannual variability of the odden ice tongue and a study of environmental effects. J. Geophys. Res., 106:9093–9116, 2001. 116
- M. Coon, S. Maykut, R. Richard, D. Rothock, and A. Thorndike. Modeling the pack ice as an eslatic-plastic material. AIDJEX Bull., 24:1–105, 1974. 13
- G. F. N. Cox and W. F. Weeks. Numerical simulations of the profile properties of undeformed first-year sea ice during the growth season. *J. Geophys. Res.*, 93:12449–12460, 1988. 85

M. Cox. Isopycnal diffusion in a z-coordinate ocean model. Ocean Mod., 74: 1–5, 1987. 5, 36, 48, 58

- J.-P. Croisille, A. Ern, T. Lelièvre, and J. Proft. Analysis and simultion of a coupled hyperbolic-parabolic model problem. J. Numer. Math., 13:81–103, 2005. 23
- B. Curry, C. M. Lee, B. Petrie, R. E. Moritz, and R. Kwok. Multiyear Volume, Liquid Freshwater, and Sea Ice Transports through Davis Strait, 2004-10. *J. Phys. Oceanog.*, 44:1244–1266, 2013. 123
- A. Dai, T. Quian, K. Trenberth, and J. Milliman. Changes in continental freshwater discharge from 1948 to 2004. J. Clim., 22:2773–2792, 2009. 94
- G. Danabasoglu and J. McWilliams. Sensitivity of the global ocean circulation to parametrizations of mesoscale tracer transports. J. Climate, 8:2967–2987, 1995. 4, 16, 52
- G. Danabasoglu, J. McWilliams, and P. Gent. The role of mesoscale tracer transport in the global ocean circulation. *Science*, 264:1123–1126, 1994. 4, 52
- S. Danilov, G. Kivman, and J. Schröter. A finite-element ocean model: principles and evaluation. *Ocean Mod.*, 6:125–150, 2004. 1, 9, 79, 80
- N. Douglas. An Interior Penalty Finite Element Method with Discontinuous Elements. SIAM J. NUMER. ANAL., 19:742–760, 1982. 23
- J. P. Dunne, J. G. John, A. J. Adcroft, S. M. Griffies, R. Hallberg, E. Shevliakova, S. R.J., W. Cooke, K. Dunne, M. Harrison, J. Krasting, S. Malyshev, P. Milly, P. Phillipps, L. Sentman, B. Samuels, M. Spelman, M. Winton, A. Wittenberg, and N. Zadeh. Gfdl's esm2 global coupled climate-carbon earth system models. part i: Physical formulation and baseline simulation characteristics. J. Climate, 25:6646–6665, 2012. 12
- E. Eady. Long waves and cyclone waves. Tellus, 1:33-52, 1949. 12, 56
- A. Ern, A. Stephansen, and P. Zunino. A discontinuous galerkin method with weighted average for advection-diffusion equations with locally small and anisotropic diffusivity. *J. Num. Ana.*, 29:235–256, 2008. 24, 32
- R. Farneti. The ictp-mom ocean model: Core-i and core-ii simulations. 10th Session of the CLIVAR Working Group on Ocean Model Development, Venice, Italy, 2012. 12
- V. I. Fedotov, N. V. Cherepanov, and K. P. Tyshko. American Geophysical Union, 2013. 113

R. Ferrari, S. Griffies, A. Nurser, and G. Vallis. A boundary-value problem for the parameterized mesoscale eddy transport. *Ocean Mod.*, 32:143–156, 2010. 12, 17, 56, 57, 74, 134, 136

- F. Fetterer, K. Knowles, W. Meier, and M. Savoie. Sea Ice Index. Technical report, 2012. 96, 100
- T. Fichefet and M. A. M. Maqueda. Sensitivity of a global sea ice model to the treatment of ice thermodynamics and dynamics. *J. Geophys. Res.*, 102: 12609–12646, 1997. 85
- G. J. Fix. Finite element model for ocean circulation problems. SIAM J. APPL. MATH., 29:371–387, 1975. 78
- G. Flato and R. Brown. Variability and climate sensitivity of landfast arctic sea ice. J. Geophys. Res., 101:25767–25777, 1996. 78
- G. Flato and W. Hibler. Ridging and strength in modeling the thickness distribution of arctic sea ice. *J. Geophys. Res.*, 100:18611–18626, 1995. 129
- R. Ford, C. Pain, M. Piggott, A. Goddard, C. de Oliveira, and A. Uplemby. A nonhydrostatic finite-element model for three-dimensional stratified oceanic flows. part i: Model formulation. *Mon Weather Rev*, 132:2816–2831, 2004. 78
- O. Fringer, M. Gerritsen, and R. Street. An unstructured-grid, finite-volume, nonhydrostatic, parallel coastal ocean simulator. *Ocean Mod.*, 14:139–173, 2006. 78
- F. Gastaldi and A. Quarteroni. On the coupling of hyperbolic and parabolic systems: analytical and numerical approach. *Appl. Numer. Math.*, 6:3–31, 1990. 23
- P. Gent and J. McWilliams. Isopycnal mixing in ocean circulation models. *J. Phys. Oceanogr.*, 20:150–155, 1990. 5, 12, 16, 22, 45, 48, 52, 53, 56, 80
- P. Gent, J. Willegrand, T. McDougall, and J. McWilliams. Parameterizing eddy-induced tracer transports in coean circulation models. *J. Phys. Oceanogr.*, 25:463–474, 1995. 16, 48, 56, 133
- P. Gent, F. Bryan, G. Danabasoglu, S. Doney, W. Holland, W. Large, and J. McWilliams. The near climate system model global ocean component. *J. Clim.*, 11:1287–1306, 1998. 11
- C. Geuzaine and J.-F. Remacle. Gmsh: A 3-d finite element mesh generator with built-in pre- and post-processing facilities. *Int. J. Numer. Methods Eng.*, 79:1309–1331, 2009. 37

A. E. Gill, J. S. A. Green, and A. Simmons. Energy partition in the large-scale ocean circulation and the production of mid ocean eddies. *Deep-Sea Res.*, 21:499–528, 1974. 45, 53

- L. Girard, S. Bouillon, J. Weiss, D. Amitrano, T. Fichefet, and V. Legat. A new modeling framework for sea-ice mechanics based on elasto-brittle rheology. *Ann. Glacio.*, 52:123–132, 2011. 137
- A. Gnanadesikan, S. M. Griffies, and B. L. Samuels. Effects in a climate model of slope tapering in neutral physics schemes. *Ocean Mod.*, 16:1–16, 2007. 57
- H. Goosse. Modelling the large-scale behaviour of the coupled ocean-sea-ice system. Ph.D. thesis, Université Catholique de Louvain., 1997. 85
- G. Gorman, M. Piggott, C. Pain, R. de Oliveira, A. Umpleby, and A. Goddard. Optimisation based bathymetry approximation through constrained unstructured mesh adaptivity. *Ocean Mod.*, 12:436–452, 2006.
- S. Griffies. The Gent-McWilliams skew flux. *J. Phys. Oceanogr.*, 28:831–841., 1998. 46, 53, 136
- S. Griffies. Fundamentals of ocean climate models, chap. 13-14. Princeton University Press, USA, 2004. 16, 57, 58, 133
- S. Griffies, A. Gnanadesikan, R. Pacanowski, V. Larichev, J. Dukowicz, and R. Smith. Isoneutral diffusion in a z-coordinate ocean model. *Amer. Meteor. Soc.*, 28:805–830, 1998. 26, 55, 56
- S. Griffies, C. Böning, F. Bryan, E. Chassignet, R. Gerdes, H. Hasumi, A. Hirst, A. Treguier, and D. Webb. Developments in ocean climate modelling. *Ocean Mod.*, 2:123–192, 2000.
- R. Hallberg. Using a resolution function to regulate parameterizations of oceanic mesoscale eddy effects. *Ocean Mod.*, 72:92–103, 2013. 136
- D. Harvey. Impact of isopycnal diffusion on heat fluxes and the transient response of a two-dimensional ocean model. *J. Phys. Oceanogr.*, 25:2166–2176, 1995. 36
- C. Henning and G. Vallis. The effect of mesoscale eddies on the stratification and transport of an ocean with a circumpolar channel. J. Phys. Oceanogr., 35:880–896, 2004. 70, 74
- W. Hibler. A dynamic thermodynamic sea ice model. *J. Phys. Ocean*, 9: 815–846, 1979. 13, 78, 81, 83

A. Hirst and W. Cai. Sensitivity of a world Ocean GCM to changes in subsurface mixing parameterization. *J. Phys. Oceanogr.*, 24:1256–1279, 1994. 5

- M. E. Hohn. Geostatistics and petroleum geology. Kluwer Academics Publishers, USA, 159, 1999. 23
- M. Holland, C. Bitz, E. Hunke, W. Lipscomb, and J. Schramm. Influence of the sea ice thickness distribution on polar climate in ccsm3. *J. Clim.*, 19: 2398–2414, 2006. 7
- P. Holland, N. Bruneau, C. Enright, M. Losch, N. Kurtz, and R. Kwok. Modeled trends in antarctic sea ice thickness. *J. Clim.*, 27:3784–3801, 2014. 114, 115
- W. Holland. Experiences with various parametrizations of sub-grids scale dissipation and diffusion in numerical models of ocean circulation. In *Parameterization of small scale processes*, pages 1–9. P. Muller and D. Henderson, 1989. 3
- P. Houston, C. Schwab, and E. Suli. Discontinuous hp-finite element methods for advection-diffusion-reaction problems. *SIAM J. Numer. Anal.*, 39:2133–2163, 2002. 23
- C. Hunke, W. H. Lipscomb, A. K. Turner, N. Jeffery, and S. M. Elliott. Cice: the los alamos sea ice model, documentation and software, version 5.0.6. Technical report, Los Alamos National Laboratory, 2013. 18
- E. Hunke. Thickness sensitivities in the cice sea ice model. *Ocean Modelling*, 34:137–149, 2010. 94
- E. Hunke and J. Dukowicz. The elastic-viscous-plastic sea ice dynamics model in general orthogonal curvilinear coordinates on a sphere-incorporation of metric term. *Mon. Weather Rev.*, 130:1848–1865, 2001. 15, 81, 82, 145
- E. Hunke and M. Holland. Global atmospheric forcing data for arctic ice-ocean modeling. *J. Geophys. Research: Oceans*, 112:C04S14, 2007. 116
- E. C. Hunke and J. K. Dukowicz. An elastic-viscous-plastic model for sea ice dynamics. J. Phys. Ocean., 27:1849–1867, 1997. 13, 78, 83
- IPCC. Climate Change 2013: The Physical Science Basis. Contribution of Working Group I to the Fifth Assessment Report of the Intergovernmental Panel on Climate Change. Cambridge University Press, Cambridge, United Kingdom and New York, NY, USA, 2013. 6

C. Iselin. The influence of vertical and lateral turbulence on the characteristics of the waters at mid-depth. *Trans. Amer. Geophys. Union*, 20:414–417, 1939. 4, 22, 45, 52

- M. Jakobsson, R. Macnab, L. Mayer, R. Anderson, M. Edwards, J. Hatzky, H. Schenke, and P. Johnson. An improved bathymetric portrayal of the arctic ocean: Implications for ocean modeling and geological, geophysical and oceanographic analyses. *Geophys. Res. Let.*, 35:L07602, 2008. 92
- M. Jeffries, A. Worby, K. Morris, and W. Weeks. Seasonal variations in the properties and structural composition of sea ice and snow cover in the Bellingshausen and Amundsen Seas, Antarctica. *J. Glaciol.*, 43:138–151, 1997. 85
- J. Jungclaus, N. Keenlyside, M. Botzet, H. Haak, J. Luo, M. Latif, J. Marotzke, U. Mikolajewicz, and E. Roeckner. Ocean Circulation and Tropical Variability in the Coupled Model ECHAM5/MPI-OM. J. Clim, 19(16):3952–3972, 2006. 11
- S. Juricke, P. Lemke, R. Timmermann, and T. Rackow. Effects of stochastic ice strength perturbation on arctic finite element sea ice modeling. *J. Climate*, 26:3785–3802, 2012. 10
- E. Kalnay, M. Kanamitsu, R. Kistler, W. Collins, D. Deaven, L. Gandin, M. Iredell, S. Saha, G. White, J. Woollen, et al. The NCEP/NCAR 40-year reanalysis project. *Bull. Am. meteo. Soc.*, 77:437–471, 1996. 85
- J. Karger. Straightforward derivation of the long-time limit of the mean-square displacement in one-dimensional diffusion. Physical Review A (Atomic, Molecular, and Optical Physics), 45:4173–4174, 1992. 17, 68
- T. Kärnä, V. Legat, and E. Deleersnijder. A baroclinic discontinuous galerkin finite element model for coastal flows. $\theta cean\ Mod.,\ 2012.\ 1,\ 23,\ 53,\ 63,\ 70,\ 78$
- H. Kernkamp, A. Van Dam, G. Stelling, and E. de Goede. Efficient scheme for the shallow water equations on unstructured grids with application to the Continental Shelf. *Ocean Dyn.*, 61:1175–1188, 2011. 9
- N. Kliem. A sea ice forecasting system for the waters around greeanland. In 16th International Conference on Port and Ocean Engineering under Arctic Conditions, pages 1217–1226, 2001. 10, 78
- M. Koentopp, O. Eisen, C. Kottmeier, L. Padman, and P. Lemke. Influence of tides on sea ice in the weddell sea: Investigations with a high-resolution dynamic-thermodynamic sea ice model. *J. Geophys. Res.*, 110, 2005. 117

N. T. Kurtz, S. L. Farrell, M. Studinger, N. Galin, J. P. Harbeck, R. Lindsay, V. D. Onana, B. Panzer, and J. G. Sonntag. Sea ice thickness, freeboard, and snow depth products from operation icebridge airborne data. *The Cryos.*, 7: 1035–1056, 2013. 111

- R. Kwok. Baffin bay ice drift and export: 2002–2007. Geophys. res. let., 34, 2007. 124
- R. Kwok and G. Cunningham. Seasonal ice area and volume production of the arctic ocean: November 1996 through april 1997. J. Geophys. Res., 107, 2002. 84
- R. Kwok and G. F. Cunningham. Icesat over arctic sea ice: Estimation of snow depth and ice thickness. *J. Geophys. Res.*, 113, 2008. 100
- R. Kwok, G. Cunningham, and S. Pang. Fram strait sea ice outflow. *J. Geophys. Res.*, 109, 2004. 125
- R. Kwok, G. F. Cunningham, M. Wensnahan, I. Rigor, H. J. Zwally, and D. Yi. Thinning and volume loss of the Arctic Ocean sea ice cover: 2003-2008. *J. Geophys. Res.*, 114, 2009. 109
- Z. Lai, C. Chen, G. Cowles, and R. Beardsley. A nonhydrostatic version of fvcom: 1. validation experiments. *J. Geophys. Res.*, 115, 2010. 9
- J. Lambrechts, R. Comblen, V. Legat, C. Geuzaine, and J.-F. Remacle. Multiscale mesh generation on the sphere. *Ocean Dyn.*, 58:461–473, 2008. 37
- W. Large and S. Yeager. Diurnal to decadal global forcing for ocean and sea ice models: The datasets and climatologies. Technical Report TN-460+STR, NCAR, 2004. 85
- W. Large and S. Yeager. The global climatology of an interannual varying air-sea flux data set. *Clim. Dyn.*, 33:341–364, 2008. 90, 91, 94
- O. Lecomte, T. Fichefet, M. Vancoppenolle, F. Domine, F. Massonnet, P. Mathiot, S. Morin, and P. Barriat. On the formulation of snow thermal conductivity in large-scale sea ice models. *J. Adv. Mod. Earth Sys.*, 5:542–557, 2013. 116, 137
- S. Legrand, V. Legat, and E. Deleersnijder. Delaunay mesh generation for an unstructured-grid ocean circulation model. *Ocean Mod.*, 2:17–28, 2000. 9
- P. Lemke. A coupled one-dimensional sea ice-ocean model. *J. Geophys. Res.*, 92:13164–13172, 1987. 81
- P. Lesaint and P.-A. Raviart. On a finite element method for solving the neutron transport equation. Academic Press, USA, 1974. 23

O. Lietaer, T. Fichefet, and V. Legat. Coupled model of ocean general circulation and sea ice evolution in the arctic ocean. *Ocean Mod.*, 24:140–152, 2008. 10, 78, 118

- R. Lindsay, M. Wensnahan, A. Schweiger, and J. Zhang. Evaluation of seven different atmospheric reanalysis products in the arctic. J. Clim., 27:2588– 2606, 2014. 137
- W. Lipscomb. Remapping the thickness distribution in sea ice models. *J. Geophys. Res.*, 106:13989–14000, 2001. 83, 85
- R. Lohner, K. Morgan, J. Peraire, and M. Vahdati. Finite element flux-corrected transport (FEM-FCT) for the euler and Navier-Stokes equations. *IJNMF*, 7:1093–1109, 1987. 80
- C. Lüpkes, V. Gryanik, J. Hartmann, and E. Andreas. A parametrization, based on sea ice morphology, of the neutral atmospheric drag coefficients for weather prediction and climate models. J. Geophys. Res., 117, 2012. 78
- G. Madec and t. N. team. NEMO ocean engine. Technical Report 27, Institut Pierre-Simon Laplace (IPSL), France, 2008. 1, 46, 72
- J. Marotzke. Influence of convective adjustment on the stability of the thermohaline circulation. J. Phys. Oceanogr., 21:903–907, 1991. 46, 71
- J. Marshall, H. Jones, R. Karsten, and R. Wardle. Can eddies set ocean stratification? J. Phys. Oceanogr., 32:26–38, 2002. 70
- S. Marsland, H. Haak, J. Jungclaus, M. Latif, and F. Röske. The max-planck-institute global ocean/sea ice model with orthogonal curvilinear coordinates. Ocean Mod., 5:91–127, 2003. 11
- F. Massonnet, T. Fichefet, H. Goosse, M. Vancoppenolle, P. Mathiot, and K. B.C. On the influence of model physics on simulations of arctic and antarctic sea ice. *The Cryo.*, 5:687–699, 2011. 101, 106, 112, 116, 135
- F. Massonnet, P. Mathiot, T. Fichefet, H. Goosse, C. Beatty, M. Vancoppenolle, and T. Lavergne. A model reconstruction of the antarctic sea ice thickness and volume changes over 1980-2008 using data assimilation. *Ocean Mod.*, 64: 67–75, 2013. 96, 101, 102, 107, 108
- Y. Masumoto, H. Sasaki, T. Kagimoto, N. Komori, A. Ishida, Y. Sasai, T. Miyama, T. Motoi, H. Mitsudera, K. Takahashi, et al. A fifty-year eddy-resolving simulation of the world ocean: Preliminary outcomes of ofes (ogcm for the earth simulator). *J. Earth Simulator*, 1:35–56, 2004. 10
- P. Mathieu and E. Deleersnijder. What is wrong with isopycnal diffusion in world ocean models? *Appl. Math. Modell.*, 22:367–378, 1998. 36

G. Maykut and N. Understeiner. Some results from a time-dependent thermodynamic model of sea ice. J. Geophys. Res., 76:1550–1575, 1971. 13, 77, 84

- T. McDougall. Neutral surfaces. J. Phys. Oceanogr., 17:1950–1967, 1987. 5, 45, 53
- T. McDougall and J. Church. Pitfalls with the Numerical Representation of Isopycnal Diapycnal Mixing. J. Phys. Oceanogr., 16:196–199, 1986. 4
- T. McDougall, D. Jackett, D. Wright, and R. Feistel. Algorithms for density, potential temperature, conservative temperature, and the freezing temperature of seawater. *J. Atmos. Oceanic Technol.*, 23:1709–1728, 2006. 46, 66, 71
- V. Meløysund, B. Leira, K. Høiseth, and K. Lisø. Predicting snow density using meteorological data. *Meteo. Appl.*, 14:413–423, 2007. 130
- P. A. Miller, S. W. Laxon, and D. L. Feltham. Consistent and contrasting decadal Arctic sea ice thickness predictions from a highly optimized sea ice model. J. Geophys. Res., 112, 2007. 94
- R. Montgomery. The present evidence on the importance of lateral mixing processes in the ocean. Amer. Meteor. Soc., 21:87–94, 1940. 4, 22, 45, 52
- M. Montoya, A. Griesel, A. Levermann, M. Mignot, J.and Hofmann, A. Ganopolski, and S. Rahmstorf. The earth system model of intermediate complexity climber-3α. part i: description and performance for present-day conditions. Clim. Dyn., 26:237–263, 2005. 78
- B. Mukherji. Crack propagation in sea ice: a finite element approach. *AIDJEX Bull.*, 18:69–75, 1973. 10, 78
- D. Notz. Challenges in simulating sea ice in earth system models. WIREs Clim. Change, 3:506–526, 2012. 15
- J. Oden and S. Kim. Interior penalty methods for finite element approximations of the Signorini problem in elastostatics. Comp. Math. Appl., 8:35–56, 1982.
- R. Pacanowski and S. Philander. Parameterization of vertical mixing in numerical models of tropical oceans. *J. Geophys. Res.*, 11:1443–1451, 1981. 71, 80
- C. Parkinson and W. Washington. A large-scale numerical model of sea ice. *J. Geophys. Res.*, 84:311–337, 1979. 81

K. Partington, T. Flynn, D. Lamb, C. Bertoia, and K. Dedrick. Late twentieth century northern hemisphere sea-ice record from us national ice center ice charts. *J. Geophys. Res.*, 108, 2003. 135

- A. Pestiaux, S. Melchior, J. Remacle, T. Kärnä, T. Fichefet, and J. Lambrechts. Discontinuous galerkin finite element discretization of a strongly anisotropic diffusion operator. *Int. J. Num. Fluids*, 75:365–383, 2014. 54, 62
- I. Peterson, J. Hamilton, S. Prinsenberg, and R. Pettipas. Wind-forcing of volume transport through lancaster sound. *J. Geophys. Res.*, 117, 2012. 10
- A. Petty, P. Holland, and D. Feltham. Sea ice and the ocean mixed layer over the antarctic shelf seas. *The Cryos.*, 8:761–783, 2014. 114, 115
- D. D. Pietro, A. Ern, and J.-L. Guermond. Discontinuous Galerkin methods for anisotropic semidefinite diffusion with advection. *SIAM J. Numer. Anal.*, 46:805–831, 2008. 23
- M. Piggott, G. Gorman, and C. Pain. Multi-scale ocean modelling with adaptive unstructured grids. *CLIVAR Exc. Ocean Model Dev. Assess.*, 12:21–23, 2007. 9
- M. J. Prather. Numerical advection by conservation of second-order moments. J. Geophys. Res. Atm., 91:6671–6681, 1986. 83
- D. Pringle, H. Eicken, H. Trodahl, and L. Backstrom. Thermal conductivity of landfast Antarctic and Arctic sea ice. *J. Geophys. Res.*, 112, 2007. 5
- R. W. S. B. R. C. T. F. J. F. V. K. A. P. J. S. J. S. R. S. f. A. S. Randall, D.A. and K. Taylor. Cambridge University Press, 2007. 78
- M. Redi. Oceanic isopycnal mixing by coordinate rotation. *J. Phys. Ocean.*, 12:1154–1158, 1982. 4, 16, 22, 26, 45, 52, 57, 80, 133
- W. Reed and T. Hill. Triangular mesh methods for the neutron transport equation. Technical report, 1973. 23
- P. Rhines. Mesoscale Eddies, Encyclopedia of ocean sciences. Elsevier, USA, 2009. 3, 45, 52
- B. Rivière. Discontinuous Galerkin methods for solving elliptic and parabolic equations: theory and implementation. Frontiers in applied mathematics, SIAM, Texas, 2008. 17, 24, 27, 29, 62
- A. T. Roach, K. Aagaard, C. H. Pease, S. A. Salo, T. Weingartner, V. Pavlov, and M. Kulakov. Direct measurements of transport and water properties through the bering strait. *J. Geophys. Res.*, 100:18443–18457, 1995. 123

D. Rothrock, R. Kwok, and D. Groves. Satellite views of the arctic ocean freshwater balance. In *The Freshwater Budget of the Arctic Ocean*, pages 409–451. Springer, 2000. 125

- C. Rousset, M. Vancoppenolle, G. Madec, T. Fichefet, S. Flavoni, A. Barthélemy, R. Benshila, J. Chanut, C. Levy, S. Masson, and F. Vivier. The Louvain-la-Neuve sea ice model LIM3.5: global and regional capabilities. Geosc. Mod. Dev. Disc., 8:3403-3441, 2015. 129, 137
- D. Salas-Mélia, F. Chauvin, M. Déqué, H. Douville, J. Gueremy, P. Marquet, S. Planton, J. Royer, and S. Tyteca. Description and validation of the cnrmcm3 global coupled model. *Clim. Dyn.*, 103:1–36, 2005. 18
- U. Schauer, A. Beszczynska-Möller, W. Walczowski, E. Fahrbach, J. Piechura, and E. Hansen. Variation of measured heat flow through the fram strait between 1997 and 2006. In Arctic-Subarctic Ocean Fluxes, pages 65–85. Springer, 2008. 123
- C. Schmitt, C. Kottmeier, S. Wassermann, and M. Drinkwater. 2004. 113
- J. L. Schramm, M. M. Holland, J. A. Curry, and E. E. Ebert. Modeling the thermodynamics of a sea ice thickness distribution: 1. sensitivity to ice thickness resolution. J. Geophys. Res., 102:23079–23091, 1997. 7
- R. Schulkes, L. Morland, and R. Staroszczyk. A finite-element treatment of sea ice dynamics for different ice rheologies. *Int. J. Num. Ana. Methods Geomech.*, 22:153–174, 1998. 10, 78
- A. Schweiger, R. Lindsay, J. Zhang, M. Steele, H. Stern, and R. Kwok. Uncertainty in modeled arctic sea ice volume. J. Geophys. Res., 116:C00D06, 2011. 96, 101
- A. Semtner. A model for the thermodynamic growth of sea ice in numerical investigations of climate. J. Phys. Oceanogr., 6:379–389, 1976. 13, 78, 81
- M. Serreze, A. Barrett, A. Slater, R. Woodgate, K. Aagaard, R. Lammers, M. Steele, R. Moritz, M. Meredith, and C. Lee. The large-scale freshwater cycle of the arctic. J. Geophys. Res., 2006. 124
- S. Shah, A. Heemik, and E. Deleersnider. Assessing lagrangian schemes for simulating diffusion on non-flat isopycnal surfaces. *Ocean. Mod.*, 39:351– 361, 2011. 67
- K. Shahbazi. An explicit expression for the penalty parameter of the interior penalty method. J. Computational Physics, 205:401–407, 2004. 28, 62

A. F. Shchepetkin and J. McWilliams. The regional oceanic modeling system (roms): a split-explicit, free-surface, topography-following-coordinate oceanic model. *Ocean Mod.*, 9:347–404, 2005. 72

- K. Shine. Parametrization of the shortwave flux over high albedo surfaces as a function of cloud thickness and surface albedo. Quart. J. R. Meteo. Soc., 110:747–764, 1984. 85
- K. P. Shine and A. Henderson-Sellers. The sensitivity of a thermodynamic sea ice model to changes in surface albedo parameterization. J. Geophys. Res. Atm., 90:2243–2250, 1985. 91, 94, 95, 96, 135
- R. Shuchman, E. Josberger, C. Russel, K. Fischer, O. Johannessen, J. Johannessen, and P. Gloersen. Greenland sea odden sea ice feature: Intra-annual and interannual variability. J. Geophys. Res., 103:12709–12724, 1998. 116
- D. Sidorenko, Q. Wang, and J. Schröter. Fesom under coordinate ocean-ice reference experiment forcing. *Ocean Dyn.*, 61:881–890, 2011. 10, 79
- L. Smedsrud, R. Ingvaldsen, J. Nilsen, and O. Skagseth. Heat in the barents sea: Transport, storage, and surface fluxes. *Ocean Sc.*, pages 219–234, 2010. 123
- D. Sodhi and W. Hibler. Nonsteady ice drift in the strait of belle isle. In Sea ice processes and models, pages 177–186. University of Washington press, 1980. 10
- T. Sou and G. Flato. Sea ice in the canadian arctic archipelago: Modeling the past (1950-2004) and the future (2041-60). J. Clim., 22:2181–2198, 2009. 118
- D. Spivakovskaya, A. Heemink, and E. Deleersnijder. Lagrangian modelling of multi-dimensional advection-diffusion with space-varying diffusivities: theory and idealized test cases. *Ocean dyn.*, 57:189–203, 2007. 34
- M. Steele. Sea ice melting and floe geometry in a simple ice-ocean model. J. $Geophys.\ Res.,\ 97:17729–17738,\ 1992.\ 84$
- M. Steele, R. Morley, and W. Ermold. PHC: A global ocean hydrography with a high quality Arctic Ocean. *J. Climate*, 14:2079–2087, 2001a. 46
- M. Steele, R. Morley, and W. Ermold. Phc: a global ocean hydrography with a high-quality arctic ocean. *J. Climate*, 14:2079–2087, 2001b. 93
- H. L. Stern, D. A. Rothrock, and R. Kwok. Open water production in arctic sea ice: Satellite measurements and model parameterizations. *J. Geophys. Res.*, pages 20601–20612, 1995. 95

J. C. Stroeve, M. C. Serreze, M. M. Holland, J. E. Kay, J. Malanik, and A. P. Barret. The arctic's rapidly shrinking sea ice cover: a research synthesis. Climatic change, 110:1005–1027, 2012. 6, 106

- D. Sulsky, H. Schreyer, and K. Peterson. Using the material-point method to model sea ice dynamics. *J. Geophys. Res.*, 112, 2007. 78
- B. Tartinville, J. Campin, T. Fichefet, and H. Goosse. Realistic representation of the surface freshwater flux in an ice-ocean general circulation model. *Ocean Mod.*, 3:95–108, 2001. 86
- D. Thomas and G. Dieckmann. Sea Ice, An introduction to its physics, chemistry, biology and geology. Blackwell Science, 2003. 6
- J. F. S. Thomson. Short-term ice motion modeling with application to the beaufort sea. J. Geophys. Res., 93:6819–6836, 1988. 10, 78
- A. Thorndike, D. Rothrock, G. Maykut, and R. Colony. The thickness distribution of sea ice. *J. Geophys. Res.*, 80:4501–4513, 1975. 13, 84, 129
- G. Timco and R. Frederking. A review of sea ice density. Cold Regions Science and Technology, 24:1–6, 1996. 130
- R. Timmermann, A. Beckmann, and H. Hellmer. Simulations of ice-ocean dynamics in the weddell sea. 1. model configuration and validation. J. Geophys. Res., 107:C33024, 2002. 81
- R. Timmermann, H. Goosse, G. Madec, T. Fichefet, C. Ethe, and V. Duliere. On the representation of high latitude processes in the orca-lim global coupled sea ice-ocean model. *Ocean Model.*, 8:175–201, 2005. 95
- R. Timmermann, S. Danilov, J. Schröter, C. Böning, D. Sidorenko, and K. Rollenhagen. Ocean circulation and sea ice distribution in a finite element global sea ice-ocean model. *Ocean Mod.*, 27:114–129, 2009. 2, 79
- A. Tivy, S. Howell, B. Alt, S. McCourt, R. Chagnon, G. Crocker, T. Carrieres, and J. Yackel. Trends and variability in summer sea ice cover in the canadian arctic based on the canadian ice service digital archive, 1960-2008 and 1968-2008. *J. Geophys. Res.*, 116, 2011. 118
- K. Trenberth, J. Olson, and W. Large. A global ocean wind stress climatology based on the ECMWF analyses. Technical Report NCAR/TN-338+STR, National Center for Atmspheric Research, Boulder, Colorado, 1989. 85
- J. Tuhkuri and M. Lensu. Laboratory tests on ridging and rafting of ice sheets.
 J. Geophys. Res., 107, 2002. 84

K. Vallis. Large-scale circulation and production of stratification: Effects of wind, geometry, and diffusion. J. Phys. Oceanogr., 30:933–954, 2000. 73

- A. T. van Scheltinga, P. G. Myers, and J. D. Pietrzak. A finite element sea ice model of the canadian arctic archipelago. *Ocean. Dyn.*, 60:1539–1558, 2010. 10, 78
- M. Vancoppenolle, T. Fichefet, and C. Bitz. On the sensitivity of undeformed arctic sea ice to its vertical salinity profile. *Geophys. Res. Let.*, 32:L16502, 2005. 15
- M. Vancoppenolle, T. Fichefet, and H. Goosse. Simulating the mass balance and salinity of arctic and antarctic sea ice. 2. importance of sea ice salinity variations. *Ocean Mod.*, 27:54–69, 2009a. 85
- M. Vancoppenolle, T. Fichefet, H. Goosse, S. Bouillon, G. Madec, and M. Maqueda. Simulating the mass balance and salinity of arctic and antarctic sea ice. 1. model description and validation. *Ocean Mod.*, 27:33–53, 2009b. 1, 15, 18, 78, 116, 135
- M. Vancoppenolle, C. M. Bitz, and T. Fichefet. Summer landfast sea ice desalination at Point Barrow, Alaska: Modeling and observations. *Journal of Geophysical Research: Oceans* (1978–2012), 112, 2007. 85
- T. Vihma, R. Pirazzini, I. Fer, I. Renfrew, J. Sedlar, M. Tjernstrom, C. Lupkes, T. Nygard, D. Notz, J. Weiss, D. Marsan, B. Cheng, G. Birnbaum, S. Gerland, D. Chechin, and J. Garscard. Advances in understanding and parameterization of small-sacle physical processes in the marine arctic climate system: a review. Atmos. Chem. Phys., 14:9403–9450, 2014.
- L. R. Wang and M. Ikeda. A lagrangian description of sea ice dynamics using the finite element element method. *Ocean Mod.*, 7:21–38, 2004. 10, 78
- Q. Wang, S. Danilov, and J. Schröter. Finite element ocean circulation model based on triangular prismatic elements, with application in studying the effect of topography representation. J. Geophys. Res., 113:C05015, 2008. 2, 27, 54, 59, 79
- Q. Wang, S. Danilov, D. Sidorenko, R. Timmermann, C. Wekerle, X. Wang, T. Jung, and J. Schröter. The Finite Element Sea Ice-Ocean Model (FESOM) v.1.4: formulation of an ocean general circulation model. *Geosci. Mod. Dev.*, 7(2):663–693, 2014. 80
- Q. Wang, M. Ilicak, R. Gerdes, H. Drange, et al. An assessment of the arctic ocean in a suite of interannual core-ii simulations: Sea ice and freshwater. *Ocean Mod. (submitted)*, 2015. 130, 136

X. Wang, Q. Wang, D. Sidorenko, S. Danilov, J. Schröter, and T. Jung. Long term ocean simulations in fesom: Validation and applications in studying the impact of greenland icesheet melting. *Ocean Dyn.*, 2012. 10

- T. Warburton and J. Hesthaven. On the constants in hp-finite element trace inverse inequalities. *Comput. Methods Appl. Mech. Engrg.*, 192:2765–2773, 2003. 30
- C. Wekerle, Q. Wang, S. Danilov, T. Jung, and J. Schröter. The canadian arctic archipelago throughflow in a multiresolution global model: Model assessment and the driving mechanism of interannual variability. J. Geophys. Res., 118: 4525–4541, 2013. 10, 78, 79, 137
- L. White, E. Deleersnijder, and V. Legat. A three-dimensional unstructured mesh finite element shallow-water model, with application to the flows around an island and in a wind-driven, elongated basin. *Ocean Mod.*, 22: 26–47, 2008a. 1, 23, 53
- L. White, E. Deleersnijder, and V. Legat. A three-dimensional unstructured mesh finite element shallow-water model, with application to the flows around an island and in a wind-driven, elongated basin. *Ocean Mod.*, 22: 26–47, 2008b. 9, 61, 141
- M. Windmuller. Untersuchung von atmospharischen reanalysedaten im Weddellmeer und anwendung auf ein dynamisch thermodynamisches meereismodell. PhD thesis, Christian-Albrechts-Univ. zu Kiel, 1997. 116
- M. Winton, W. Anderson, T. Delworth, S. Griffies, W. Hurlin, and A. Rosati. Has coarse ocean resolution biased simulations of transient climate sensitivity? Geophys. Res. Let., 41:8522–8529, 2014. 137
- R. Woodgate and K. Aagaard. Revising the bering strait freshwater flux into the arctic ocean. *Geophys. Res. Let.*, 32, 2005. 124, 125
- A. Worby, C. Geiger, M. Paget, M. Van Woert, S. Ackley, and T. DeLiberty. Thickness distribution of antarctic sea ice. J. Geophys. Res., 113, 2008. 110, 125
- N. Yakovlev. Coupled model of ocean general circulation and sea ice evolution in the arctic ocean. *Izvestiya. Atmos. Ocean. Phys.*, 39:355–368, 2003. 10, 78
- J. Zhang and D. Rothrock. Modeling arctic sea ice with an efficient plastic solution. *J. geophys. res.*, 105:3325–3338, 2000. 78